MAX-PLANCK-INSTITUT
FÜR METEOROLOGIE

International Max Planck Research School on Earth System Modelling

The impact of ocean eddies on tropical cyclone intensity on a global scale and the role of boundary layer dynamics

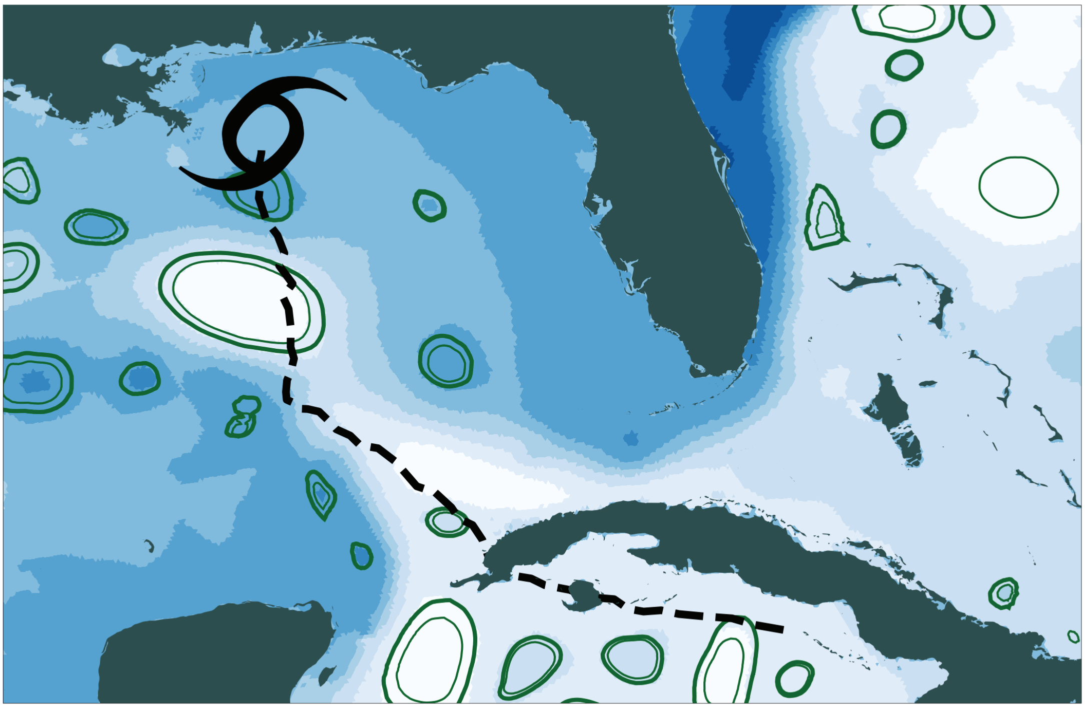

Arjun Unnithan Kumar

Hamburg 2022

Berichte zur Erdsystemforschung
Reports on Earth System Science

258
2022

Hinweis

Die Berichte zur Erdsystemforschung werden vom Max-Planck-Institut für Meteorologie in Hamburg in unregelmäßiger Abfolge herausgegeben.

Sie enthalten wissenschaftliche und technische Beiträge, inklusive Dissertationen.

Die Beiträge geben nicht notwendigerweise die Auffassung des Instituts wieder.

Die "Berichte zur Erdsystemforschung" führen die vorherigen Reihen "Reports" und "Examensarbeiten" weiter.

Notice

The Reports on Earth System Science are published by the Max Planck Institute for Meteorology in Hamburg. They appear in irregular intervals.

They contain scientific and technical contributions, including PhD theses.

The Reports do not necessarily reflect the opinion of the Institute.

The "Reports on Earth System Science" continue the former "Reports" and "Examensarbeiten" of the Max Planck Institute.

Anschrift / Address

Max-Planck-Institut für Meteorologie
Bundesstrasse 53
20146 Hamburg
Deutschland

Tel./Phone: +49 (0)40 4 11 73 - 0
Fax: +49 (0)40 4 11 73 - 298

name.surname@mpimet.mpg.de
www.mpimet.mpg.de

Layout

Bettina Diallo and Norbert P. Noreiks
Communication

Copyright

Photos below: ©MPI-M
Photos on the back from left to right:
Christian Klepp, Jochem Marotzke,
Christian Klepp, Clotilde Dubois,
Christian Klepp, Katsumasa Tanaka

The impact of ocean eddies on tropical cyclone intensity on a global scale and the role of boundary layer dynamics

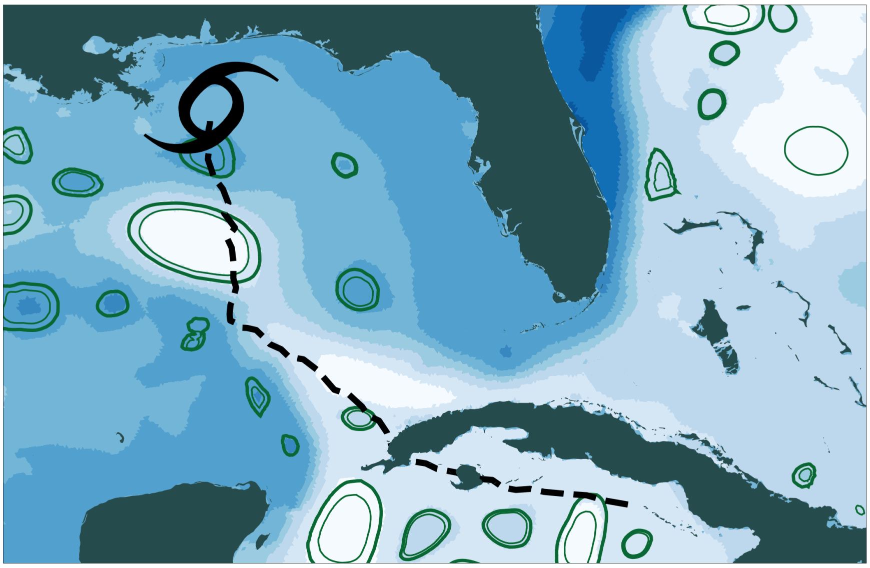

Arjun Unnithan Kumar

Hamburg 2022

Arjun Unnithan Kumar
aus Brighton, Großbritannien

Max-Planck-Institut für Meteorologie
The International Max Planck Research School on Earth System Modelling
(IMPRS-ESM)
Bundesstrasse 53
20146 Hamburg

Tag der Disputation: 8. Juni 2022

Folgende Gutachter empfehlen die Annahme der Dissertation:
Prof. Dr. Jochem Marotzke
Dr. Nils Brüggemann

Vorsitzender des Promotionsausschusses:
Prof. Dr. Hermann Held

Dekan der MIN-Fakultät:
Prof. Dr.-Ing. Norbert Ritter

Titelgrafik: Arjun Kumar

Berichte zur Erdsystemforschung / Max-Planck-Institut für Meteorologie 258
Reports on Earth System Science / Max Planck Institute for Meteorology 2022

ISSN 1614-1199 - doi: 10.17617/2.3432708

Arjun Unnithan Kumar

The impact of ocean eddies on tropical cyclone intensity on a global scale and the role of boundary layer dynamics

ABSTRACT

Warm-core ocean eddies have been linked to the rapid intensification of tropical cyclones across the world's oceans, from Hurricane Katrina in the Atlantic, to Supertyphoon Maemi in the Pacific and Cyclone Nargis in the Indian Ocean. Normally, sea-surface cooling induced by tropical cyclones acts as a brake on tropical cyclone intensity. By suppressing sea-surface cooling, warm-core eddies enable tropical cyclones to intensify further. Although coupled atmosphere-ocean forecasting models simulate sea-surface cooling, rapid intensification remains difficult to predict. A better understanding of the effect of warm-core eddies on tropical cyclone intensity is key to improving forecasts.

In my thesis, I focus on the dynamics of the tropical cyclone boundary layer. Boundary layer dynamics influence the structure of the tropical cyclone circulation, which is inextricably linked to tropical cyclone intensity. While boundary layer dynamics are important for tropical cyclone intensity in atmosphere-only models, they have not been explored in coupled models. I address this gap by analysing a simulation of a tropical cyclone that decays due to sea-surface cooling and subsequently reintensifies when the sea-surface cooling is suppressed by a warm-core eddy. I find boundary layer dynamics play an important role modulating the decay and reintensification through changes in the structure of the tropical cyclone. Moreover, I find the differing rates of decay cannot be explained without boundary layer dynamics. These results underscore the importance of accurately representing boundary layer dynamics in coupled forecasting models and guide the choice of boundary layer parameterisations, which affect the ability of forecasting models to predict rapid intensification.

In addition, I investigate the impact of warm-core and cold-core eddies on tropical cyclone intensity on a global scale with the first analysis of a global coupled simulation that resolves tropical cyclones and ocean eddies. I find encounters between tropical cyclones and ocean eddies are common. My analysis reveals that tropical cyclones that encounter warm-core eddies reach on average a higher peak intensity, whereas cold-core eddies do not have an effect on the average peak intensity. If these results prove to be robust, they point to a potential bias in future projections of tropical cyclone intensity, which are based on climate simulations that do not resolve ocean eddies. Disentangling the impact of ocean eddies in future eddy-resolving climate simulations will hinge on the sensitivity of tropical cyclone intensity to boundary layer schemes and our understanding of boundary layer dynamics.

ZUSAMMENFASSUNG

Über alle Ozeane hinweg wurden warme Ozeanwirbel mit der rasanten Intensivierung tropischer Wirbelstürme in Verbindung gebracht, von Hurrikan Katrina im Atlantik, über den Supertaifun Maemi im Pazifik, bis hin zum Zyklon Nargis im Indischen Ozean. Normalerweise bremst die von tropischen Wirbelstürmen herbeigeführte Abkühlung der Meeresoberflächentemperatur eine weitere Intensivierung der Stürme aus. Indem warme Ozeanwirbel diese Abkühlung unterdrücken, ermöglichen sie eine fortschreitende Intensivierung tropischer Wirbelstürme. Obwohl numerische Vorhersagemodelle mit gekoppelten Komponenten für die Atmosphäre und den Ozean in der Lage sind die Abkühlung der Meeresoberflächentemperatur zu simulieren, bleibt eine rasante Intensivierung tropischer Wirbelstürme schwer vorherzusagen. Ein besseres Verständnis des Effekts von warmen Ozeanwirbeln auf die Intensität von tropischen Wirbelstürmen ist ein wichtiger Schlüssel zur Verbesserung von Vorhersagen.

In meiner Arbeit fokussiere ich mich auf die Dynamiken in der Oberflächengrenzschicht tropischer Wirbelstürme. Diese Dynamiken beeinflussen die Struktur eines tropischen Wirbelsturms, welche untrennbar mit dessen Intensität verbunden ist. Während die Wichtigkeit von Grenzschichtdynamiken für die Intensität von tropischen Wirbelstürmen in Atmosphärenmodellen bereits gezeigt wurde, ist der Effekt in gekoppelten Modellen noch unerforscht. Ich adressiere diese Wissenslücke, indem ich einen simulierten tropischen Wirbelsturm untersuche, dessen Intensität sich in seinem Verlauf zunächst aufgrund der von ihm induzierten Abkühlung der Meeresoberflächentemperatur verringert. Im Anschluss nimmt die Intensität des tropischen Wirbelsturms wieder zu, da der tropische Wirbelsturm auf einen warmen Ozeanwirbel trifft, welcher die Abkühlung der Meeresoberflächentemperatur unterdrückt. Meine Ergebnisse zeigen, dass die Dynamiken in der Oberflächengrenzschicht eine wichtige Rolle für die Abschwächung und die anschließende Intensivierung des tropischen Wirbelsturms spielen, da sie einen Einfluss auf dessen Struktur ausüben. Des Weiteren zeige ich, dass die unterschiedlichen Abschwächungsraten nicht ohne Berücksichtigung der Grenzschichtdynamik erklärt werden können. Diese Ergebnisse unterstreichen die Wichtigkeit einer korrekten Darstellung der Grenzschichtdynamik in gekoppelten Vorhersagemodellen und geben eine Hilfestellung bei der Auswahl von Parametrisierungen der Grenzschicht, welche die Qualität der Vorhersage einer rasanten Intensivierung tropischer Zyklone beeinflussen.

Darüber hinaus studiere ich den globalen Einfluss von warmen und kalten Ozeanwirbeln auf die Intensität von tropischen Wirbelstürmen mit Hilfe der ersten Analyse einer globalen, gekoppelten Simulation, die tropische Wirbelstürme und Ozeanwirbel auflösen kann. Ich zeige, dass Begegnungen zwischen tropischen Wirbelstürmen und Ozeanwirbeln häufig vorkommen. Meine Analyse offenbart, dass tropische Wirbelstürme, die einem warmen Ozeanwirbel begegnen, im Durchschnitt eine höhere Maximalintensität erreichen, wohingegen kalte Ozeanwirbel keinen Einfluss auf die erreichte Maximalintensität besitzen. Wenn sich diese Ergebnisse als robust herausstellen, deutet dies auf eine mögliche Verzerrung in Projektionen für die zukünftige Intensität von tropischen Wirbelstürmen

hin, da diese auf Klimamodellen basieren, die Ozeanwirbel nicht auflösen können. Unser Verständnis des Einflusses von Ozeanwirbeln in zukünftigen, hochauflösenden Klimasimulationen hängt ab von der Sensitivität, die tropische Wirbelstürme gegenüber Grenzschichtparametrisierungen zeigen, sowie von unserem Wissen über die Dynamiken innerhalb der Oberflächengrenzschicht.

PUBLICATIONS RELATED TO THIS DISSERTATION

Appendix A:

A. U. Kumar, N. Brüggemann, R. K. Smith, and J. Marotzke (2021). “Response of a tropical cyclone to a subsurface ocean eddy and the role of boundary layer dynamics.” In: *Quarterly Journal of the Royal Meteorological Society* n/a.n/a. DOI: `https://doi.org/10.1002/qj.4210`. eprint: `https://rmets.onlinelibrary.wiley.com/doi/pdf/10.1002/qj.4210`. URL: `https://rmets.onlinelibrary.wiley.com/doi/abs/10.1002/qj.4210`

Appendix B:

A. U. Kumar, N. Brüggemann, and J. Marotzke (2022). *The impact of ocean eddies on tropical cyclone intensity in a one-year, global coupled atmosphere-ocean simulation (in preparation)*

ACKNOWLEDGMENTS

With the rest of the thesis written up, after what appears to have been an eternity, I finally have time to realise how far I have come over the past four years. Moving to a new country, learning a new language and doing a PhD all at the same time was never going to be easy. And while I think I managed rather well, I make no mistake about the fact that getting to where I am now would not have been possible without the help and support of many people.

I would like to start by thanking my supervisor, Jochem Marotzke, for giving me the opportunity to come and work at the Max Planck Institute for Meteorology and for his support and guidance throughout the PhD. In addition, I would like to express my gratitude to my co-supervisor, Nils Brüggemann, for his help and invaluable feedback week in week out. I would also like to extend my gratitude to Roger Smith for sharing his knowledge of tropical cyclones with me and for two enjoyable research stays in Munich. Furthermore, I would like to thank the IMPRS Office for helping me with the move to Germany and their administrative support.

My time at the Institute has been a pleasure thanks to all my fellow PhD students. Lennart deserves a special mention for putting up with my questionable sense of humour back at the flat and for providing me with feedback for this lengthy manuscript not once, but twice. Writing the manuscript in the last few weeks was especially stressful and I would not have managed without the kindness and affection shown by Alvine. Finally, these acknowledgements would not be complete without thanking Mum, Dad and Siddharth, whose unconditional support and encouragement allowed me to get here in the first place.

CONTENTS

I UNIFYING ESSAY 1

1 INTRODUCTION 3
  1.1 Tropical cyclones and society 3
  1.2 Operational track and intensity forecasting 5
  1.3 The negative feedback and coupled models 7
  1.4 Subsurface ocean structure and warm-core eddies 9
  1.5 Numerical models for studying the impact of warm-core eddies 10
  1.6 Research objectives 10
    1.6.1 Overarching goal 10
    1.6.2 Research question 1 10
    1.6.3 Research question 2 11

2 THE ROLE OF BOUNDARY LAYER DYNAMICS 13
  2.1 Tropical cyclone circulation 13
  2.2 Spin down in coupled models 16
  2.3 Boundary layer dynamics 16
    2.3.1 Vertical mass flux 16
    2.3.2 Radius of forced ascent 18
    2.3.3 Rotating-convection paradigm 18
    2.3.4 Non-linear boundary layer dynamics and the slab boundary layer model 19
  2.4 Research question 21
  2.5 Strategy to answer the research question 21
  2.6 Simulation 22
  2.7 Change in tropical cyclone intensity 22
  2.8 Role of air-sea coupling 22
  2.9 Change in primary and secondary circulation 24
  2.10 Conceptual framework 25
  2.11 Process-based analysis 27
    2.11.1 Slow decay 28
    2.11.2 Fast decay 28
    2.11.3 Re-intensification 30
    2.11.4 Discussion 30
  2.12 Complementary solutions from the steady-state slab boundary layer model 30
    2.12.1 Obtaining the solutions 31
    2.12.2 Comparison with the ICON simulation 31
    2.12.3 Discussion 31
  2.13 Summary and conclusions 32

3 THE IMPACT OF OCEAN EDDIES ON TROPICAL CYCLONE INTENSITY ON A GLOBAL SCALE 35
  3.1 Tropical cyclone intensity and climate change 35

- 3.2 Limitations of climate simulations 35
- 3.3 Global aspects of interactions between ocean eddies and tropical cyclones 36
- 3.4 Research question 37
- 3.5 Strategy to answer the research question 38
- 3.6 Simulation 38
- 3.7 Tropical cyclone climatology 39
  - 3.7.1 Tracks 39
  - 3.7.2 Intensity and frequency 39
  - 3.7.3 Pressure-wind relationship 40
  - 3.7.4 Sea-surface cooling 41
  - 3.7.5 Evaluation of tropical cyclone climatology 42
- 3.8 Impact of ocean eddies on tropical cyclone intensity 42
  - 3.8.1 Frequency of encounters 42
  - 3.8.2 Tropical cyclone statistics for warm-core and cold-core eddies 44
  - 3.8.3 Discussion 45
- 3.9 Conclusions 46

4 SUMMARY AND CONCLUSIONS 47
- 4.1 Research question 1 47
- 4.2 Research question 2 48

II APPENDIX 51

A RESPONSE OF A TROPICAL CYCLONE TO A SUBSURFACE OCEAN EDDY AND THE ROLE OF BOUNDARY LAYER DYNAMICS 53
- A.1 Abstract 53
- A.2 Introduction 53
- A.3 ICON model description and simulation 56
- A.4 A conceptual framework for understanding tropical cyclone intensity change 57
- A.5 Tropical cyclone in the ICON simulation 60
  - A.5.1 Overview of the simulated tropical cyclone 61
  - A.5.2 Upper-ocean structure and sea-surface cooling 66
  - A.5.3 Influence of sea-surface cooling on surface latent heat flux 68
  - A.5.4 Equivalent potential temperature of ascending boundary layer air 69
  - A.5.5 Vertical mass flux 72
  - A.5.6 Updraught and inflow 73
  - A.5.7 Absolute angular momentum 73
  - A.5.8 Discussion 74
- A.6 The role of boundary layer dynamics for intensity 77
  - A.6.1 Slab boundary layer model 78
  - A.6.2 Results from the slab boundary layer model 79
  - A.6.3 Discussion of results from the slab boundary layer model 79
- A.7 Summary and conclusions 81
- A.8 Acknowledgements 82
- A.9 Appendix: Slab boundary layer model 82

B THE IMPACT OF OCEAN EDDIES ON TROPICAL CYCLONE INTENSITY IN A ONE-YEAR, GLOBAL COUPLED ATMOSPHERE-OCEAN SIMULATION 85

B.1 Abstract 85
B.2 Introduction 85
B.3 ICON model description and simulation 88
B.4 Algorithms for tracking tropical cyclones and identifying ocean eddies 89
  B.4.1 Tropical-cyclone tracking algorithm 89
  B.4.2 Eddy-identification algorithm 90
B.5 Tropical cyclone climatology 91
  B.5.1 Tracks 92
  B.5.2 Intensity and frequency 92
  B.5.3 Pressure-wind relationship 95
  B.5.4 Sea-surface cooling 95
  B.5.5 Tropical-cyclone-eddy encounters 96
B.6 Impact of ocean eddies on TC intensity 98
  B.6.1 Warm-core eddies 99
  B.6.2 Cold-core eddies 101
  B.6.3 Discussion 103
B.7 Summary and conclusion 103
B.8 Acknowledgements 105

BIBLIOGRAPHY 107

LIST OF FIGURES

Figure 1.1 Typhoon Maysak as seen from the International Space Station on 31st March 2015. Credits: European Space Agency and NASA. Source: `https://earthobservatory.nasa.gov/images/85630/typhoon-maysak-from-the-space-station`. Accessed on 30th March 2022. 3

Figure 1.2 Fields and villages submerged in the aftermath of the Bangladesh cyclone (1991). Credits: Sergeant Val Gempis (US Air Force). Source: `https://www.britannica.com/event/Bangladesh-cyclone-of-1991/images-videos`. Accessed on 30th March 2022. 4

Figure 1.3 Advisory issued by the National Hurricane Center in the United States for Hurricane Laura that includes a forecast cone showing the uncertainty in the track. The intensity is indicated by the letters D, S, H and M, which stand for tropical depression, tropical storm, hurricane and major hurricane, respectively. Credits: National Hurricane Center and the National Oceanic and Atmospheric Administration (NOAA). Source: `https://www.nhc.noaa.gov/images/cone_5day_with_wind.png`. Accessed on 30th March 2022. 6

Figure 1.4 Visualisation of a retrospective forecast of Hurricane Katrina run with the coupled atmosphere-ocean model developed by the Geophysical Fluid Dynamics Laboratory (GFDL). The visualisation shows the simulated cold wake trailing the hurricane and the disruption of the cold wake due to warm subsurface waters. Credits: NOAA/GFDL. Adapted from animation snapshot available on `https://www.gfdl.noaa.gov/visualizations-hurricanes/`. Accessed on 30th March 2022. 8

Figure 2.1 Cross section of a tropical cyclone. The large red arrows show the primary circulation rotating around the eye and the small red arrows show the updraught and outflow legs of the secondary circulation. The inflow leg of the secondary circulation towards the centre is not shown. There is also sinking air in the eye, which is indicated by the blue arrows. Credits: NASA. Source: `https://gpm.nasa.gov/education/articles/how-do-hurricanes-form`. Accessed 1st April 2022. 14

Figure 2.2 Schematic of the tropical cyclone circulation in the axisymmetric picture as a function of height and radius. In this case, the secondary circulation brings in M-surfaces radially inwards, which is referred to as spin up. The surface latent heat flux is associated with the evaporation of water, which is transported by the boundary layer. 15

Figure 2.3 Schematic of the tropical cyclone circulation showing key aspects of the rotating-convection paradigm in the axisymmetric picture. In the boundary layer, air parcels do not conserve M as they spiral inwards. Despite this, the strong inflow there means that the tangential velocity of boundary layer air parcels can locally exceed the tangential velocity above the boundary layer. At the radius of forced ascent, the boundary layer inflow turns upwards, corresponding to a vertical mass flux. The schematic is adapted from Montgomery et al. (2014). 17

Figure 2.4 Schematic of slab boundary layer model adapted from Montgomery et al. (2017). The slab extends vertically from the sea surface up to a height, h. The arrows show the orientation of the radial velocity, $u_b(r)$, and the vertical velocity out of the boundary layer, $w_b(r)$. The circle with the cross indicates the orientation of the tangential velocity, $v_b(r)$, into the page. The solutions, $u_b(r)$, $v_b(r)$ and $w_b(r)$ are a function of radius only. The red line indicates that the solution at a given radius only depends on the boundary layer flow and the tangential velocity at the top of the boundary layer, v(r), at larger radii. 20

Figure 2.5 Snapshots of SST in (a) the rapid intensification phase (RI), (b) CW1, (c) CW2 and (d) WF. The tropical cyclone is shown by the black circle and traverses northwards along the track indicated by the dotted line in all the snapshots. The partitions between the subphases are indicated with solid horizontal lines. The cold wake is evident from the region of low SST trailing the tropical cyclone. Note how the cold wake is disrupted in panel (d) and no longer within the circle directly under the tropical cyclone. 23

Figure 2.6 Ocean heat content prior to the arrival of the tropical cyclone. The horizontal surface current is shown in by the black arrows. The tropical cyclone traverses northwards along the track indicated by the dotted line. The partitions between the subphases are indicated with solid horizontal lines. The warm-core eddy is identifiable as the region of high ocean heat content WF section of the track that is centred on 30.5 °N 77 ° W. Note the rotational surface current that is characteristic of warm-core eddies. 24

Figure 2.7 Schematic of the processes outlined in the conceptual framework in the case of (a) intensification over a warm-core eddy and (b) decay over a cold wake. 26

Figure 2.8 Hovmöller plot of absolute angular momentum, M, and vertical velocity, w. The M contours at the top of the boundary layer at a height of 780 m is shown as a black contour. The M contours at a height of 620 m are shown as a yellow contour. The contours are displayed for (1.0, 1.5, 2.0, 2.5, 3.0, 3.5) × 10^6 m^2s^{-1}. The shading indicates w at 780 m according to the colorbar. Note how the radial interval where w exceeds 0.25 ms^{-1}, taken to be the region where air ascends into the eyewall updraught, move radially outwards during CW1 and CW2 and inwards during WF. The M contours within this radial interval also move radially outwards during CW1 and CW2 and inwards during WF. 29

Figure 2.9 The tangential velocity in the boundary layer, v_b, is displayed as a Hovmöller plot for the ICON (left) and the slab boundary layer model (right). For the ICON simulation, v_b represents a vertical average of tangential velocity over the lower 780 m in the atmosphere. In the slab boundary layer model, the solution for v_b breaks down at the radius where the radial velocity becomes zero. 32

Figure 3.1 Comparison between simulated monthly tropical-cyclone frequency across the globe with observations from 2020. The frequency for the simulated tropical cyclones is shown as a stacked bar chart sorted according to category. 40

Figure 3.2 Comparison between the simulated pressure-wind relationship and the observed pressure-wind relationship for 2020. 41

Figure 3.3 Snapshot of sea-surface height overlaid with red contours showing the ocean eddies identified by the algorithm. The surface current is displayed in both plots with black arrows scaled according to the magnitude. The solid black circles indicate the track points of the tropical cyclone, which encounters a large warm-core eddy (WCE4) in the Gulf of Mexico before making landfall further north. 43

Figure 3.4 Normalised histogram of the peak intensity, V_{max}, for warm-track and not-warm-track tropical cyclones. The mean for the warm-track tropical cyclones, μ_{WCE}, and not-warm-track tropical cyclones, μ, are given with their respective 95% confidence intervals. 44

Figure A.1 Schematic of the processes outlined in the conceptual framework in the case of (a) intensification over a warm-core eddy and (b) decay over a cold wake. 60

Figure A.2 The outgoing longwave radiation at a height of 30 km, corresponding to the model top, is shown for 132 hours after 31/08/2013 00:00 UTC. The tropical cyclone traverses along the trajectory (dotted line) to higher latitudes. The partitions between stages (see Table 1) are indicated with solid horizontal lines. Here, the data is plotted on the original triangular grid, and land cells are masked out in gray. 61

Figure A.3 Top: The 3-hour running mean of the maximum near-surface wind speed, V_{max}, and the minimum sea level pressure, P_{min}, are denoted by a solid line and a dashed line, respectively. Bottom: A blow-up of the maximum near surface wind speed in the mature phase (M). A description of the abbreviations is provided in Table 1. 62
Figure A.4 Horizontal snapshots of vertical velocity (blue and red shading) and tangential velocity (black contours) at a height of 5 km at (a) 92 hours, (b) 116 hours, (c) 136 hours, (d) 144 hours, (e) 152 hours and (f) 168 hours after 31/08/2013 00:00 UTC. For the tangential velocity, contours are shown for 35 ms^{-1}, 40 ms^{-1} and 50 ms^{-1}. The direction of the vertical wind shear, as defined by Kaplan et al. (2003), is indicated by the arrow. Radial grid lines are displayed for 50 km and 100 km. 63
Figure A.5 Azimuthal-mean of flow in tropical cyclone is shown as a 3-hour running mean for 92, 116, 136, 144, 152 and 168 hours after 31/08/2018 00:00 UTC. Contours of the updraught are shown by the solid black lines and correspond to (0.5, 1.0, 1.5) ms^{-1}. The single blue contour shows regions of downdraught. Angular momentum contours are displayed as solid green lines and increase from the centre outwards, corresponding to (1.0, 1.5, 2.0, 2.5, 3.0) $\times 10^6$ m^2s^{-1}. The blue and red shading indicates the inflow and outflow, respectively. The shading corresponds to, from light to dark, (2, 6, 10, 14) ms^{-1}. The radius of maximum vertical velocity is indicated by the black dashed line and the radius of maximum tangential velocity is shown as a green dashed line. 64
Figure A.6 Time series of the boundary layer height, h, displayed as a 3-hour running mean. 65
Figure A.7 Time series of (a) surface latent heat flux (LHF), (b) SST (solid line) and translational speed (V_{trans}) and (c) vertical wind shear. All variables are displayed as 3-hour running means. LHF and SST are averaged over an annulus which extends 10 km inside and 10 km outside the radius of maximum near-surface wind speed. The vertical wind shear is computed from the average horizontal wind vector over a circular anulus spanning a radial interval between 200 km and 800 km. 65
Figure A.8 Snapshots of (a) pre-storm ocean heat content (OHC) at 0 hours and SST at (b) 94 hours (RI), (c) 116 hours (RI/CW1), (d) 140 hours (CW2) and (e) 164 hours (WF) after 31/08/2013 00:00 UTC. The horizontal surface current is shown in (a) by the black arrows. The tropical cyclone traverses northwards along the trajectory indicated by the dotted line in all the snapshots. The position of the tropical cyclone is shown by the black circle. The partitions between the stages (see Table 1) are indicated with solid horizontal lines. The SST snapshots are plotted on the original triangular grid. 67

Figure A.9 Hovmöller plots of azimuthally averaged (a) SST, (b) moisture disequilibrium at the air-sea interface, (c) surface latent heat flux and (d) near-surface wind speed for the innermost 100 km. The spacing of the thin black contours for each of the plots are (a) 1 °C, (b) 1 gkg^{-1}, (c), 100 Wm^{-2} and (d) 2 ms^{-1}. The 3-hour running mean of the radius of maximum near-surface wind speed, $R_{surfmax}$, is shown as a thick solid black line in all four plots. 68

Figure A.10 The azimuthal-mean of equivalent potential temperature, $\overline{\theta_e}$, and vertical velocity are displayed as ((a) - (f)) six instantaneous, radius-height snapshots and (g) a Hovmöller plot at the boundary layer top at 780 m. The vertical snapshots are shown for (a) 92 hours, (b) 116 hours, (c) 136 hours, (d) 144 hours, (e) 152 hours and (e) 168 hours after 31/08/2013 00:00 UTC. The horizontal black lines ((a) - (f)) indicates the top of the boundary layer at 780 m. Note that the colorbar and contour values are identical for both the vertical snapshots and the Hovmöller plot. The spacing between the red $\overline{\theta_e}$ contours is 1 K in panels (a) - (f) and 2.5 K in panel (g). The thick black contours ((a) - (g)) correspond to an updraught of 0.25 ms^{-1} and 0.5 ms^{-1}. The bright yellow contour in panels (a) - (f) indicates the regions of downdraught (zero vertical velocity). For visual clarity the yellow contour is not included in panel (g). 70

Figure A.11 Time series of the azimuthal-mean equivalent potential temperature at 780 m averaged over all radii where vertical velocity exceeds 0.25 ms^{-1}, $\langle\overline{\theta_e}\rangle_{up}$, and the mean updraught radius where the vertical velocity exceeds 0.25 ms^{-1}, $\langle R\rangle_{up}$. Both variables are shown as a 3-hour running mean. 71

Figure A.12 Instantaneous horizontal snapshots of the downward flux of θ_e', DFX, (blue and red shading) and vertical velocity (black contours) at a height of 780 m at (a) 92 hours, (b) 116 hours, (c) 136 hours, (d) 144 hours, (e) 152 hours and (f) 168 hours after 31/08/2013 00:00 UTC. Contours are displayed for a vertical velocity of -0.1 ms^{-1} (dashed), 0.25 ms^{-1} (thick), and 0.5 ms^{-1} (thin). The direction of the vertical wind shear is indicated by the arrow. Radial grid lines are displayed for 50 km and 100 km. 72

Figure A.13 Upward mass fluxes averaged within a radius of 60 km are shown as a 3-hour running mean for a height of 780 m (blue) and 5 km (red). 73

Figure A.14 Azimuthal-mean of secondary circulation shown as a 3-hour running mean for 92, 116, 136, 144, 152 and 168 hours after 31/08/2018 00:00 UTC. The red shading indicates the magnitude of vertical velocity. Inflow contours are displayed as blue lines, corresponding to (0.0,0.5,1.0,2.0,5.0,10.0) ms^{-1}. 74

Figure A.15 Hovmöller plot of angular momentum (M) and vertical velocity. The M contours at a height of 780 m and 620 m are shown as black and yellow lines, respectively. The contours are displayed for (1.0, 1.5, 2.0, 2.5, 3.0, 3.5) × 10^6 m^2s^{-1}. The shading indicates the vertical velocity at 780 m according to the colorbar. 75

Figure A.16 The tangential velocity in the boundary layer, v_b, is displayed as a Hovmöller plot for the ICON (left) and the slab boundary layer model (right). For the ICON simulation, v_b represents a vertical average of tangential velocity over the lower 780 m in the atmosphere. 79

Figure A.17 The radial velocity in the boundary layer, u_b, is displayed as a Hovmöller plot for the ICON simulation (left) and the slab boundary layer model (right). For the ICON simulation, u_b represents a vertical average of tangential velocity over the lower 780 m in the atmosphere. 80

Figure B.1 Schematic of the 9x9 filter adapted from Matsuoka et al., 2016. Each square represents a single grid cell. If the eddy is associated with an SSH minimum, the SSH successively increases from the central cell (black) outwards for each of the 8 paths (arrows) separately. SSH values on different paths are not compared. If the eddy is associated with an SSH maximum, the SSH successively decreases along the same paths. 91

Figure B.2 Two plots of the ocean eddies identified for a single track off the west coast of Mexico overlaid on a) the Okubo-Weiss parameter and b) the sea surface height. The inner- and outer-eddy contours are shown as thin and thick loops, respectively. The surface current is displayed in both plots with black arrows scaled according to the magnitude. The track points are also indicated in both plots by solid black circles. 92

Figure B.3 Global map of tropical cyclone tracks in the simulation. The black marker denotes the location at which each tropical cyclone is initially detected. The tracks are colour-coded according to the peak intensity reached by the tropical cyclone over its lifetime. 93

Figure B.4 Comparison between simulated monthly tropical-cyclone frequency across the globe with observations from 2020. The frequency for the simulated tropical cyclones is shown as a stacked bar chart sorted according to category. Observed values for 2020 are shown as black dots. Observations are taken from the same source as for Table 2. 94

Figure B.5 Comparison between the simulated pressure-wind relationship and the observed pressure-wind relationship for 2020. The observations are taken from the same source as in Table 2. 96

Figure B.6 Simulated sea-surface cooling averaged across all tropical cyclones of the same category. Prior to averaging, all the time series are centred on the time step where sea-surface cooling is strongest, i.e. ΔSST is most negative. 97

Figure B.7 Scatter plot of track-averaged sea-surface cooling plotted against the maximum near-surface wind speed obtained by the tropical cyclone. The vertical lines represent the binned averages and the standard deviations for each category. 97

Figure B.8 Grouped bar chart showing the number of tropical cyclones that encounter n ocean eddies, where n = 0, 1, 2, 3, 4 and 5. The grey bars display the number of tropical cyclones that encounter a total of n ocean eddies, where n is a sum of the number of warm-core eddies (WCEs) and cold-core eddies (CCEs). The red and blue bars display the number of tropical cyclones that encounter a total of n WCEs and n CCEs, respectively. The exact numbers are displayed on top of each bar. 98

Figure B.9 Normalised histogram of the peak intensity, V_{max}, for warm-track and not-warm-track tropical cyclones. The mean for the warm-core-track tropical cyclones, μ_{WCE}, and not-warm-track tropical cyclones, μ, are given with their respective 95% confidence intervals. 99

Figure B.10 Four panel plots comparing warm-track tropical cyclones with not-warm-track tropical cyclones. Panel a) is a histogram of the track-averaged surface latent heat flux, $\overline{LHF}$. Panel b) is a scatter plot of the peak intensity, V_{max}, against $\overline{LHF}$. Panel c) is a histogram of the track-averaged sea-surface cooling, $\overline{\Delta SST}$. Panel d) is a scatter plot of V_{max} against $\overline{\Delta SST}$. The correlation coefficients, lines of best fit and corresponding 95% confidence intervals are shown for the scatter plots. The means for the histograms are indicated at the top of panel a) and panel c). 100

Figure B.11 Same as Figure B.9 but for cold-track and not-cold-track tropical cyclones. 101

Figure B.12 Same as Figure B.10 but for cold-track and not-cold-track tropical cyclones. 102

LIST OF TABLES

Table 1 A list of phases that the simulated tropical cyclone undergoes during its life cycle. 63

Table 2 Table comparing the simulated frequency of tropical cyclones and simulated accumalated cyclone energy with observations. Note that the simulated time period starts on 21st January 2020 and ends on 21st January 2021, whereas the observed values refer strictly to the year 2020. The observational data is taken from: NOAA National Centers for Environmental Information, State of the Climate: Tropical Cyclones for Annual 2020, published online January 2021, retrieved on April 20, 2021 from `https://www.ncdc.noaa.gov/sotc/tropical-cyclones/202013`. 93

Part I

UNIFYING ESSAY

1

INTRODUCTION

Tropical cyclones loom large in the public imagination as highly destructive rotating storm systems. These storms are hundreds, sometimes even more than a thousand, kilometres wide. Images of tropical cyclones taken from space allow one to truly get a sense of their vast scale.

The energy that powers tropical cyclones comes from the ocean. As we shall see later on, the world's oceans harbour their own rotating systems, which influence the formation of tropical cyclones.

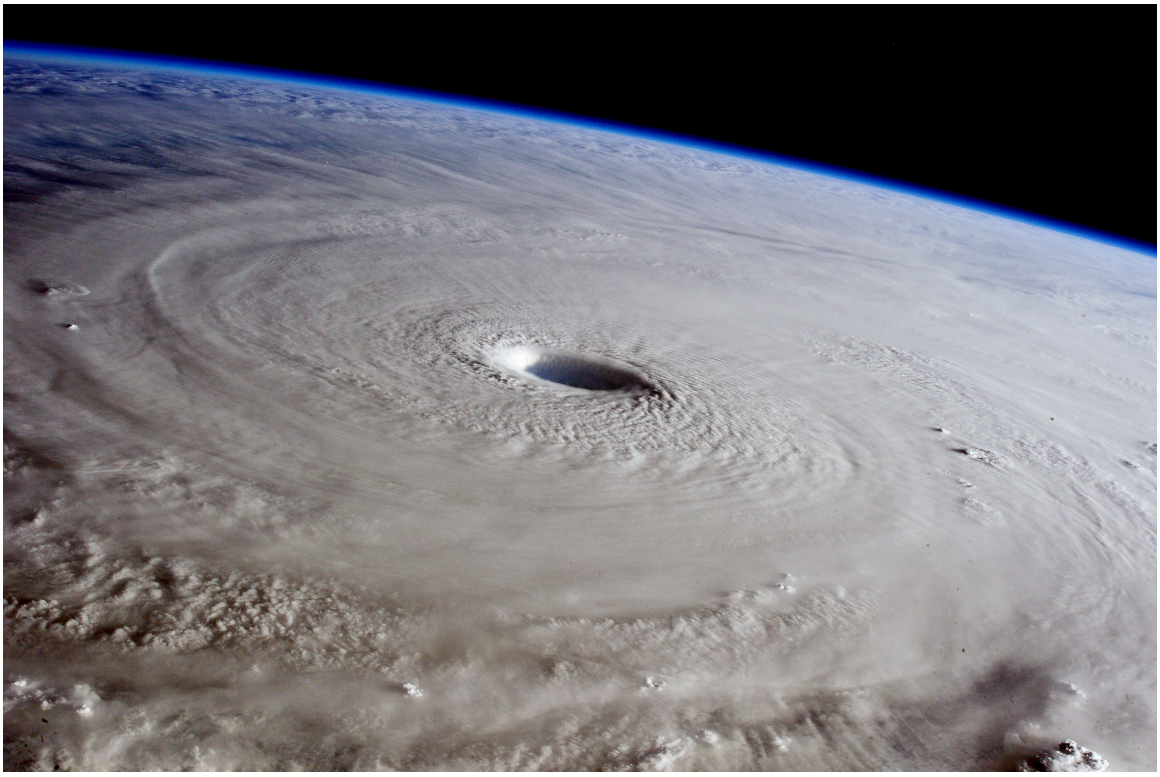

Figure 1.1: Typhoon Maysak as seen from the International Space Station on 31st March 2015. Credits: European Space Agency and NASA. Source: `https://earthobservatory.nasa.gov/images/85630/typhoon-maysak-from-the-space-station`. Accessed on 30th March 2022.

1.1 TROPICAL CYCLONES AND SOCIETY

More commonly known as hurricanes in the North Atlantic and North East Pacific, typhoons in the western Pacific, and cyclones in the Indian Ocean, tropical cyclones have instilled fear in those unfortunate enough to have crossed their path through the ages.

Sailors across the world were only too familiar with the dangers of being caught up in these violent storms, where towering waves threaten to swallow any ship not already toppled by the seemingly relentless high winds. Kublai Khan's attempt to invade Japan was thwarted not once, but twice by tropical cyclones that sunk his entire fleet (Emanuel, 2005).

Tropical cyclones cause tremendous loss of life when they make landfall. Nowhere is the human cost of tropical cyclones more severe than in Bangladesh (Ali, 1999). Although Bangladesh is directly hit by only 1% of all tropical cyclones on average, it accounts for around 50% of the global casualties due to tropical cyclones. A glance at the staggering death tolls associated with tropical cyclones in recent history brings the scale of the human tragedy into sharp relief. Between 300,000 and 500,00 people lost their lives when the Bhola cyclone (1970) hit the coast of Bangladesh (Alam et al., 2015; Frank et al., 1971). More recently, the Bangladesh cyclone (1991) claimed around 138,000 lives (Ali, 1999).

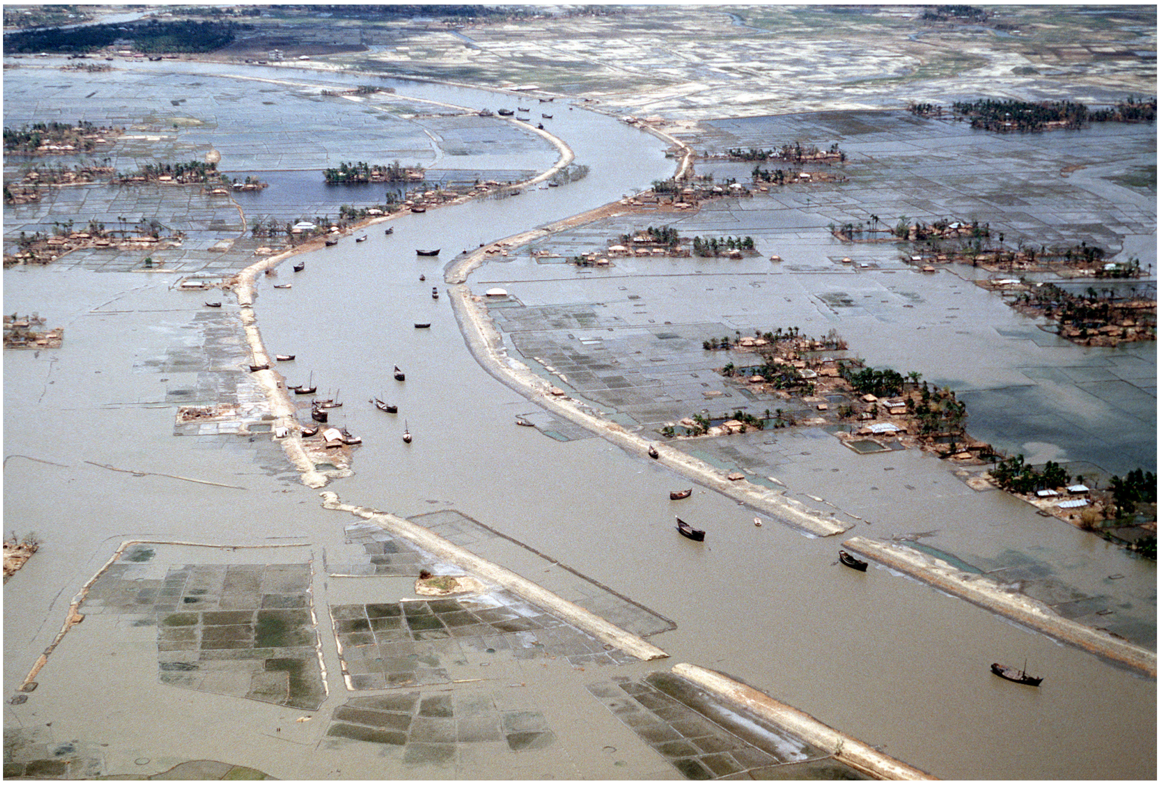

Figure 1.2: Fields and villages submerged in the aftermath of the Bangladesh cyclone (1991). Credits: Sergeant Val Gempis (US Air Force). Source: https://www.britannica.com/event/Bangladesh-cyclone-of-1991/images-videos. Accessed on 30th March 2022.

Deadly tropical cyclones are not limited to Bangladesh. Counting together the official deaths and the missing, a total of 138,000 perished in Myanmar due to Cyclone Nargis (2008) (Seekins, 2009). Typhoon Nina (1975) caused the Banqiao Dam in China to burst, leading to 26,000 direct fatalities and at least another 100,000 fatalities as a result of ensuing famine and disease (Yang et al., 2017). Further afield, Hurricane Mitch (1998) led to approximately 11,000 deaths in Central America (Hellin et al., 1999).

Tropical cyclones are not only responsible for a large loss of life but also for widespread damage due to high wind speeds, storm surges and torrential rainfall. Bangladesh is extremely vulnerable to storm surges, with only 10% of the total area lying at least 1 m above the mean sea level (Karim et al., 2008). Storm surges that swept away villages during the Bhola cyclone (1970) coincided with the spring high tide resulting in water levels 10 m above the mean sea level. A combination of a storm surge, heavy rainfall and high winds during Hurricane Katrina (2005) left behind a trail of destruction, with 204,000 residential properties rendered uninhabitable, damaged or destroyed, costing an estimated US$16 billion (Pistrika et al., 2010). The damage caused by tropical cyclones is not limited to coastal communities, but aso affects populations further inland. In China, where tropical cyclones incur damages equivalent to 0.38% of the annual total gross domestic product, the devastation caused by flooding and landslides extend into landlocked provinces, such as Hunan and Jiangxi (Zhang et al., 2009).

1.2 OPERATIONAL TRACK AND INTENSITY FORECASTING

Early warning systems are crucial to minimising the loss of life and economic damage unleashed by tropical cyclones by enabling local authorities to adequately prepare local communities that lie in the path of the tropical cyclone. In Bangladesh, early warning systems were instrumental in evacuating 3 million people before the arrival of Cyclone Sidr (2007) (Rogers et al., 2010). The timely evacuation along with the increase in the number of tropical cyclone shelters over the previous decade limited the death toll to 4000 - a much lower figure compared to the 138,000 who perished during the similarly destructive Bangladesh Cyclone (1991) (Paul et al., 2010).

Warnings for tropical cyclones are issued on both a national and international level. At the international level, the World Meteorological Organisation (WMO) has set up a global network of 5 Regional Specialized Meteorological Centers (RSMC) that issue tropical-cyclone related advisories (Zschau et al., 2003). While many countries have their own national meteorological centres for this purpose, the RSMCs allow countries to pool their resources to optimise the generation and communication of these advisories.

Advisories are underpinned by operational forecasts. The primary aim of operational forecasts is to accurately predict the path taken by the tropical cyclone, known as the track, and its maximum near-surface wind speed at any given time, otherwise known as intensity. Nowadays, most operational forecasts include a representation of uncertainty in the predicted track and intensity (Titley et al., 2019). Reducing these uncertainties for the forecasted track and intensity is necessary to improve the accuracy of advisories on a local level that not only relate to the threats posed by high wind speeds, but also to the risk of heavy rainfall and storm surges along the coastline.

Operational forecasting relies heavily on numerical modelling [1]. The type of numerical models used for forecasting are known as numerical weather prediction (NWP) models. These NWP models are used to simulate tropical cyclones directly by dynamically solving the equations that govern fluid dynamics on a discrete, three-dimensional grid. Physical processes that occur on scales smaller than the grid spacing are not resolved. Sub-grid processes that are important for the conservation of energy and mass in the model are ac-

---

[1] Statistical models also exist that are based on empirical data, such as the tropical cyclone climatology of the region (Demaria et al., 1994)

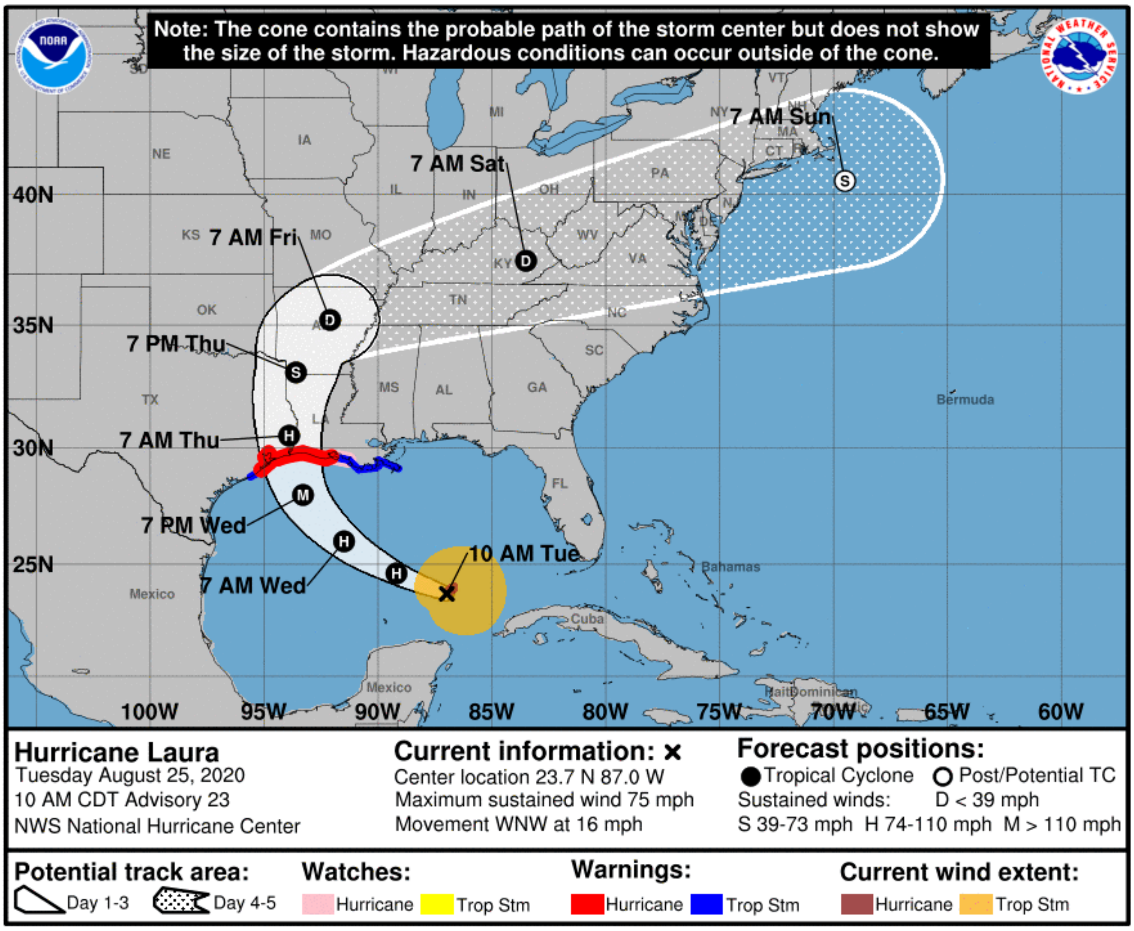
Note: The cone contains the probable path of the storm center but does not show the size of the storm. Hazardous conditions can occur outside of the cone.
7 AM Sun
7 AM Sat
7 AM Fri
7 PM Thu
7 AM Thu
7 PM Wed
7 AM Wed
10 AM Tue
40N
35N
30N
25N
100W
95W
90W
85W
80W
75W
70W
65W
60W
NE
IA
MI
KS
MO
IL
IN
OH
PA
NY
VT
MA
CT
RI
NJ
DE
MD
WV
VA
KY
TN
NC
SC
OK
AR
TX
LA
MS
AL
GA
FL
Bermuda
Bahamas
Cuba
Mexico
Haiti
Dominican
Hurricane Laura
Tuesday August 25, 2020
10 AM CDT Advisory 23
NWS National Hurricane Center
Current information: ×
Center location 23.7 N 87.0 W
Maximum sustained wind 75 mph
Movement WNW at 16 mph
Forecast positions:
● Tropical Cyclone ○ Post/Potential TC
Sustained winds: D < 39 mph
S 39-73 mph H 74-110 mph M > 110 mph
Potential track area:
Day 1-3
Day 4-5
Watches:
Hurricane
Trop Stm
Warnings:
Hurricane
Trop Stm
Current wind extent:
Hurricane
Trop Stm

Figure 1.3: Advisory issued by the National Hurricane Center in the United States for Hurricane Laura that includes a forecast cone showing the uncertainty in the track. The intensity is indicated by the letters D, S, H and M, which stand for tropical depression, tropical storm, hurricane and major hurricane, respectively. Credits: National Hurricane Center and the National Oceanic and Atmospheric Administration (NOAA). Source: `https://www.nhc.noaa.gov/images/cone_5day_with_wind.png`. Accessed on 30th March 2022.

counted for with parameterisations, which represent a simplification of a physical process (Bauer et al., 2015).

Increasing computational power has enabled the simulation of tropical cyclones in NWP models with successively smaller grid spacing (Bender et al., 2007). As the grid spacing reduces, a number of small-scale processes are directly resolved and no longer have to be parameterised. On the one hand, removing parameterisations has the advantage that the simulated physical processes reflect the current understanding more closely and can improve forecasts by increasing the realism of simulated tropical cyclones (Klemp, 2006). On the other hand, removing parameterisations comes at the price of increasing model complexity due to the increasing range of scales at which processes are resolved. The increasing model complexity makes it more difficult to understand the behaviour of the model and harder to identify and rectify errors (Stensrud, 2007).

Decreasing grid spacing alone is not sufficient to improve the simulation of tropical cyclones in NWP models. The limitations of decreasing grid spacing are illustrated by the relatively small progress made in operational intensity forecasts compared to track forecasts (DeMaria et al., 2014). The track is primarily determined by the large-scale background atmospheric flow, which steers the tropical cyclone. The progress in track forecasting largely reflects the improved ability of numerical models to predict the large-scale background atmospheric flow. The intensity by contrast depends on small-scale processes, such as convection, as well as large-scale processes. Despite the decrease in grid spacing and the resolution of such small-scale processes, intensity forecasting has not undergone a level of improvement comparable to track forecasting (ibid.).

Improving intensity forecasts further hinges on advancing our scientific understanding of the physical processes that determine tropical cyclone intensity. Advancing our understanding of these processes helps guide the development of the NWP models used for intensity forecasts. Intensity forecasts can then be improved by ensuring that these processes are adequately represented in NWP models and lead to tropical cyclones with a more realistic structure (Gopalakrishnan et al., 2021; Gopalakrishnan et al., 2013). Assessing the realism of these processes and the simulated tropical cyclone is especially important, given the increasing complexity of NWP models that has accompanied the increase in computational power.

1.3 THE NEGATIVE FEEDBACK AND COUPLED MODELS

One key physical process for intensity forecasts is the evaporation of water at the sea surface. The evaporation of water is associated with a flux of energy from the ocean to the atmosphere, known as the surface latent heat flux. The surface latent heat flux is important for tropical cyclone intensity, because the surface latent heat flux, and hence the ocean, is the primary source of energy for the tropical cyclone (Emanuel, 1986).

The surface latent heat flux depends on the air-sea interface, a thin vertical region encompassing the sea surface and the air directly above. In NWP models, the surface latent heat flux, Q_l, is often parameterised using the bulk air-sea formula (Smith, 1988) and is given by

$$Q_l = \rho_a L_v C_q U_{10}(q_s - q_a), \tag{1.1}$$

where ρ_a, L_v, C_q, U_{10} and (q_s - q_a) are the density of air, the latent heat of vaporisation, the exchange coefficient, the wind speed 10 m above the sea surface and the moisture disequilibrium, respectively (Jaimes et al., 2021). The moisture disequilibrium is equal to the saturation specific humidity at the sea surface temperature, q_s, minus the specific humidity of the air 10 m above the sea surface, q_a. The saturation specific humidity is a monotonously increasing function of sea surface temperature (SST). Simply put, if the SST increases, so does the saturation specific humidity and vice versa.

From the above formula, one can see that the surface latent heat flux decreases if the SST decreases. A decrease in the SST corresponds to a decrease in q_s, which in turn reduces the moisture disequilibrium and, ultimately, the surface latent heat flux. Here we assume that the other variables remain unchanged. In reality, the change in surface latent heat flux is more complicated, because the other variables also vary in time.

A decrease in SST occurs in the presence of tropical cyclones. High wind speeds at the air-sea interface exert a stress force on the sea surface. The wind stress causes the churning of the upper ocean, which brings cold water to the sea surface (Chang et al., 1978; Price, 1981). As the tropical cyclone moves along its track, the resultant cooling of the sea surface trails the tropical cyclone and is correspondingly referred to as the cold wake.

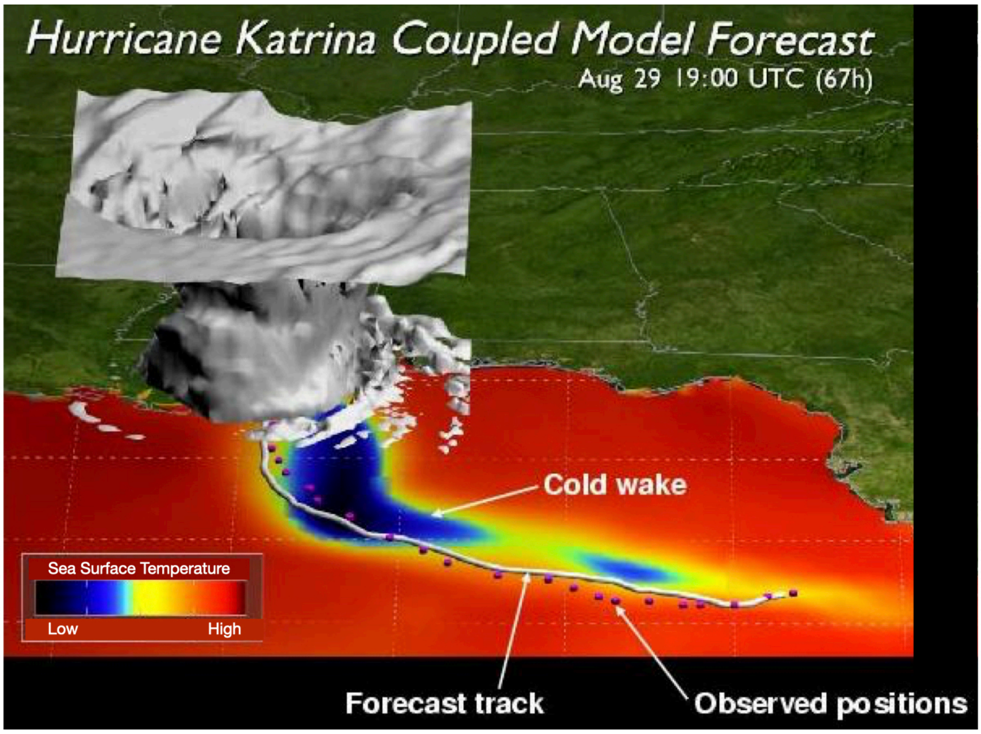

Figure 1.4: Visualisation of a retrospective forecast of Hurricane Katrina run with the coupled atmosphere-ocean model developed by the Geophysical Fluid Dynamics Laboratory (GFDL). The visualisation shows the simulated cold wake trailing the hurricane and the disruption of the cold wake due to warm subsurface waters. Credits: NOAA/GFDL. Adapted from animation snapshot available on `https://www.gfdl.noaa.gov/visualizations-hurricanes/`. Accessed on 30th March 2022.

The relationship between sea surface cooling and tropical cyclone intensity is often conceptualised as a negative feedback (Chang et al., 1979). As the tropical cyclone intensifies, the increasing wind stress on the sea surface induces sea-surface cooling. The sea-surface cooling decreases the moisture disequilibrium by reducing q_s. Assuming the sea-surface cooling is strong enough, such that the decrease in moisture disequilibrium dominates over the increase in wind speed, the surface latent heat flux decreases. This decrease in surface latent heat flux prevents the tropical cyclone from intensifying further and can also lead to a subsequent decrease in intensity. In this sense, the negative feedback acts as a brake on tropical cyclone intensity.

Simulating the negative feedback in intensity forecasts requires coupled atmosphere-ocean NWP models, which capture the churning of the upper ocean and the ensuing sea-surface cooling. Recognition of the importance of the negative feedback for intensity forecasting is reflected in the transition from atmosphere-only to coupled atmosphere-ocean NWP models. Aided by increasing computational power, this transition has led to a considerable improvement in intensity forecasting (Balaguru et al., 2018; Bender et al., 2000; Mogensen et al., 2017).

1.4 SUBSURFACE OCEAN STRUCTURE AND WARM-CORE EDDIES

The negative feedback simulated in coupled NWP models depends on the representation of the subsurface ocean. The upper most layer in the ocean is the mixed layer. The churning of cold water at the bottom of the mixed layer causes the mixed layer to cool, which in turn cools the sea surface (Price, 1981). However, if the mixed layer is warm and deep, the large heat content associated with the mixed layer reduces the cooling (Leipper et al., 1972; Shay, 2019). By reducing the sea-surface cooling, the region of large heat content weakens the negative feedback, allowing the tropical cyclone to intensify further. Due to the effect of the subsurface ocean on sea-surface cooling and the negative feedback, the subsurface ocean structure is of first-order importance for intensity forecasting (Emanuel, 1999).

The structure of the subsurface ocean is not homogeneous, but is shaped by background oceanic features. One feature that is pertinent for intensity forecasting are warm-core eddies. These are highly localised rotating masses of water that possess a mixed layer that is warmer and deeper than that of the surrounding environment. Correspondingly, the heat content of the mixed layer in warm-core eddy exceeds that of the surrounding environment. When a tropical cyclone encounters a warm-core eddy, the sudden increase in the heat content in the mixed layer suppresses the sea-surface cooling and weakens the negative feedback (Ali et al., 2007; Shay et al., 2000; Wu et al., 2007a).

One notable example is Hurricane Katrina, which encountered a warm-core eddy in the Gulf of Mexico (Kafatos et al., 2006; Scharroo et al., 2005). Following the suppression of the sea-surface cooling, Katrina experienced multiple instances of rapid intensification, defined as an increase in intensity of 15 ms^{-1} over any 24-hour period (Jaimes et al., 2016). Hurricane Opal (1995) also experienced rapid intensification after encountering a warm-core eddy in the Gulf of Mexico (Shay et al., 2000). Further afield, the rapid intensification of Supertyphoon Maemi (2003) in the northwest Pacific and Cyclone Nargis (2008) in the Indian Ocean has been directly attributed to the presence of warm-core eddies (Lin et al., 2009; Lin et al., 2005).

Tropical cyclones that undergo rapid intensification are especially dangerous, because they are notoriously difficult to forecast (DeMaria et al., 2021; Na et al., 2018; Trabing et al., 2020). Moreover, rapidly intensifying tropical cyclones give communities in the path of the tropical cyclone less time to prepare. Given the danger posed by rapidly intensifying tropical cyclones, the impact of warm-core ocean eddies on tropical cyclone intensity has attracted growing attention in the scientific community (Lin et al., 2013).

1.5 NUMERICAL MODELS FOR STUDYING THE IMPACT OF WARM-CORE EDDIES

Our understanding of how warm-core eddies influence tropical cyclone intensity hinges on our understanding of the negative feedback between tropical cyclone intensity and sea-surface cooling. We know that the negative feedback is important, because intensity forecasting is improved when using coupled atmosphere-ocean models that simulate sea-surface cooling rather than atmosphere-only models that do not. It is also clear that warm-core ocean eddies can weaken this negative feedback and result in more intense tropical cyclones compared to the case where the warm-core eddy is absent. However, there is a lack of understanding about the mechanisms that determine the strength of this negative feedback and how these mechanisms are affected by warm-core eddies.

The complexity of the physical processes underlying the negative feedback means that numerical models similar to NWP models that capture these complexities represent an invaluable tool for studying the negative feedback. A hierarchical approach with coupled and uncoupled numerical models provides a way of teasing apart the mechanisms that determine the impact of warm-core eddies on the strength of the negative feedback and, ultimately, the tropical cyclone intensity. Atmosphere-only models provide insight into how tropical cyclones intensify when the properties of the sea surface are prescribed. Ocean-only models allow one to isolate the effect tropical cyclones have on the sea-surface and the subsurface ocean structure, including warm-core eddies, by prescribing the atmospheric conditions of the tropical cyclone at the sea surface. Finally, coupled atmosphere-ocean models reveal the influence of the two-way interaction between atmosphere and ocean.

1.6 RESEARCH OBJECTIVES

1.6.1 *Overarching goal*

The overarching goal of my thesis is to advance the scientific understanding of how warm-core eddies affect tropical cyclone intensity through the lens of the negative feedback. To this end, I analyse simulations of tropical cyclones that encounter warm-core eddies. These simulations are run with a coupled atmosphere-ocean model that captures both the negative feedback and the full range of complex physical processes that are present in NWP models. With the insights provided by these simulations, I aim to contribute to an improvement in intensity forecasting by providing a reference point that can help assess the realism of the simulated interaction between warm-core eddies and tropical cyclones in NWP models. Additionally, I seek to further understanding of the limitations of climate simulations, which are used to project future changes in tropical cyclone intensity.

1.6.2 *Research question 1*

In the first part of my thesis, I use a coupled atmosphere-ocean model to study how the strength of the negative feedback changes when a single tropical cyclone encounters a warm-core eddy. Here, I focus on the dynamics of the air flow in the lowermost vertical layer in the tropical cyclone, known as the boundary layer. Boundary layer dynamics have been shown to be important for both the intensification and decay of tropical cyclones in atmosphere-only models (Montgomery et al., 2017). However, the role of boundary layer dynamics has not been investigated in coupled atmosphere-ocean models, which are required to simulate the negative feedback. For this reason, it remains unclear what the role of boundary layer dynamics plays for the strength of the negative feedback and the tropical cyclone intensity response to a warm-core eddy. Accordingly, my first research question is:

Are boundary layer dynamics important for the negative feedback and the tropical cyclone intensity response to a warm-core eddy in coupled atmosphere-ocean models?

Answering this research question helps guide the development of NWP models used in intensity forecasting. The intensity of simulated tropical cyclones is highly sensitive to the choice of boundary layer scheme, which is required to parameterise physical processes in the boundary layer (Gopalakrishnan et al., 2013; Smith et al., 2014; Srinivas et al., 2008). The choice of boundary layer scheme has also been shown to affect whether numerical models correctly predict the rapid intensification of historical tropical cyclones, including that of Cyclone Nargis, which encountered a warm-core eddy in the Bay of Bengal (Rai et al., 2018; Raju et al., 2011; Zhang et al., 2017b). However, there is still no consensus on the optimal boundary layer scheme for intensity forecasting (Kepert, 2012; Smith et al., 2010a). Advancing the scientific understanding of the role played by boundary layer dynamics for the negative feedback allows the forecasting community to make informed choices as to which boundary layer scheme is appropriate for simulating tropical cyclones in coupled NWP models. Choosing the appropriate boundary layer scheme in coupled models is key to improving intensity forecasts of rapidly intensifying tropical cyclones, including those tropical cyclones that encounter warm-core eddies.

1.6.3 *Research question 2*

In the second part of my thesis, I use the same coupled atmosphere-ocean model to explore the impact of both warm-core eddies and cold-core eddies on tropical cyclone intensity on a global scale. In contrast to warm-core eddies, cold-core eddies strengthen the negative feedback by enhancing sea-surface cooling. Warm-core and cold-core eddies, together referred to as ocean eddies, are, similar to tropical cyclones, not evenly distributed across the globe, but tend to be found near strong ocean currents (Olson, 1991). In the same way tropical cyclones are steered by the background atmospheric flow, ocean eddies are carried by the background oceanic flow. Satellite altimetry allows cold-core and warm-core eddies to be tracked in real time (Chelton et al., 2007). However, satellites measurements cannot reveal the subsurface ocean structure (Brokaw et al., 2020). Instead, in situ measurements are required. While the global coverage of in situ measurements have increased in the last couple of decades, their spatial density is not high enough to resolve the subsurface structure of ocean eddies on a global scale in real time (Jayne et al., 2017; Li et al., 2021).

The varying spatial distribution of ocean eddies and the lack of subsurface measurements make it difficult to predict the frequency with which tropical cyclones encounter ocean eddies on a global scale. Moreover, it is unclear whether tropical cyclones that encounter warm-core eddies reach on average higher peak intensities compared to those that do not encounter warm-core eddies. Conversely, one does not know whether tropical cyclones that encounter cold-core eddies reach on average lower peak intensities compared to those that do not encounter cold-core eddies. To overcome this difficulty, one can analyse a global simulation run with a coupled atmosphere-ocean model that has both small enough grid spacing to resolve tropical cyclones and warm-core eddies and a reasonable representation of subsurface oceanic features, including ocean currents. Analysing the effect of ocean eddies on tropical cyclone intensity with such a global, coupled atmosphere-ocean model has not been done before (Knutson et al., 2020). Access to such a simulation places me in a unique position to answer my second research question:

What is the impact of ocean eddies on tropical cyclone intensity on a global scale in a coupled atmosphere-ocean model?

Answering the second research question contributes to wider efforts to predict future changes in tropical cyclone intensity due to climate change. A majority of climate change studies project an increase in the frequency of intense tropical cyclones (ibid.). However, the longer temporal scales and larger spatial scales mean that climate simulations that underpin these projections tend to be run with atmosphere-only models or coupled models with a very large grid spacing. Consequently, climate simulations do not currently have a representation of ocean eddies. If ocean eddies do have a sizeable impact on tropical cyclone intensity in the one-year simulation, this suggests that climate simulations underpinning projected increases in the frequency of intense tropical cyclones may be biased.

2

THE ROLE OF BOUNDARY LAYER DYNAMICS

The negative feedback is not only sensitive to the subsurface ocean structure, which influences the strength of sea-surface cooling, but also depends on the relationship between surface latent heat flux and tropical cyclone intensity. The decrease in tropical cyclone intensity for a given reduction in surface latent heat flux is modulated by changing thermodynamic and dynamical structure of the tropical cyclone's circulation. One aspect of the tropical cyclone circulation that has not been investigated in coupled models is boundary layer dynamics.

Before diving into the role of boundary layer dynamics for tropical cyclone intensity, I describe the structure of the tropical cyclone circulation and its relevance to tropical cyclone intensity in Section 2.1. In this description, I intentionally omit the role of boundary layer dynamics. With reference to this incomplete description of the tropical cyclone circulation, I summarise the current understanding of how tropical cyclones decay in coupled models in Section 2.2. Then I discuss the role of boundary layer dynamics for tropical cyclone intensity in atmosphere-only models in Section 2.3. In Section 2.4, I outline the motivation for investigating the role of the boundary layer dynamics in coupled models and reintroduce the first research question. In the subsequent sections, I present the work I have done before providing an answer to the first research question.

2.1 TROPICAL CYCLONE CIRCULATION

Tropical cyclones are vortices spinning in a cyclonic sense, i.e. anticlockwise in the Northern Hemisphere and clockwise in the Southern Hemisphere. As with other vortices, the largest component of velocity of the air is in the tangential direction. This tangential circulation is commonly referred to as the primary circulation. The primary circulation is not constant throughout the tropical cyclone, but varies with radius. The eye at the low pressure centre of the tropical cyclone is calm with low tangential velocity. The tangential velocity increases rapidly moving from the centre towards the rapidly rotating eyewall. After reaching a maximum near the eyewall, the tangential velocity tails off with increasing radius.

The primary circulation is accompanied by a transverse, overturning circulation, known as the secondary circulation. This secondary circulation consists of a region of inflow, updraught and outflow. The inflow brings air radially inwards from the surrounding environment towards the centre of the tropical cyclone, where it then rises in the eyewall updraught before being ejected and moves radially outwards in the outflow region.

The circular motion of the primary circulation gives rise to angular momentum. The absolute angular momentum of an air parcel, M, consists of a background contribution due to the Earth's rotation and a term depending on the tangential velocity, v(r), and the radius from the centre, r. The expression for M is

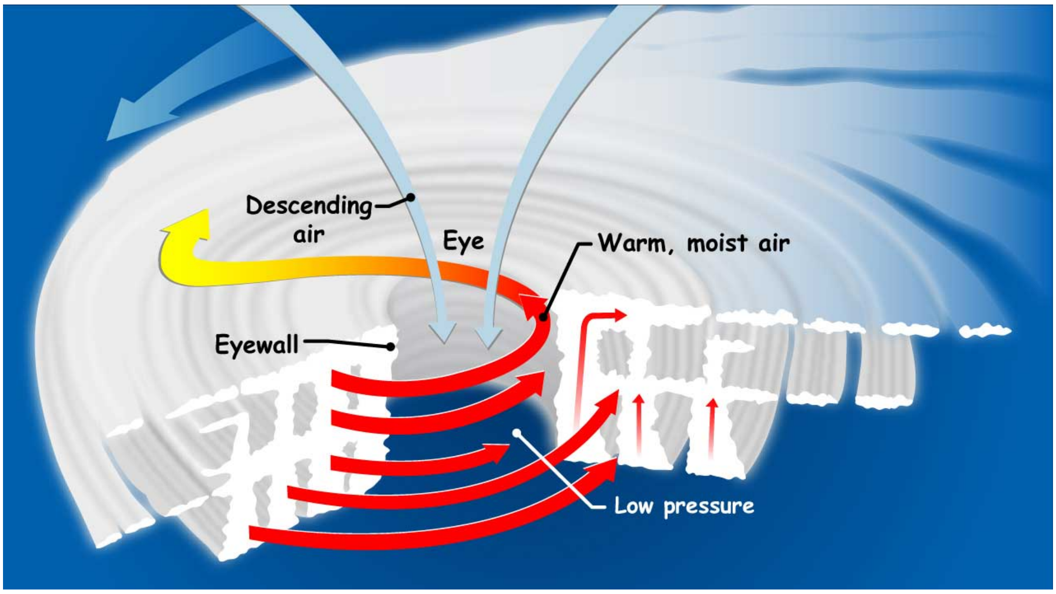

Figure 2.1: Cross section of a tropical cyclone. The large red arrows show the primary circulation rotating around the eye and the small red arrows show the updraught and outflow legs of the secondary circulation. The inflow leg of the secondary circulation towards the centre is not shown. There is also sinking air in the eye, which is indicated by the blue arrows. Credits: NASA. Source: `https://gpm.nasa.gov/education/articles/how-do-hurricanes-form`. Accessed 1st April 2022.

$$M = rv(r) + \frac{1}{2}fr^2, \tag{2.1}$$

where f denotes the Coriolis parameter. We can rearrange this expression into the following form,

$$v(r) = \frac{M}{r} - \frac{1}{2}fr. \tag{2.2}$$

From this expression, we can see that tangential velocity increases if M is held constant and r decreases [1]. This increase in tangential velocity with constant M and decreasing radius is, in simple terms, how tropical cyclones intensify. Air parcels in the tropical cyclone conserve M as they move to smaller radii, increasing their tangential velocity in the process. The radial movement of these air parcels is determined by the secondary circulation. The radial movement of M associated with these air parcels can be visualised as surfaces of constant M being advected by the secondary circulation. If the secondary circulation brings M-surfaces radially inwards, the tropical cyclone spins up. If the secondary circulation leads to M-surfaces moving radially outwards, the tropical cyclone spins down.

The secondary circulation cannot exist without a source of energy. The source of energy is the surface latent heat flux associated with the evaporation of water at the sea surface.

---

[1] Note that r does not go to zero, because the air in the inflow goes up into the eyewall updraught before reaching the centre.

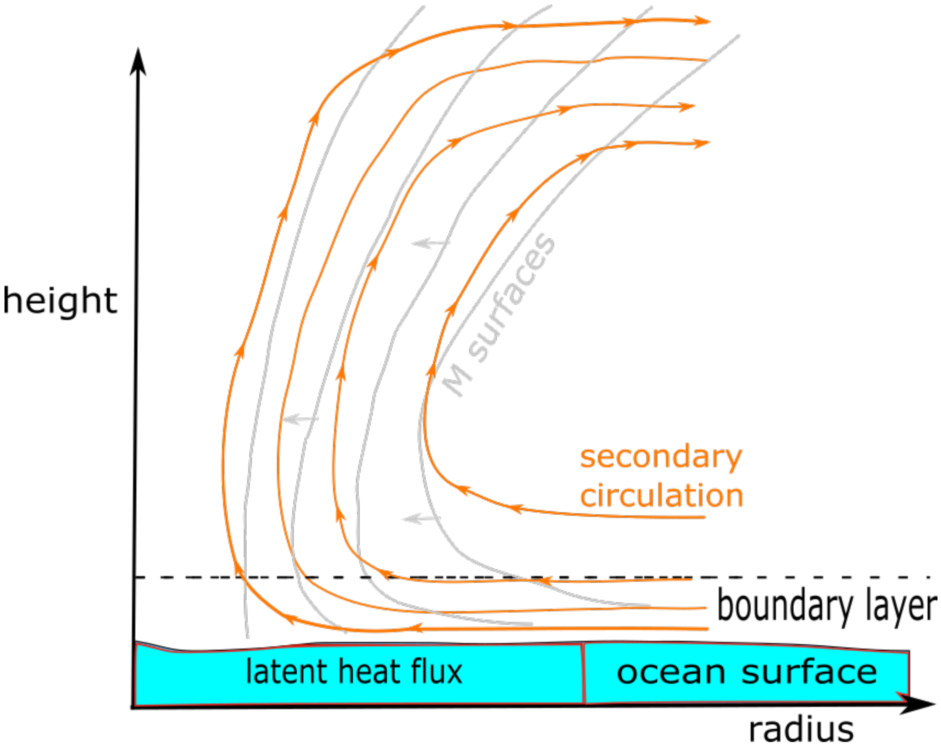

Figure 2.2: Schematic of the tropical cyclone circulation in the axisymmetric picture as a function of height and radius. In this case, the secondary circulation brings in M-surfaces radially inwards, which is referred to as spin up. The surface latent heat flux is associated with the evaporation of water, which is transported by the boundary layer.

The condensation of water vapour in the deep convective updraughts, forming the eyewall, releases latent heat, which drives the secondary circulation. This release of latent heat corresponds to diabatic heating in the eyewall updraught.

The water vapour evaporated at the sea surface does not automatically enter the eyewall updraught. The supply of water vapour to the eyewall updraught first goes through the lowermost atmospheric layer, known as the boundary layer. The boundary layer plays an important thermodynamic role for spin up by supplying the moisture, which includes the water vapour evaporated at the sea surface, to sustain deep convection in the eyewall updraught (Emanuel, 1986; Ooyama, 1969).

The effect of boundary layer moisture on deep convection in the eyewall updraught can be understood in terms of the equivalent potential temperature, θ_e[2]. The buoyancy of boundary layer air parcels depends on the value of θ_e. If θ_e is sufficiently large, air parcels are buoyant enough to rise from the top of the boundary layer into the eyewall updraught above. These air parcels influence the strength of deep convection in the eyewall updraught, which again depends on the value of θ_e. The value of θ_e in the boundary layer is influenced by the surface latent heat flux. By influencing the surface latent heat flux, sea-surface cooling affects the boundary layer θ_e and the tropical cyclone circulation.

---

[2] The physical meaning of θ_e is the temperature an air parcel would have after all the water vapour within the air parcel condenses and the air parcel is brought to a reference height, usually the sea surface.

2.2 SPIN DOWN IN COUPLED MODELS

The scientific background above allows us to follow the reasoning presented in recent studies as to how tropical cyclone intensity decreases in coupled simulations (Chen et al., 2010a, 2017; Guo et al., 2020; Li et al., 2018; Ma, 2020). These studies describe how sea-surface cooling causes surface latent heat flux to decrease, which in turn decreases θ_e in the boundary layer. They then link the decrease in boundary layer θ_e to a weakening of deep convection in the eyewall updraught. The weakening deep convection leads to a weakening of the entire secondary circulation that causes M-surfaces to move radially outwards together with the eyewall updraught. The outward moving M-surfaces correspond to a spin down of the tropical cyclone and a decrease in tropical cyclone intensity. While this reasoning is not wrong, it neglects the role of boundary layer dynamics, which are increasingly being recognised as playing an important role for tropical cyclone spin up (Montgomery et al., 2017).

2.3 BOUNDARY LAYER DYNAMICS

The importance of boundary layer dynamics to spin up arises, somewhat counter-intuitively, due to the friction at the sea surface that characterises the boundary layer flow. The friction upsets the approximate radial balance between the centrifugal, Coriolis and pressure gradient forces, known as gradient wind balance.

The lack of gradient wind balance in the boundary layer can be understood as follows. At the outer edges of the tropical cyclone at some large radius, R, air parcels have a tangential wind speed, $v(R)$, and are in gradient wind balance. Due to friction, the tangential wind speed in the boundary layer, $v_b(R)$, is less than $v(R)$. As $v_b(R)$ is less than $v(R)$, the centrifugal force that acts on the air parcel in the boundary layer is less than the centrifugal force above the boundary layer. Since the radial pressure gradient above the boundary layer is transmitted unchanged into the boundary layer and the Coriolis force remains unchanged, a net inward force in the radial direction arises.

The net inward force results in air parcels spiralling inwards with large radial speeds that exceed that of air parcels above the boundary layer. As the boundary layer air parcels move inwards, they lose M due to friction at the sea surface, unlike air parcels above the boundary layer, which conserve M to a good approximation. However, if the loss of M is sufficiently small, air parcels at some small radius, r, can obtain a $v_b(r)$ that locally exceeds $v(r)$. In this case, the centrifugal force acting on the boundary layer air parcel is locally greater than the centrifugal force acting on air parcels above the boundary layer. As a result, the sign of the net radial force changes, and there is a net radial force outwards. Correspondingly, the boundary layer air parcels decelerate. Due to mass continuity, the air parcels are then pushed upwards out of the boundary layer.

2.3.1 *Vertical mass flux*

The rate at which air mass is pushed vertically out of the boundary layer depends on strength of convergence in the boundary layer itself. The strength of this convergence

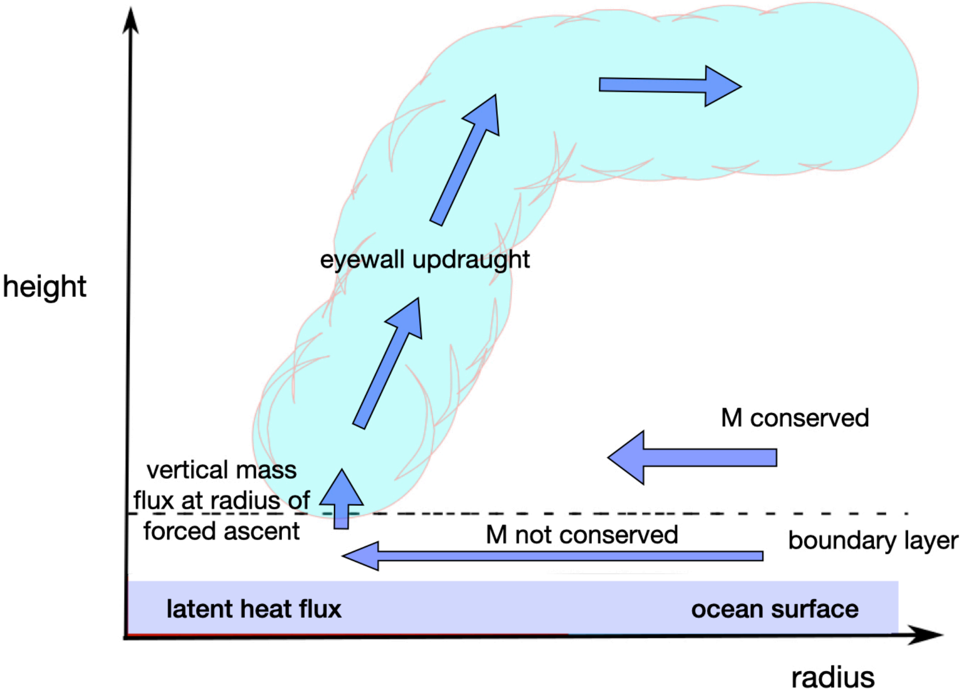

Figure 2.3: Schematic of the tropical cyclone circulation showing key aspects of the rotating-convection paradigm in the axisymmetric picture. In the boundary layer, air parcels do not conserve M as they spiral inwards. Despite this, the strong inflow there means that the tangential velocity of boundary layer air parcels can locally exceed the tangential velocity above the boundary layer. At the radius of forced ascent, the boundary layer inflow turns upwards, corresponding to a vertical mass flux. The schematic is adapted from Montgomery et al. (2014).

depends on the radial and tangential velocity of air parcels spiralling inwards, which primarily depends on boundary layer dynamics. Hence, the rate at which air mass flows out of the top of the boundary layer is principally determined by boundary layer dynamics. By contrast, the rate at which air mass rises in the eyewall updraught depends on the buoyancy of the air parcels, which in turn depends on the θ_e in the boundary layer. The difference between these two vertical mass fluxes influences the ability of the tropical cyclone to draw in M-surfaces. For the tropical cyclone to draw in M-surfaces, the vertical mass flux in the eyewall must exceed the vertical mass flux at the top of the boundary layer. Otherwise, the boundary layer air mass flows outwards above the boundary layer and the M-surfaces move radially outwards, corresponding to spin down (Smith et al., 2018). In this sense, spin up depends on the interplay between boundary layer dynamics and thermodynamics.

2.3.2 *Radius of forced ascent*

The importance of boundary layer dynamics for spin up not only rests on the vertical mass flux at the top of the boundary layer, but also on the radius at which the boundary layer flow turns upwards, known as the radius of forced ascent. Similar to the vertical mass flux at the top of the boundary layer, the radius of forced ascent depends on the boundary layer convergence, which is primarily governed by boundary layer dynamics. As a result, boundary layer dynamics exert a strong control on the radius of forced ascent (Abarca et al., 2015; Nguyen et al., 2002; Persing et al., 2013; Schmidt et al., 2016; Smith et al., 2009; Zhang et al., 2001; Zhang et al., 2015a). By controlling changes in the radius of forced ascent, boundary layer dynamics influence the θ_e of air parcels rising into the eyewall updraught and, in turn, the strength of deep convection there (Smith et al., 2016). The strength of deep convection affects the vertical mass flux in the eyewall updraught, which in turn influences the strength of the secondary circulation and the ability of the tropical cyclone to spin up. Again, spin up depends on the interplay between boundary layer dynamics and thermodynamics.

The radius of forced ascent also influences the vertical advection of M into the eyewall updraught. As mentioned, v_b can be locally larger than v, which is equivalent to the M in the boundary layer locally exceeding M above the boundary layer. The process by which air parcels in the boundary layer possess M that is locally larger than M above the boundary layer is referred to as the boundary layer spin-up mechanism (Smith et al., 2009). Due to the boundary layer spin-up mechanism, vertical advection of angular momentum can significantly contribute to spin up in the eyewall updraught, provided sufficiently large angular momentum is generated in the boundary layer (Kilroy et al., 2016; Persing et al., 2013; Schmidt et al., 2016; Smith et al., 2009).

2.3.3 *Rotating-convection paradigm*

A paradigm for tropical cyclone spin up that explicitly recognises the importance of boundary layer dynamics is the rotating-convection paradigm (Montgomery et al., 2017). This paradigm is an extension of the cooperative paradigm of Ooyama (1982; 1969) that includes the boundary layer spin-up mechanism as articulated by Smith et al. (2009). In the rotating-convection paradigm, boundary layer dynamics play an important role for spin up by exerting strong control on the convergence of air mass in the boundary layer. The boundary layer convergence determines to a large extent the vertical mass flux at the top of the boundary layer and the radius of forced ascent. Together with the value of θ_e in the boundary layer, the vertical mass flux and the radius of forced ascent influence the strength of the secondary circulation and the ability of the tropical cyclone to spin up.

The rotating-convection paradigm highlights the tightly coupled behaviour between the deep convection in the eyewall updraught and the convergence in the boundary layer. The coupling is two way, so that not only does any change in the boundary layer convergence affect the eyewall updraught, but a change in the eywall updraught also affects the boundary layer convergence. This is because the eyewall updraught impacts the advection of angular momentum surfaces above the boundary layer, which leads to a local change in the tangential velocity above the boundary layer. The radial pressure gradient at the top of the boundary layer adjusts to the local change in tangential velocity, such that the flow remains in gradient wind balance. This radial pressure gradient is then transmitted into the boundary layer, where it affects the dynamics of the air parcels and, as a result, boundary layer convergence, vertical mass flux at the top of the boundary layer and the radius of forced ascent.

2.3.4 *Non-linear boundary layer dynamics and the slab boundary layer model*

The rotating-convection paradigm recognises the non-linear nature of boundary layer dynamics. The non-linear nature arises from the lack of gradient wind balance in the boundary layer, which leads to large radial wind speeds. As a result, the non-linear advective terms in the momentum equations become large in the boundary layer. Consequently, these non-linear terms cannot be neglected from the momentum equations (Vogl et al., 2009).

A simple model for the boundary layer that retains the non-linear terms in the momentum equations is the steady-state slab boundary layer model. As its name suggests, the steady-state slab boundary layer model treats the boundary layer as a slab of constant height, h, with a boundary layer flow that is not dependent on height or time but a function of radius only. A steady-state model is appropriate here, because the boundary layer is thin and reacts to changes in the radial pressure gradient at the top of the boundary layer on short time scales (Kilroy et al., 2016). Since the slab boundary layer model is based on the momentum and continuity equations, the solutions represent dynamical considerations only.

Solving the equations for the slab boundary layer model yields solutions for the radial velocity, $u_b(r)$, the tangential velocity, $v_b(r)$ and the vertical velocity, $w_b(r)$. The boundary conditions applied to the slab boundary layer model are the radial pressure gradient at the top of the boundary layer at h, which is transmitted into the boundary layer, and the frictional drag at the sea surface. The frictional drag depends on a drag coefficient, C_D, which is a function of wind speed and has to be prescribed. The radial pressure gradient at h is derived from the tangential velocity at the top of the boundary layer, $v(r)$, which is assumed to be in gradient wind balance.

The governing non-linear equations of the slab boundary layer model are parabolic. Information in parabolic equations flows in the direction of the physical flow. Since the physical flow is inwards in the slab boundary layer model, the solution at a given radius depends only on the flow at larger radii and does not know about the flow at smaller radii.

Kilroy et al. (2016) use the steady-state slab boundary layer model to demonstrate the importance of non-linear boundary layer dynamics for the spin down of a tropical cyclone. They compare the boundary layer flow of a tropical cyclone simulated in an atmosphere-only model with solutions from a slab boundary layer model. They find that the slab boundary layer model predicts the increasing radius of forced ascent of the decaying tropical cyclone. Since the solutions only depend on the flow at larger radii, they conclude that the increasing radius of forced ascent is controlled by the strengthening primary circulation at the outer edges of the tropical cyclone. This strengthening primary circulation

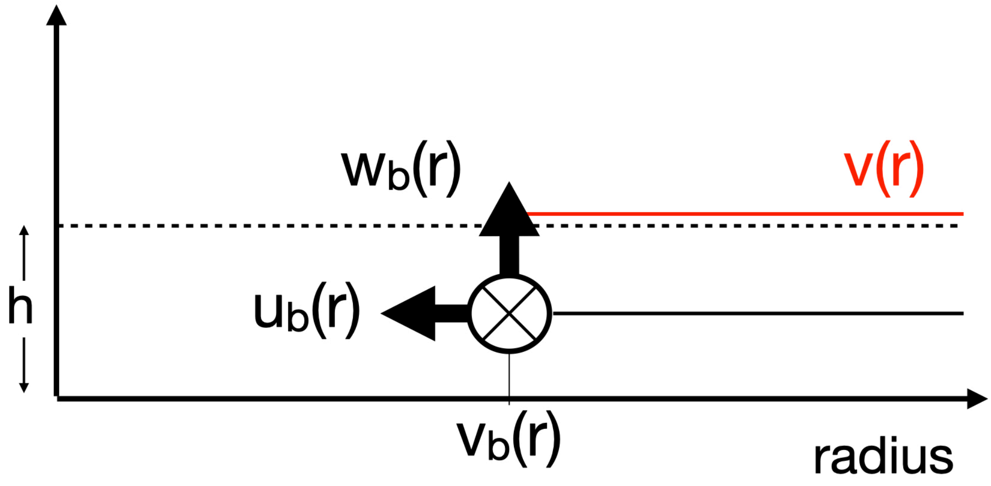

Figure 2.4: Schematic of slab boundary layer model adapted from Montgomery et al. (2017). The slab extends vertically from the sea surface up to a height, h. The arrows show the orientation of the radial velocity, $u_b(r)$, and the vertical velocity out of the boundary layer, $w_b(r)$. The circle with the cross indicates the orientation of the tangential velocity, $v_b(r)$, into the page. The solutions, $u_b(r)$, $v_b(r)$ and $w_b(r)$ are a function of radius only. The red line indicates that the solution at a given radius only depends on the boundary layer flow and the tangential velocity at the top of the boundary layer, v(r), at larger radii.

corresponds to the increasing size of the tropical cyclone and is henceforth referred to as the expanding outer circulation. The control exerted by the expanding outer circulation is a consequence of the non-linear nature of boundary layer dynamics that is captured in the slab boundary layer model.

Kilroy et al. (2016) use these results to articulate the role of non-linear boundary layer dynamics for spin down. Their articulation is framed in terms of the rotating-convective paradigm and can be summarised as follows. The increase in the radius of forced ascent is controlled by the expanding outer circulation on account of non-linear boundary layer dynamics. The increase in the radius of forced ascent contributes to the outward movement of the eyewall updraught and the accompanying outward movement of M-surfaces in the vicinity of the eyewall updraught. At the same time, the expanding outer circulation corresponds to M-surfaces at large radii being drawn inwards. The radial movement of the M-surfaces corresponds to a local change in the tangential velocity at the top of the boundary layer and the radial pressure gradient transmitted into the boundary layer. The resulting change in the radial pressure gradient together with the continuing expansion of the outer circulation determine the extent to which the radius of forced ascent increases and so on.

2.4 RESEARCH QUESTION

The study by Kilroy et al. (2016) shows that boundary layer dynamics play an important role for tropical cyclone spin down. As with the other numerical studies on boundary layer dynamics, the tropical cyclone in their study is simulated in an atmosphere-only model, where there is no sea-surface cooling and the SST is fixed. This raises the question as to the role of non-linear boundary layer dynamics for the spin down simulated in coupled models that capture sea-surface cooling.

However, there are no studies that investigate the role of the boundary layer dynamics for tropical cyclone spin down in coupled models that build on the work of Kilroy et al. (2016). Moreover, no study has investigated the importance of boundary layer dynamics for the surface latent heat flux in coupled simulations. Boundary layer dynamics presumably play an important role for surface latent heat flux by determining the near-surface wind speed, on which surface latent heat flux depends.

More generally, there has been no attempt to understand the behaviour of tropical cyclone intensity in coupled models with reference to the aforementioned aspects of boundary layer dynamics that are central to the rotating-convection paradigm. As a result, it is not clear how boundary layer dynamics may be important for the strength of the negative feedback and the weakening of this feedback by warm-core eddies. This is the research gap that I aim to tackle, which is summarised by the following research question:

Are boundary layer dynamics important for the negative feedback and the tropical cyclone intensity response to a warm-core eddy in coupled atmosphere-ocean models?

2.5 STRATEGY TO ANSWER THE RESEARCH QUESTION

To answer this research question, I analyse a coupled atmosphere-ocean simulation of a single tropical cyclone that encounters a warm-core eddy. The details of the simulation are given in Section 2.6. In Section 2.7, I describe how the intensity of the simulated tropical cyclone changes over its life cycle. Then, in Section 2.8 I examine the role of the coupling between the atmosphere and the ocean, which I refer to as air-sea coupling in this Chapter. Subsequently, in Section 2.9 I turn my attention to the changes in the primary and secondary circulation that accompany the changes in intensity. To understand the role of boundary layer dynamics for these changes in the primary and secondary circulation, I conduct a process-based analysis guided by a conceptual framework that extends the rotating-convection paradigm to account for air-sea coupling. I outline the conceptual framework in Section 2.10 and present the results of the process-based analysis in Section 2.11. In Section 2.12, I complement the process-based analysis with solutions from the same steady-state slab boundary layer model used in Kilroy et al. (2016). Finally in Section 2.13, I summarise my results, present my conclusions with respect to the research question and discuss the broader implications for intensity forecasting.

2.6 SIMULATION

The simulation is run with the global, convection-permitting, coupled atmosphere-ocean ICON model with a horizontal grid spacing of 5 km in both the atmosphere and the ocean (Korn, 2017; Zängl et al., 2014). The ocean component is spun up with atmospheric forcing prior to the coupling (Dee et al., 2011), which permits the formation of a realistic ocean-eddy field that includes background oceanic features, such as the warm-core eddy encountered by the tropical cyclone. Following initialisation of the ocean and atmosphere, the model is run in coupled mode for 40 days. The tropical cyclone is not seeded in the model, but forms organically over the North Atlantic on day 30 of the coupled simulation.

2.7 CHANGE IN TROPICAL CYCLONE INTENSITY

The life cycle of the simulated tropical cyclone can be divided into four phases: tropical depression, rapid intensification, the mature phase and landfall. The tropical cyclone intensity initially increases slowly during the tropical depression phase, before increasing rapidly into a category 3 tropical cyclone in the subsequent rapid intensification phase. After reaching peak intensity at the end of the rapid intensification phase, the tropical cyclone enters the mature phase, which I focus on in the subsequent analysis. The mature phase is then divided into three subphases: cold wake 1 (CW1), cold wake 2 (CW2) and warm feature (WF). During CW1 and CW2, the intensity continuously decreases; gradually during CW1 and then more rapidly during CW2. Subsequently, the tropical cyclone undergoes a period of re-intensification during WF. After the mature phase, the tropical cyclone makes landfall on the east coast of the United States before recurving back over the North Atlantic.

2.8 ROLE OF AIR-SEA COUPLING

Air-sea coupling plays an important role for the changes in tropical cyclone intensity during the mature phase. The wind-stress force exerted by the tropical cyclone induces sea-surface cooling. The corresponding change in SST under the tropical cyclone leads to changes in the surface latent heat flux supplied to the tropical cyclone. These changes in surface latent heat flux then influence the changes in intensity.

During CW1, the SST under the tropical cyclone decreases due to the formation of a cold wake trailing the tropical cyclone. The decrease in SST coincides and is strongly correlated with a decrease in the surface latent flux. The decrease in surface latent heat flux is then accompanied by the gradual decrease in intensity.

During CW2, the sea-surface cooling in the cold wake increases in strength, which is possibly due to the decrease in translational speed and an increase in the size of the tropical cyclone between CW1 and CW2. As a result, the SST under the tropical cyclone decreases further. Similar to CW1, the decrease in SST is accompanied by and strongly correlated with a further decrease in surface latent heat flux. The further decrease in surface latent heat flux occurs as the intensity decreases more rapidly compared to CW1.

During WF, the sea-surface cooling in the cold wake weakens due to the presence of the warm-core eddy. Interestingly, the warm-core eddy is not visible in the SST field before it is encountered by the tropical cyclone. Instead, the warm-core eddy can be seen from the ocean heat content, which is a measure of the anomalous heat content in the upper ocean where the temperature exceeds 26 °C, and a rotating surface current. As the tropical cyclone translates over the warm-core eddy, the warm-core eddy suppresses the sea-surface cooling and disrupts the cold wake. As a result, the tropical cyclone experiences an increase in SST. The increase in SST coincides and is strongly correlated with an increase in surface latent heat flux, which is accompanied by the period of re-intensification.

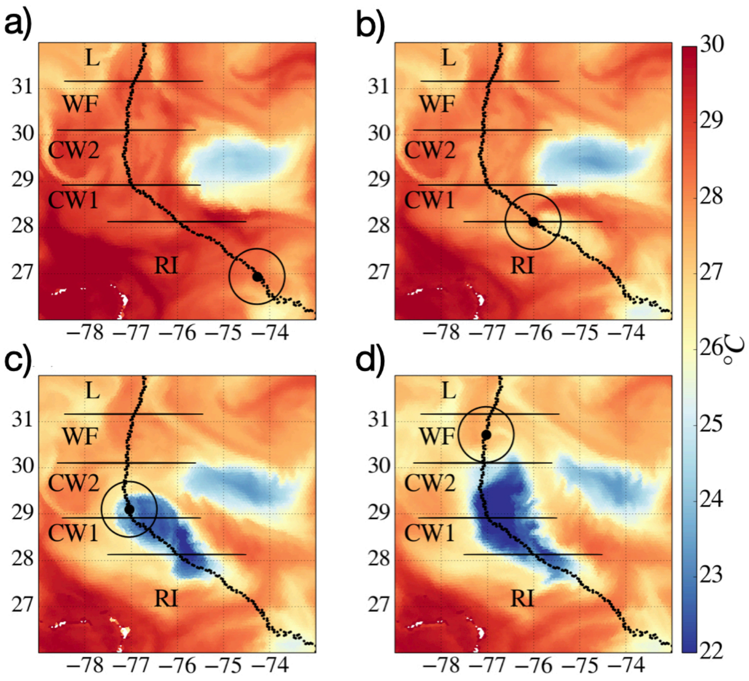

Figure 2.5: Snapshots of SST in (a) the rapid intensification phase (RI), (b) CW1, (c) CW2 and (d) WF. The tropical cyclone is shown by the black circle and traverses northwards along the track indicated by the dotted line in all the snapshots. The partitions between the subphases are indicated with solid horizontal lines. The cold wake is evident from the region of low SST trailing the tropical cyclone. Note how the cold wake is disrupted in panel (d) and no longer within the circle directly under the tropical cyclone.

Although SST and surface latent heat flux are strongly correlated, it is not possible to attribute the change in surface latent heat flux solely to the change in SST. This is because the surface latent heat flux is a function of both SST and near-surface wind speed. As a result, changes in the near-wind speed directly contribute to the changes in the surface latent heat flux. Moreover, changes in the near-surface wind speed correspond to changes in the wind stress at the sea surface, which in turn alter the strength of sea-surface cooling, the SST under the tropical cyclone and the surface latent heat flux. Nevertheless, analysing the radial distribution of SST, near-surface moisture disequilibrium, near-surface wind speed and surface latent heat flux reveals that the change in surface latent heat flux is primarily driven by changes in SST and not near-surface wind speed during the mature phase.

As the change in the surface latent heat flux is primarily driven by changes in the SST, the simulation underscores the importance of air-sea coupling and the role of the warm-core eddy for the re-intensification. Since the warm-core eddy was not visible in the pre-storm SST field, the simulation emphasises the importance of initialising ocean models with a realistic ocean eddy field for intensity forecasting.

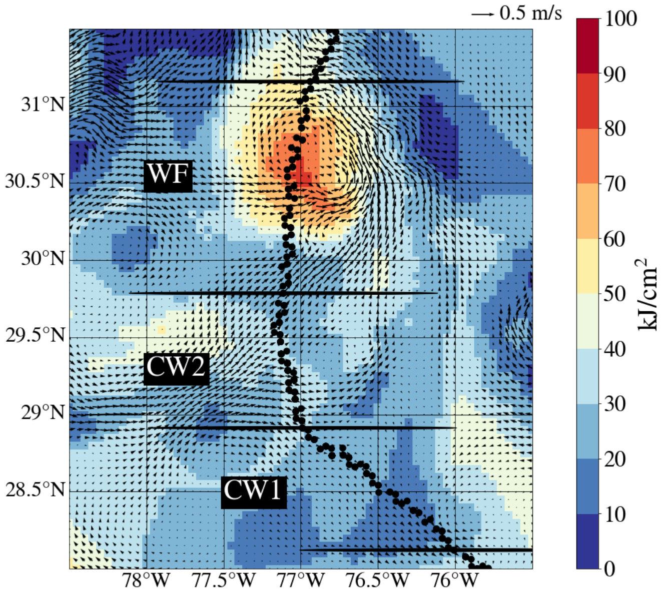

Figure 2.6: Ocean heat content prior to the arrival of the tropical cyclone. The horizontal surface current is shown in by the black arrows. The tropical cyclone traverses northwards along the track indicated by the dotted line. The partitions between the subphases are indicated with solid horizontal lines. The warm-core eddy is identifiable as the region of high ocean heat content WF section of the track that is centred on 30.5 °N 77 ° W. Note the rotational surface current that is characteristic of warm-core eddies.

2.9 CHANGE IN PRIMARY AND SECONDARY CIRCULATION

The changes in intensity during the mature phase are accompanied by changes to the tropical cyclone circulation. During CW1 and CW2, the secondary circulation along with the eyewall updraught weakens. As the eyewall updraught weakens, it moves radially outwards. The primary circulation also weakens in the vicinity of the eyewall updraught, where M-surfaces move outwards. Simultaneously, the primary circulation strengthens at larger radii, corresponding to an inward movement of the M-surfaces and an expanding outer circulation. During WF, the secondary circulation strengthens along with eyewall updraught. As the eyewall updraught strengthens, it moves radially inwards. At the same time, the primary circulation strengthens throughout the tropical cyclone and M-surfaces both in the vicinity of the eyewall updraught and at larger radii move inwards. The inward movement of M-surfaces during WF corresponds to a continued expansion of the outer circulation.

2.10 CONCEPTUAL FRAMEWORK

To understand the importance of boundary layer dynamics for the changes in the tropical cyclone circulation and intensity, I conduct a process based analysis guided by a conceptual framework that recognises the role of boundary layer dynamics. The conceptual framework is an extension of the rotating-convection paradigm that includes the effect of air-sea coupling. Within this framework, I explicitly recognise the role of non-linear boundary layer dynamics in controlling the change in the radius of forced ascent at the top of the boundary layer on account of the expanding outer circulation (Kilroy et al., 2016). This framework has not previously been used to investigate the change in simulated tropical cyclone intensity for coupled atmosphere-ocean models and can be understood as follows:

(1) Air-sea coupling: Surface latent heat supplied to the tropical cyclone depends on the SST, the near-surface wind speed and the near-surface moisture content. Changes in the surface latent heat flux lead to changes in the equivalent potential temperature, θ_e, in the boundary layer. The value of θ_e determines the buoyancy acquired by the air parcels in the boundary layer and whether they reach the level of free convection. Air parcels that do not reach the level of free convection remain negatively buoyant. Those that reach the level of free convection become positively buoyant and rise into the troposphere with a vertical velocity that depends on θ_e.

(2) Boundary layer convergence via surface drag: Surface drag leads to an inflow in the boundary layer. Due to the upward pressure-perturbation force that follows from mass continuity, the converging air is accelerated out of the boundary layer. The resulting vertical mass flux at the top of the boundary layer, $\overline{\rho w}_{BL}$, depends, in part, on the strength of the convergence in the boundary layer. The strength of convergence and the radial location at which the air is directed upwards is determined to a large extent by the non-linear dynamics of the boundary layer flow and the expanding outer circulation.

(3) Boundary layer convergence via eyewall suction: In addition to the convergence pushing out air mass from the boundary layer, deep convection in the eyewall updraught acts to suck air mass at the top of the boundary layer into the eyewall updraught above (Smith et al., 2015). Consequently, $\overline{\rho w}_{BL}$ depends on boundary layer convergence via both surface drag and eyewall suction, effects which cannot be separated because of the nonlinearity of the flow dynamics.

(4) Vertical mass flux: In contrast to $\overline{\rho w}_{BL}$, the vertical mass flux in the eyewall updraught, $\overline{\rho w}_{EW}$, is primarily buoyancy-driven and, therefore, more sensitive to changes in θ_e and, ultimately, air-sea coupling than to changes in $\overline{\rho w}_{BL}$. The change in $\overline{\rho w}_{EW}$ depends also on how the areal extent of the eyewall updraught changes. The vertical mass fluxes are important because they influence the evolution of the tropical cyclone structure. Due to mass continuity, mass flows out above the boundary layer if $\overline{\rho w}_{EW}$ is smaller than $\overline{\rho w}_{BL}$. Conversely, if $\overline{\rho w}_{EW}$ is greater than $\overline{\rho w}_{BL}$, there is inflow above the boundary layer.

(5) Advection of absolute angular momentum: Any change of the inflow or outflow above the boundary layer is reflected in the radial advection of absolute angular momentum, M. A weakening inflow above the boundary layer decreases the ability of the tropical cyclone to advect M-surfaces radially inwards. Conversely, a strengthening inflow enhances the ability of the tropical cyclone to advect M-surfaces radially inwards.

(6) Tangential velocity change: The radial advection of M-surfaces translates into local changes in the tangential velocity, v.

(7) Feedback on air-sea coupling: Finally, the local change in the tangential velocity above the boundary layer leads to a change in the radial pressure gradient at the top of the boundary layer (assuming the flow is in approximate gradient-wind balance). This radial pressure gradient is transmitted into the boundary layer and leads to a change in the net radial force there. Through non-linear boundary layer dynamics, the change in the net radial force and the expanding outer circulation determine the change in the boundary layer convergence and the radius of forced ascent. Since the accompanying change in the near-surface wind field influences the radial distribution of surface latent heat flux and, therefore, the air-sea coupling outlined in (1), the interaction between the boundary layer flow and surface latent heat flux forms a feedback loop.

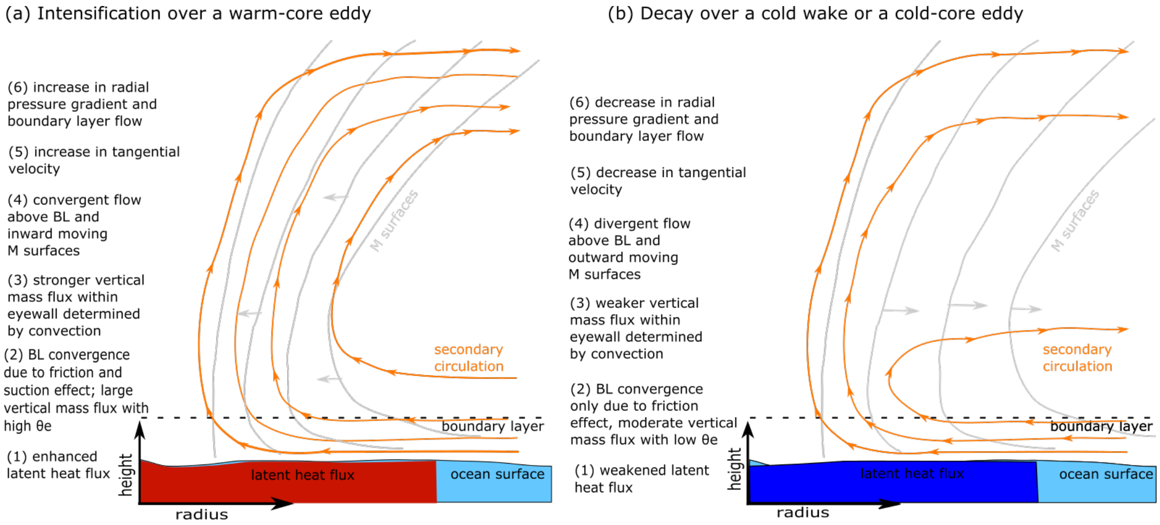
(a) Intensification over a warm-core eddy
(6) increase in radial pressure gradient and boundary layer flow
(5) increase in tangential velocity
(4) convergent flow above BL and inward moving M surfaces
(3) stronger vertical mass flux within eyewall determined by convection
(2) BL convergence due to friction and suction effect; large vertical mass flux with high θe
(1) enhanced latent heat flux
M surfaces
secondary circulation
boundary layer
latent heat flux
ocean surface
height
radius
(b) Decay over a cold wake or a cold-core eddy
(6) decrease in radial pressure gradient and boundary layer flow
(5) decrease in tangential velocity
(4) divergent flow above BL and outward moving M surfaces
(3) weaker vertical mass flux within eyewall determined by convection
(2) BL convergence only due to friction effect, moderate vertical mass flux with low θe
(1) weakened latent heat flux
M surfaces
secondary circulation
boundary layer
latent heat flux
ocean surface
height
radius

Figure 2.7: Schematic of the processes outlined in the conceptual framework in the case of (a) intensification over a warm-core eddy and (b) decay over a cold wake.

Within this framework, the intensification of a mature tropical cyclone over a warm-core eddy can be understood as follows (please refer to Figure 2.7). A higher surface latent heat flux leads to an increase in θ_e at the top of the boundary layer via air-sea coupling. Air parcels with higher θ_e then ascend from the boundary layer into the eyewall updraught at the radius of forced ascent. The vertical mass flux at the top of the boundary layer depends on the convergence due to surface friction and the suction effect of deep convection in the eyewall updraught. Assuming there is no warming aloft, the increase in mean θ_e of air parcels ascending into the eyewall leads to an increase in mean vertical velocity in the eyewall updraught and, if the areal extent of the eyewall updraught does not decrease appreciably, an increase in the vertical mass flux. The inflow and the inward advection of M increase in a vertical layer above the boundary layer at radii outside the eyewall updraught. The corresponding increase in the local tangential velocity increases the radial pressure gradient transmitted into the boundary layer, which changes the net radial force there. The change in the net radial force, along with the expanding outer circulation, leads to a change in the boundary-layer convergence and the radius of forced ascent. While one may expect an increase in the transmitted radial pressure gradient to increase the strength of the boundary-layer convergence and decrease the radius of forced ascent, one cannot know whether this is the case until one performs the calculation, due to the nonlinear nature of boundary-layer dynamics. A strengthening in the boundary-layer convergence would feedback on air-sea coupling, with increasing near-surface wind speed increasing the surface latent heat flux, assuming a constant moisture disequilibrium at the air-sea interface. In reality, moisture disequilibrium is not constant and increases in moisture disequilibrium can be a more efficient way of increasing surface latent heat flux than near-surface wind speed (Jaimes et al., 2021).

As shown in Figure 2.7, the decay of a mature tropical cyclone due to a cold wake or interaction with a cold-core eddy can be understood with the same set of processes, but with the tendencies reversed. Again, although one might expect a weakening of boundary-layer convergence and an increase in the radius of forced ascent, one cannot be sure, due to the nonlinear nature of boundary-layer dynamics. In the case of weakening boundary-layer convergence, a negative feedback may occur between the surface latent heat flux and the near-surface wind speed. Note, however, that a negative feedback might also arise for fixed SST, if convergence in the boundary layer is initially strong and $\overline{\rho w}_{BL}$ is greater than $\overline{\rho w}_{EW}$. In this case, there is an outflow above the boundary layer that spins down the boundary-layer flow (Kilroy et al., 2016; Smith et al., 2018).

2.11 PROCESS-BASED ANALYSIS

The process-based analysis is guided by the conceptual framework outlined in the previous section. The analysis is conducted separately for the slow decay, fast decay and re-intensification the tropical cyclone experiences during CW1, CW2 and WF, respectively. By contrasting the evolution of the tropical cyclone circulation for these three periods, I illustrate the combined role of boundary layer dynamics and air-sea coupling for the intensity response. While I describe the processes for each period following the order set out in Section 2.10, it is important to remember that the processes occur in parallel and not one after the other.

For the process-based analysis, I examine fields averaged around the centre of the tropical cyclone, such that they are a function of height and radius only. Analysing these azimuthal-mean fields is appropriate because the tropical cyclone is highly axisymmetric in the mature phase. For the following analysis, it is also necessary to define the boundary layer height, h. Here, I follow the dynamical definition of h as the height at which the maximum tangential velocity in the tropical cyclone is located (Bryan et al., 2009). With this definition, h fluctuates between 600 and 800 m in the mature phase. The vertical level in the ICON model that most closely corresponds to the largest value of h in the mature phase is located at 780 m. While the boundary layer height is in reality a function of radius

(Zhang et al., 2011), I take h to be a constant 780 m with a view to keep the subsequent analysis simple.

2.11.1 *Slow decay*

During CW1, the decrease in SST and the accompanying decrease in the moisture disequilibrium at the air–sea interface, Δq, dominate the decrease in the surface latent heat flux. The decrease in surface latent heat flux is accompanied by a transient decrease in the azimuthal-mean equivalent potential temperature at the top of the boundary layer, $\overline{\theta_e}$. However, the transient decrease in $\overline{\theta_e}$ does not have a large influence on the mean $\overline{\theta_e}$ of air layer ascending into the eyewall updraught at the top of the boundary layer, $\langle\overline{\theta_e}\rangle_{up}$, which is characterised by vertical velocities exceeding 0.25 ms^{-1}. This is because the corresponding updraught region at the top of the boundary layer extends from 15–40 km radius, whereas $\overline{\theta_e}$ changes inside a 20 km radius. Hence, $\langle\overline{\theta_e}\rangle_{up}$ is not appreciably affected by the decrease in the surface latent heat flux. During the same time, the mean radius of the eyewall updraught increases on account of nonlinear boundary-layer dynamics in the presence of the expanding outer circulation. As the mean radius of the updraught increases, $\langle\overline{\theta_e}\rangle_{up}$ decreases. The decreasing $\langle\overline{\theta_e}\rangle_{up}$ reduces the local buoyancy of air parcels in the eyewall updraught, which leads to a decrease in the vertical velocity in the eyewall updraught. While the vertical velocity decreases at a height of 5 km, which is in the middle troposphere, the average vertical mass flux remains steady [3] within a radius of 60 km, which includes the outward-moving eyewall updraught. Since the difference between the vertical mass flux of the eyewall updraught in the middle troposphere and at the base of the eyewall updraught remains large, the eyewall updraught is more than able to accept the ascending boundary-layer air and produce a strong radial inflow in a vertical layer above the boundary layer at radii larger than the radii where the eyewall updraught is located. In turn, the radial inflow draws absolute angular momentum (M) surfaces at these radii beyond the eyewall updraught, leading to a local increase in the tangential wind speed. Because the tangential wind speed above the boundary layer remains in gradient-wind balance to a good approximation, the local increase in the tangential wind speed increases the local radial pressure gradient, which is transmitted essentially unchanged into the boundary layer. The increase in the radial pressure gradient in the boundary layer changes the net radial force in the boundary layer at radii beyond the eyewall updraught. As shown by Kilroy et al. (2016), the expanding outer circulation leads to an increase in the mean radius of the air ascending into the eyewall updraught through nonlinear boundary-layer dynamics.

2.11.2 *Fast decay*

The evolution during CW2 is similar to CW1 apart from several key differences. The wind-stress-induced sea-surface cooling is stronger than in CW1, which leads to a further decrease in surface latent heat flux. In contrast to CW1, $\overline{\theta_e}$ decreases over the radial interval

---

[3] Since the areal extent of the eyewall updraught increases, decreasing vertical velocity does not necessarily equate to a decreasing vertical mass flux.

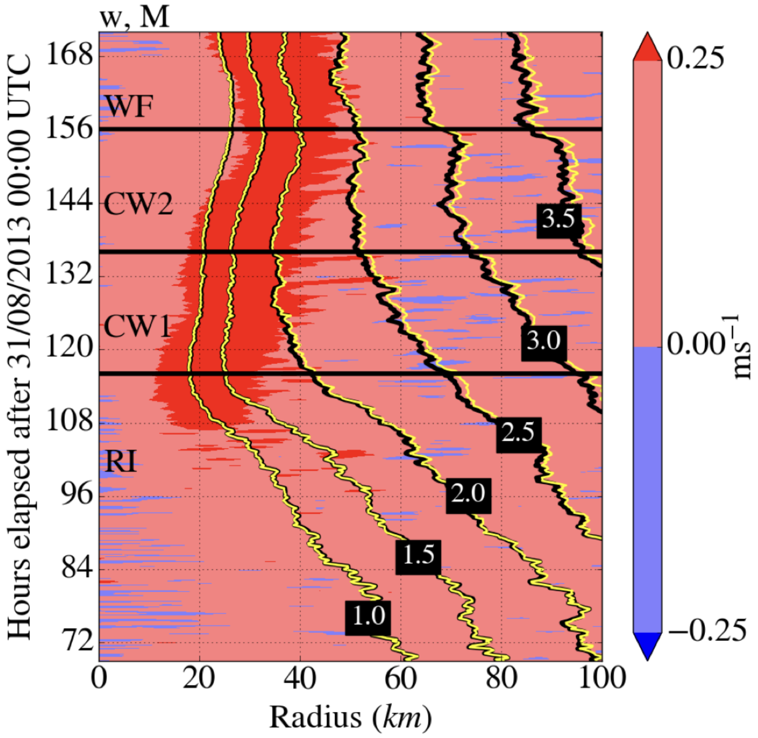

Figure 2.8: Hovmöller plot of absolute angular momentum, M, and vertical velocity, w. The M contours at the top of the boundary layer at a height of 780 m is shown as a black contour. The M contours at a height of 620 m are shown as a yellow contour. The contours are displayed for (1.0, 1.5, 2.0, 2.5, 3.0, 3.5) × 10^6 m^{2}s^{-1}. The shading indicates w at 780 m according to the colorbar. Note how the radial interval where w exceeds 0.25 ms^{-1}, taken to be the region where air ascends into the eyewall updraught, move radially outwards during CW1 and CW2 and inwards during WF. The M contours within this radial interval also move radially outwards during CW1 and CW2 and inwards during WF.

spanned by the eyewall updraught and contributes substantially to the decrease of the $\overline{\theta_e}$ of air ascending into the eyewall updraught. The combined effect of the increasing radius of forced ascent and decreasing θ_e at the top of the boundary layer result in $\langle\overline{\theta_e}\rangle_{up}$ decreasing faster during CW2 than during CW1. Consequently, the eyewall updraught weakens more substantially during CW2 than CW1. Unlike in CW1, the eyewall updraught weakens to the extent that the vertical mass flux also decreases during CW2. The weaker vertical mass flux leads to a weaker radial inflow above the boundary layer. The weaker radial inflow, combined with the vertical advection of low M from within the boundary layer, leads to M-surfaces moving radially outwards above the boundary layer at radii beyond the eyewall updraught up to 100-km radius. The outward movement of M-surfaces beyond the eyewall updraught stands in contrast to the inward movement of M-surfaces during CW1. As a result of the outward-moving M-surfaces, the local tangential wind speed decreases at the top of the boundary layer along with the radial pressure gradient transmitted into the boundary layer. Through nonlinear boundary-layer dynamics, the changes in the net radial force, together with the expanding outer circulation, lead to an accelerated increase in the mean radius of air ascending into the eyewall updraught compared with CW1.

2.11.3 *Re-intensification*

During the latter stage of CW2 and during WF, the tendencies in CW1 and CW2 are reversed. The subsurface warm-core eddy suppresses the sea-surface cooling and the SST under the translating tropical cyclone increases along with the surface latent heat flux. The value of $\langle\overline{\theta_e}\rangle$ increases on account of a local increase in $\overline{\theta_e}$ and the decreasing mean radius of the updraught, leading to an increase in the local buoyancy and the vertical velocity in the eyewall updraught. The increase in vertical velocity is accompanied by a sharp increase in the vertical mass flux in the eyewall updraught. Consequently, the eyewall updraught is more able to accept ascending boundary-layer air than during the decay in CW2. As a result, the radial inflow strengthens above the boundary layer and M-surfaces are drawn inwards at radii beyond the eyewall updraught. Correspondingly, the tangential wind speed at the top of the boundary layer increases along with the radial pressure gradient transmitted into the boundary layer at radii beyond the eyewall updraught. Again, through nonlinear boundary-layer dynamics, the strengthening outer circulation leads to a decrease in the mean radius of air ascending into the eyewall updraught, although a part of this decrease may be associated with local suction effects of the increasing vertical mass flux, which are not captured by boundary-layer dynamics.

2.11.4 *Discussion*

The outward-moving eyewall updraught in CW1 resembles the simulation in Kilroy et al. (2016) with constant SST, because the decrease in average surface latent heat flux does not have an appreciable effect on the thermodynamics of air ascending from the boundary layer into the eyewall updraught, captured by $\langle\overline{\theta_e}\rangle_{up}$. In CW2, by contrast, the decrease in $\langle\overline{\theta_e}\rangle_{up}$ cannot be explained without air–sea coupling. Air–sea coupling is also crucial during the latter stage of CW2 and in WF, where the increase in the average surface latent heat flux is accompanied by an increase in $\langle\overline{\theta_e}\rangle_{up}$ and a strengthening of the deep convection in the eyewall updraught.

The foregoing discussion shows that the air-sea coupling alone, corresponding to the changes in SST and surface latent heat flux, does not fully explain the changes in the tropical cyclone intensity. Instead, it is necessary to consider both air–sea coupling and boundary-layer dynamics in order to acquire a complete picture of the changes in the azimuthal-mean circulation and the intensity of the simulated tropical cyclone.

2.12 COMPLEMENTARY SOLUTIONS FROM THE STEADY-STATE SLAB BOUNDARY LAYER MODEL

In the previous section, I articulated how the expanding outer circulation influences the decay and re-intensification of the simulated tropical cyclone. Specifically, I stated that the expanding outer circulation controls the changes in the mean updraught radius via non-linear boundary layer dynamics. However, I did not provide explicit evidence for this effect. To this end, I now compare solutions from the same steady-state slab boundary layer model used by Kilroy et al. (2016) with the boundary layer flow in the ICON simulation. By indicating the change in the radius of forced ascent in the presence of an expanding circulation, the comparison with the slab boundary layer provides an insight as to whether the expanding circulation is controlling the change in the radius of forced ascent in the ICON simulation.

2.12.1 *Obtaining the solutions*

For the steady-state slab boundary layer model, I prescribe a constant boundary layer height of 780 m, matching the boundary layer height diagnosed for the tropical cyclone in the ICON simulation. I also prescribe a surface drag coefficient, C_D, which is a function of wind-speed that is compatible with observations (Black et al., 2007). The parameters in the function are tuned to fit as closely as possible to the C_D in the ICON model, which is not only a function of wind speed but also other variables. The radial pressure gradient transmitted into the boundary layer is derived from the tangential velocity at the top of the boundary layer which is taken from the ICON simulation. Solutions are then obtained separately for each time step.

After obtaining the solutions, I average the tangential and radial velocity in the ICON simulation over the lowermost 780 m corresponding to the boundary layer. This allows me to compare the solutions for the tangential and radial velocity from the slab boundary layer model to the vertically-averaged tangential and radial velocity in the ICON simulation.

2.12.2 *Comparison with the ICON simulation*

The solutions from the slab boundary layer model show good agreement with the ICON simulation. Contours of constant tangential velocity move radially outwards over time during CW1 and CW2. This outward movement of tangential velocity contours is also seen in the tangential velocity solution from the slab boundary layer model. For WF, the slab boundary layer correctly predicts that the tangential velocity contours within a radius of 50 km no longer move outwards. However, while the innermost contour moves inwards, the slab boundary layer model is unable to capture the full extent of the inward-moving tangential velocity contours seen in the ICON simulation. Although the radial velocity is consistently larger in the slab boundary layer model than the ICON simulation, the slab boundary layer model correctly predicts the expansion of radial velocity contours during CW1 and CW2 followed by the contraction in WF. Moreover, there is good agreement with the strengthening radial velocity between the latter half of CW2 and WF.

2.12.3 *Discussion*

The results for CW1 and CW2 are similar to the findings in Kilroy et al. (2016) for a decaying tropical cyclone and constant SST, where the slab boundary layer model predicted the expansion of the tangential and radial velocity contours. As with Kilroy et al. (2016),

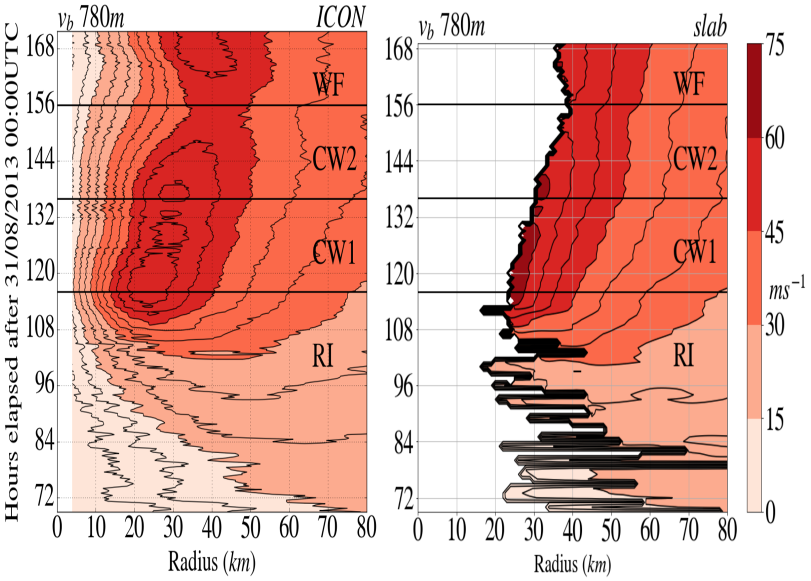

Figure 2.9: The tangential velocity in the boundary layer, v_b, is displayed as a Hovmöller plot for the ICON (left) and the slab boundary layer model (right). For the ICON simulation, v_b represents a vertical average of tangential velocity over the lower 780 m in the atmosphere. In the slab boundary layer model, the solution for v_b breaks down at the radius where the radial velocity becomes zero.

the expansion of the tangential and radial velocity contours show that an increasing radius of forced ascent is being controlled by the expanding outer circulation in the ICON simulation via boundary layer dynamics. Similar to CW1 and CW2, the slab boundary layer model can predict the contraction of the radial velocity contours and the innermost tangential velocity contour. Again, the agreement between the ICON simulation and slab boundary layer show that a decreasing radius of forced ascent is being determined by the expanding outer circulation through boundary layer dynamics. The inability of the slab boundary layer model to capture the full extent of the contraction of the tangential velocity contours during WF is likely to be related to the enhanced convective suction effect, which is not captured by the slab boundary layer model.

2.13 SUMMARY AND CONCLUSIONS

In summary, I examine how boundary layer dynamics modulate the intensity of a mature tropical cyclone that encounters a warm-core eddy in a coupled atmosphere-ocean model. After reaching peak intensity, the simulated tropical cyclone experiences a period of decay following the interaction with its cold wake and subsequently re-intensifies as it encounters the warm-core eddy. The changes in the structure of the tropical cyclone and its intensity are analysed with the help of a conceptual framework that recognises the importance of boundary layer dynamics, as well as the role played by air-sea coupling. A key part of the framework is the recognition that the change in the mean radius of updraught at the boundary layer top is regulated by the expanding outer tangential wind field through boundary layer dynamics.

I find that the decay of the tropical cyclone cannot be explained by air-sea coupling alone. During the early decay phase, the decrease in the average equivalent potential temperature of the boundary layer updraught is related to an increase in the mean radius of the updraught rather than the decrease in surface latent heat flux driven by sea-surface cooling. As a result, air-sea coupling does not influence the strength of the deep convection in the eyewall updraught and the accompanying outward movement of the eyewall updraught. Instead, the outward movement of the eyewall updraught and the accompanying spin down is influenced by the increasing mean radius of the boundary layer updraught.

In contrast to earlier in the decay phase, both air-sea coupling and boundary layer dynamics are important later in the decay phase. During this period, the equivalent potential temperature of the boundary layer updraught decreases on account of the decreasing surface latent heat flux, as well as the increasing mean updraught radius. The simultaneous weakening of the deep convection leads to a decrease in the vertical mass flux in the eyewall updraught. This weakening vertical mass flux causes the radial inflow above the boundary layer to weaken, which ultimately leads to a more pronounced spin down, corresponding to a more rapid decay, than earlier in the decay phase.

Similarly, boundary layer dynamics and air-sea interactions both play an important role for the re-intensification, where the tendencies are reversed. During the reintensification phase, the equivalent potential temperature of the boundary layer updraught increases on account of both increasing SST and surface latent heat flux, as well as the decreasing mean radius of the boundary layer updraught. The simultaneous strengthening of the deep convection leads to an increase in the vertical mass flux in the eyewall updraught. This increase in vertical mass flux leads to a strengthening radial inflow above the boundary layer and spin up, corresponding to re-intensification.

I complement the results of the process-based analysis with solutions from a steady-state boundary layer model. These solutions capture the increase in the radius of forced ascent during the decay phase and, to a lesser extent, the subsequent decrease during re-intensification. The agreement between these solutions and the ICON simulation provides evidence of the effect demonstrated by Kilroy et al. (2016). Namely, that the radius of forced ascent is controlled by the expanding outer circulation on account of non-linear boundary layer dynamics. In turn, the change in radius of forced ascent influences deep convection in the eyewall updraught, which then feeds back on the boundary layer flow.

In addition, my results highlights another layer of complexity to the coupling between surface latent heat flux, SST and near-surface wind speed through boundary layer dynamics. Changes in surface latent heat flux depend on changes in the near-surface wind linked to the boundary layer flow, which depend on whether convergence in the boundary layer is dominated by the non-linear dynamics of the boundary layer flow or the suction effect. Thus, any feedback between surface latent heat flux and tropical cyclone intensity in coupled models ultimately involves non-linear boundary layer dynamics. Further work is required to determine the importance of this coupling for the strength of the negative feedback.

Further work is also required to establish the link between the boundary layer flow and sea-surface cooling in coupled models. Changes in SST also depend on the nature of the boundary layer flow, because the wind stress at the sea surface that initiates sea-surface cooling is, as with the surface latent heat flux, a function of near-surface wind speed. Since changes in SST influence the surface latent flux, which ultimately affect the boundary layer flow, it is difficult to know how important this aspect is without coupled atmosphere-ocean simulations.

Taken together, my results show that boundary layer dynamics play an important role for the negative feedback and the tropical cyclone intensity response to a warm-core eddy in a coupled atmosphere-ocean model. By modulating the decrease in intensity in response to the strengthening sea-surface cooling, boundary layer dynamics affect the strength of the negative feedback between intensity and sea-surface cooling. Similarly, boundary layer dynamics influence the weakening of the negative feedback over the warm-core eddy by modulating the increase in intensity in response to the weakening sea-surface cooling.

3

THE IMPACT OF OCEAN EDDIES ON TROPICAL CYCLONE INTENSITY ON A GLOBAL SCALE

3.1 TROPICAL CYCLONE INTENSITY AND CLIMATE CHANGE

Over recent decades there has been an increase in the global proportion of tropical cyclones intensifying into the most severe category 4 or category 5 storms. The balance of evidence suggests that the increase is partly attributable to anthropogenic climate change (Knutson et al., 2019). Due to the disproportionately large economic damage they inflict and the loss of life they cause, the number of these intense (Category 4 - 5) tropical cyclones is an important measure for the societal impact of all tropical cyclones (Christensen et al., 2013). Accurately predicting the change in the number of intense tropical cyclones in the future is especially important for decision makers responsible for mitigation and adaptation measures (Masson-Delmotte et al., 2021).

Projections of future changes in tropical cyclone intensity are based on climate simulations run with general circulation models (GCMs). GCMs derive their name from their ability to simulate the large-scale general circulation in the atmosphere. Accordingly, the grid used in GCMs covers the entire globe. The range and complexity of physical processes simulated in GCMs is similar to that of Numerical Weather Prediction (NWP) models used for intensity forecasting.

The majority of climate simulations run with GCMs project a future decrease in the overall number of tropical cyclones, but an increase in the global proportion of intense tropical cyclones (Knutson et al., 2020). A recent climate simulation with a coupled atmosphere-ocean GCM shows not only a future increase in the proportion of intense tropical cyclones, but also an increase in their frequency (Bhatia et al., 2018). The authors find that the increased frequency of intense tropical cyclones is consistent with an increase in the extent of oceanic regions with conditions conducive to intensification. Additionally, the authors find that the increase in the number of intense tropical cyclones is linked to an increase in the average intensification rates.

3.2 LIMITATIONS OF CLIMATE SIMULATIONS

Many of the climate simulations used for future projections of tropical cyclone intensity are run with atmosphere-only GCMs (Bacmeister et al., 2018; Murakami et al., 2012; Sugi et al., 2016; Wehner et al., 2018; Yamada et al., 2017). Without an ocean component, these simulations do not capture the negative feedback between intensity and sea-surface cooling. Given the current limitations in computing power, downscaling methods have been deployed to generate projections that take the negative feedback into account. For intensity projections, downscaling is a two-step process consisting of a global climate simulation run with an atmosphere-only GCM followed by regional simulations using a coupled atmosphere-ocean model with substantially smaller horizontal grid spacing (Bender et al., 2010; Knutson et al., 2013, 2015). The tropical cyclones that form in the global climate simulation are extrapolated and simulated in the coupled regional models which simulate the negative feedback. A major disadvantage of downscaling is that the tropical cyclones simulated in the regional models cannot affect the climate simulated in the GCMs (Emanuel, 2013).

More recently, climate simulations have been carried out without downscaling by using coupled atmosphere-ocean GCMs (Bhatia et al., 2018; Kim et al., 2014; Ogata et al., 2016). In contrast to downscaling methods, simulations with coupled GCMs capture both the negative feedback and any effect the tropical cyclone has on the surrounding environment, which in turn influences the climate. However, the grid spacing of the ocean models used is too coarse to resolve warm-core ocean eddies, which are a highly localised phenomena (Kirtman et al., 2012; Knutson et al., 2020). As a result, there are no projections of future tropical cyclone intensity based on climate simulations in coupled GCMs that resolve warm-core eddies, referred to as eddy-resolving simulations.

Eddy-resolving simulations not only resolve warm-core eddies, but also resolve cold-core eddies. Similar to warm-core eddies, cold-core eddies are rotating water masses with a mixed layer that differs in temperature and depth from the background flow. Both cold-core and warm-core eddies are more generally referred to as ocean eddies. In contrast to warm-core eddies, cold-core eddies have a mixed layer that is shallower and cooler than the surrounding environment. As a result, cold-core eddies have a mixed-layer heat content that is smaller than the surrounding environment. When a tropical cyclone encounters a cold-core eddy, the sudden decrease in heat content leads to an enhancement of sea-surface cooling and, hence, a strengthening of the negative feedback.

The absence of eddy-resolving climate simulations means that it is unclear what role ocean eddies play for tropical cyclone intensity in a warming climate. The attribution of numerous rapidly-intensifying tropical cyclones to warm-core eddies suggests that using eddy-resolving ocean models may alter the average intensity and rate of intensification in current climate simulations. At the same time, any increase in intensity or intensification rates may be offset by cold-core eddies, which strengthen the negative feedback. If one effect is more pronounced that the other, the lack of eddy-resolving simulations may lead to a bias in current climate simulations. However, before quantifying whether the lack of eddy-resolving climate simulations may skew future projections, it is necessary to ask what effect warm-core and cold-core eddies have on tropical cyclone intensity on a global scale in the current climate.

3.3 GLOBAL ASPECTS OF INTERACTIONS BETWEEN OCEAN EDDIES AND TROPICAL CYCLONES

The impact of ocean eddies on a global scale depends on the frequency with which tropical cyclones encounter them. The frequency of encounters in turn depends on the formation and movement of the ocean eddies, which are carried by the background ocean flow (Olson, 1991). Tracking ocean-eddy movements is possible with altimetry data collected by satellites, in which warm-core and cold-core eddies appear as a respective maxima and minima in the sea surface height (Chelton et al., 2007). A study comparing the tracks of eddies and tropical cyclones found that 90% of tropical cyclones in the western Pacific between 2002 and 2011 encountered ocean eddies, indicating that such encounters may be common on the global scale (Ma et al., 2017).

Although satellites reveal the presence of ocean eddies through altimetry measurements, they cannot reveal their subsurface ocean structure (Brokaw et al., 2020). Instead, in situ measurements are required. Around 4000 autonomous measurement devices known as ARGO floats are spread over the world's oceans and collect in situ data in real time (Jayne et al., 2017). Data collected from ARGO floats has recently been used to analyse in detail the changes in the subsurface structure of ocean eddies and the sea-surface cooling that occurs when a tropical cyclone passes overhead (Li et al., 2021; Sadhuram et al., 2012; Sun et al., 2012). However, while a large part of the world's ocean is sampled by ocean floats, there is on average only one ARGO float in a 3° x 3° latitude-longitude box (Li et al., 2021). As a result, the network of ARGO floats cannot fully resolve the structure of individual ocean eddies, let alone on a global scale. Without knowledge of the depth and temperature of the mixed layer of the ocean eddies, one cannot say to what extent warm-core and cold-core eddies respectively suppress and enhance sea-surface cooling.

The extent to which ocean eddies alter sea-surface cooling depends on complex processes at play in the upper ocean. Three processes in the upper ocean are primarily responsible for sea-surface cooling induced by tropical cyclones: entrainment, vertical mixing and upwelling (Price, 1981). Entrainment refers to the process whereby water at the bottom of the mixed layer entraps and brings in colder waters from the thermocline below. Once the cold water enters the mixed layer, vertical mixing distributes the cold thermocline water throughout the depth of the mixed layer. Cold thermocline water can also enter the mixed layer via upwelling. Upwelling refers to the upward movement of water that replaces surface water above, which diverges due to the wind stress exerted by the tropical cyclone. The complication is that the contribution of these processes to sea-surface cooling is sensitive to the background oceanic flow (Jaimes et al., 2009a). Therefore, the impact of an ocean eddy on the intensity of a tropical cyclone passing overhead is also sensitive to the background oceanic flow.

3.4 RESEARCH QUESTION

There are many studies that model the effect of ocean eddies on tropical cyclone intensity. However, most focus on case studies where individual tropical cyclones encounter ocean eddies (Hong et al., 2000; Lin et al., 2005; Ma et al., 2013; Yan et al., 2017). While Ma et al. (2017) study the effect of ocean eddies over the western Pacific with a regional coupled atmosphere-ocean model, their ocean model is not initialised with a background oceanic flow. Given the additional complexities associated with the background oceanic flow and the lack of subsurface measurements, it is hard to foresee the impact ocean eddies have on tropical cyclone intensity on a global scale. This is the research gap I address, which is summarised in the following research question.

What is the impact of ocean eddies on tropical cyclone intensity on a global scale in a coupled atmosphere-ocean model?

Answering the above research question is possible with a coupled atmosphere-ocean GCM that can capture the background oceanic flow, a realistic distribution of ocean eddies and tropical cyclones, and the complex physics processes at play. A realistic background oceanic flow and distribution of ocean eddies can be obtained via a process of ocean spin up, whereby time dependent atmospheric fields, such as wind and temperature, are prescribed at the sea surface. Ocean spin up also provides a way of recreating a physically sensible subsurface ocean structure despite the lack of eddy-resolving measurements.

3.5 STRATEGY TO ANSWER THE RESEARCH QUESTION

To answer this research question, I analyse a one year, coupled simulation with a realistic ocean-eddy field, the details of which are given in Section 3.6. I begin by identifying and tracking the tropical cyclones in the simulation. Once I extract the tropical cyclone tracks, I evaluate the climatology of the tropical cyclones simulated in the model against observational data in Section 3.7. Then, I identify the ocean eddies encountered by the tropical cyclones. After this, I separately analyse the impact of warm-core and cold-core eddies on tropical cyclone intensity in Section 3.8. For the warm-core eddy analysis, I divide all the tropical cyclones into two groups: those that encounter at least one warm-core eddy before reaching peak intensity (warm tracks) and those that do not (not-warm tracks). Between the two groups I compare the distribution of the maximum intensity attained over the life cycle of each tropical cyclone, known as the peak intensity. To gain insight into the strength of the negative feedback, I also compare the sea-surface cooling and surface latent heat flux supplied to the tropical cyclone. With a view to keep things simple, I average the sea-surface cooling and the surface latent heat flux for each tropical cyclone from the time of detection to the time of peak intensity. I repeat the analysis for the cold-core eddies with tropical cyclones divided into the following two groups: those that encounter at least one cold-core eddy before peak intensity (cold tracks) and those that do not (not-cold tracks). Finally, I present a summary and my conclusions in Section 3.9.

3.6 SIMULATION

The one-year, global simulation is run with the coupled atmosphere-ocean ICON model (Korn, 2017; Zängl et al., 2014). The horizontal grid spacing in the model is 5 km and the model is convection permitting. The background features in the ocean are obtained by spinning up the ocean with climatological atmospheric forcing. The atmospheric forcing is taken from the fifth generation ECMWF atmospheric dataset (ERA5) (Dee et al., 2011). After spin up, the atmosphere is initialised for 20th January 2020 and run in coupled mode for one year until 20th January 2021. The ocean eddies form during the spin up process, and the tropical cyclones form organically when the model is run in coupled mode.

3.7 TROPICAL CYCLONE CLIMATOLOGY

To evaluate the tropical cyclone climatology, I compare the simulated tropical cyclones to observations from the year 2020 and other years. Since the synoptic skill of the model is limited, the simulated tropical cyclones do not correspond to historical tropical cyclones that occurred in 2020. Also, the synoptic eddy field does not represent the eddy field from 2020. For this reason, I do not expect there to be a perfect match between observations from 2020 and simulation. Instead, I am interested in whether the global statistics of the simulated tropical cyclones are reasonable.

3.7.1 *Tracks*

I extract the tropical cyclone tracks with a tracking algorithm that uses thresholds for the mean sea-level pressure and the near-surface wind speed fields that are adjusted for the ICON simulation. A tropical cyclone is detected if the mean sea-level pressure is below 990 hPa and the maximum near-surface wind speed exceeds 17 ms^{-1}. Track points are detected at 2 hour intervals.

The tropical cyclones in the simulation are located in the Pacific Ocean, the Southern Indian Ocean and the North Atlantic Ocean, including the Gulf of Mexico. Besides the lack of tracks in the North Indian Ocean, the geographical region covered by the tracks is in agreement with tropical cyclone climatology. The greater number of tracks in the Northern Hemisphere than the Southern Hemisphere is also consistent with the observational record.

3.7.2 *Intensity and frequency*

The model simulates a total of 66 tropical cyclones (category 1 - 5). This number is substantially larger than the 45 tropical cyclones observed in 2020 and the yearly mean of 47.5 tropical cyclones between 1981 and 2010. The number of simulated tropical cyclones also exceeds the yearly record between 1972 and 2020 of 59. However, there is good agreement in terms of major tropical cyclones (category 3 - 5), defined as being category 3 or stronger. The number of 24 simulated major tropical cyclones is similar to the observed 21 in 2020 and the yearly mean of 23.4 between 1981 and 2010. The number of major tropical cyclones is much lower than the record of 39 for the period from 1972 until 2020. Also, the accumulated cyclone energy, which is an aggregated measure of tropical cyclone frequency, intensity and duration, lies between the observed value for 2020 and the mean value for the period 1981 to 2010.

The frequency with which the simulated tropical cyclones form varies over the course of the year. The monthly frequency peaks in August, which is consistent with the observations from 2020. The peak in August reflects the larger number of tropical cyclones in the Northern Hemisphere. A smaller peak in March corresponds to the simulated height of the tropical cyclone season in the Southern Hemisphere. In the observations for 2020, this peak occurs in February, a month earlier than the simulation. It is not clear why there are no tropical cyclones simulated in April.

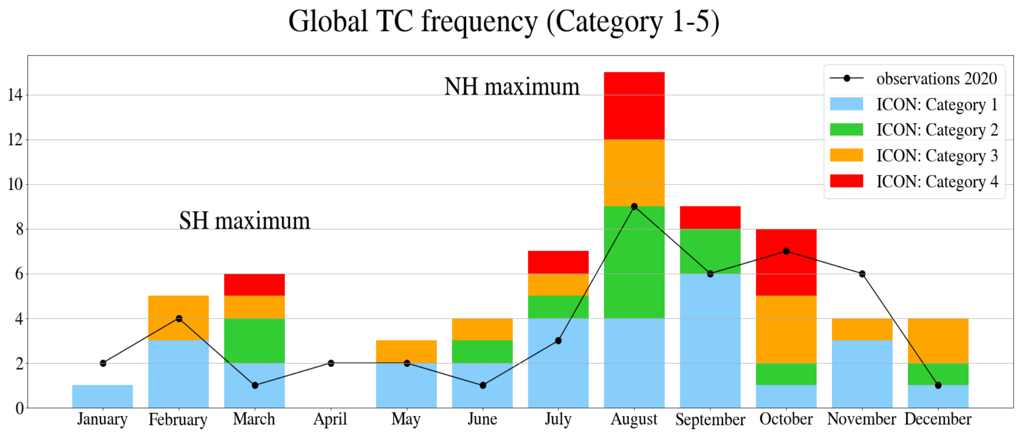

Figure 3.1: Comparison between simulated monthly tropical-cyclone frequency across the globe with observations from 2020. The frequency for the simulated tropical cyclones is shown as a stacked bar chart sorted according to category.

None of the simulated tropical cyclones intensify into category 5 tropical cyclones. The months with the largest number of simulated major tropical cyclones are August and October with 6 each. All the category 4 tropical cyclones in the Northern Hemisphere occur between the beginning of July and the end of October. These are the four months with the largest number of tropical cyclones. With the exception of one category 4 tropical cyclone in the Gulf of Mexico, all category 4 tropical cyclones are found in the Pacific region.

It is not clear why the model simulates too many tropical cyclones throughout the year compared to the observations for 2020. On the one hand, the environmental factors, notably sea-surface temperature and vertical wind shear, may be too conducive to tropical cyclone genesis. One large-scale phenomena that may be responsible for the discrepancy is the Madden-Julian Oscilation, which modulates tropical cyclone frequency globally and has been shown to be highly model dependent (Camargo et al., 2009, 2016; Klotzbach, 2014; Klotzbach et al., 2015; Satoh et al., 2012). On the other hand, there are large differences in tropical cyclone frequency across models that have similar genesis indices, which are used to estimate the probability of genesis based on environmental parameters (Camargo, 2013). This discrepancy suggests that the frequency is more strongly controlled by the dynamics of the tropical cyclone circulation simulated in the model than the large scale environment (Camargo et al., 2016).

3.7.3 *Pressure-wind relationship*

The pressure-wind relationship examines the two measures of tropical cyclone intensity: the minimum mean sea-level pressure at the centre of the tropical cyclone and the maximum near-surface wind speed. The two variables are negatively correlated in observations, with pressure decreasing with increasing wind speed. For category 1 tropical cyclones, there is an overlap between the observed and simulated pressure-wind relation-

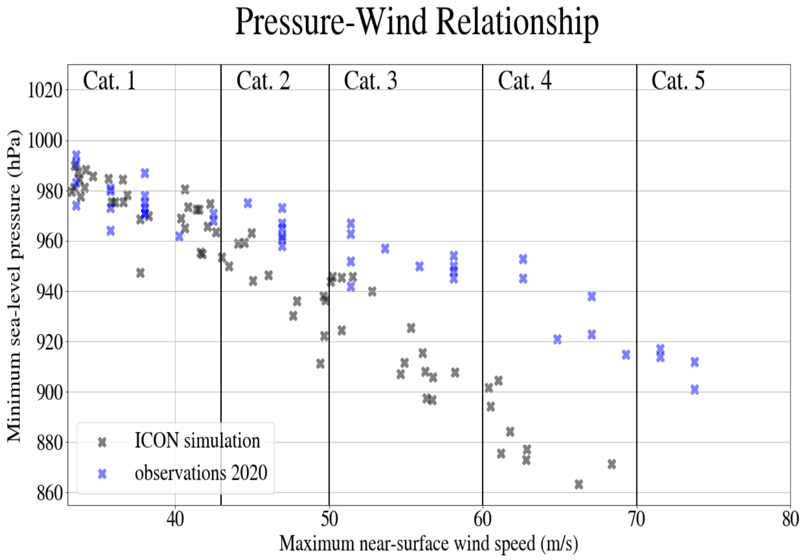

Figure 3.2: Comparison between the simulated pressure-wind relationship and the observed pressure-wind relationship for 2020.

ships. However, the pressure-wind relationship diverges for tropical cyclones as intensity increases above category 2. In this range, the simulated tropical cyclones have a maximum near-surface wind speed that is lower than observations for a given minimum mean sea-level pressure. Interestingly, the gap between the observed and simulated tropical cyclones diverges with increasing maximum near-surface wind speed. One possible explanation for the diverging relationship is the way the surface drag is parameterised in the model. In the ICON model, the surface drag coefficient increases linearly with wind speed. Bao et al. (Oct. 2012) showed that switching from a surface drag coefficient that increases linearly with wind speed to one that increases and then plateaus beyond a certain wind speed leads to tropical cyclones with a higher minimum mean sea-level pressure but a similar maximum near-surface wind speed.

3.7.4 *Sea-surface cooling*

To define sea-surface cooling, one has to specify a time period over which the sea surface cools. Here, I define sea-surface cooling as the change in the SST from 24 hours before to 24 hours after the tropical cyclone is directly overhead. With this definition, I find that the maximum sea-surface cooling that a tropical cyclone experiences over its lifetime increases with category. This positive relationship also exists between the sea-surface cooling averaged along the entire track of each tropical cyclone and category. Since there are no category 5 tropical cyclones, category 4 tropical cyclones experience the largest track-averaged sea-surface cooling. In agreement with observations, the track-averaged sea-surface cooling does not increase substantially above category 2 (Lloyd et al., 2011).

3.7.5 *Evaluation of tropical cyclone climatology*

Overall, the ICON model performs reasonably well in terms of tropical cyclone climatology. The distribution of tropical cyclone tracks is realistic, with the exception of the lack of tropical cyclones in the Bay of Bengal. The model simulates a very active tropical cyclone year, with the number of tropical cyclones reaching at least category 1 exceeding the yearly record for the period 1972 to 2020. However, the number of major tropical cyclones (category 3 - 5) is in good agreement with observations. The two simulated peaks in the monthly frequency corresponding to each hemisphere indicate that the model does a reasonable job of not only capturing the spatial distribution of tropical cyclones, but also their temporal distribution. The relationship between sea-surface cooling and intensity is also broadly in agreement with observations, suggesting that the air-sea coupling and the negative feedback in the model are well represented. The main identified shortcoming of the model is the simulated pressure-wind relationship, which diverges from the observed pressure-wind for major tropical cyclones.

3.8 IMPACT OF OCEAN EDDIES ON TROPICAL CYCLONE INTENSITY

The ability of the ICON model to simulate a reasonable tropical cyclone climatology suggests that the simulation is suitable for investigating the impact of ocean eddies on tropical cyclone intensity. Here, I begin by examining the frequency of encounters between tropical cyclones and ocean eddies. Then I analyse the effect of warm-core and cold-core eddies separately on tropical cyclone intensity. Finally, I discuss my results and possible limitations.

3.8.1 *Frequency of encounters*

I define an encounter between a tropical cyclone and an ocean eddy when at least one track point, which corresponds to the centre of the tropical cyclone, lies within the eddy. This definition is conservative, given that tropical cyclones typically have a much larger radius than ocean eddies (Ma et al., 2017). Nevertheless, I choose this definition, because the the surface latent heat flux supplied to the tropical cyclone is most sensitive to the sea-surface cooling in the inner region, where the wind speeds are strongest (Cione et al., 2003).

I find that encounters between tropical cyclones and ocean eddies are common, despite the conservative definition of an encounter. A total of 107 ocean eddies are encountered by the 66 tropical cyclones, which equates on average to more than one ocean eddy encounter per tropical cyclone. Of these ocean eddies, 63 are cold-core eddies, and 44 are warm-core eddies. The larger number of cold-core eddies encountered compared to warm-core eddies is in agreement with Ma et al. (2017), who find that tropical cyclones in the Northwest Pacific encountered more cold-core eddies than warm-core eddies between 2002 and 2011. The eddy encounters are not evenly distributed across the tropical cyclones. In total, more than 70% of all the 66 tropical cyclones encounter at least one ocean eddy and 45% encounter two or more. There are even tropical cyclones that encounter up to five ocean eddies.

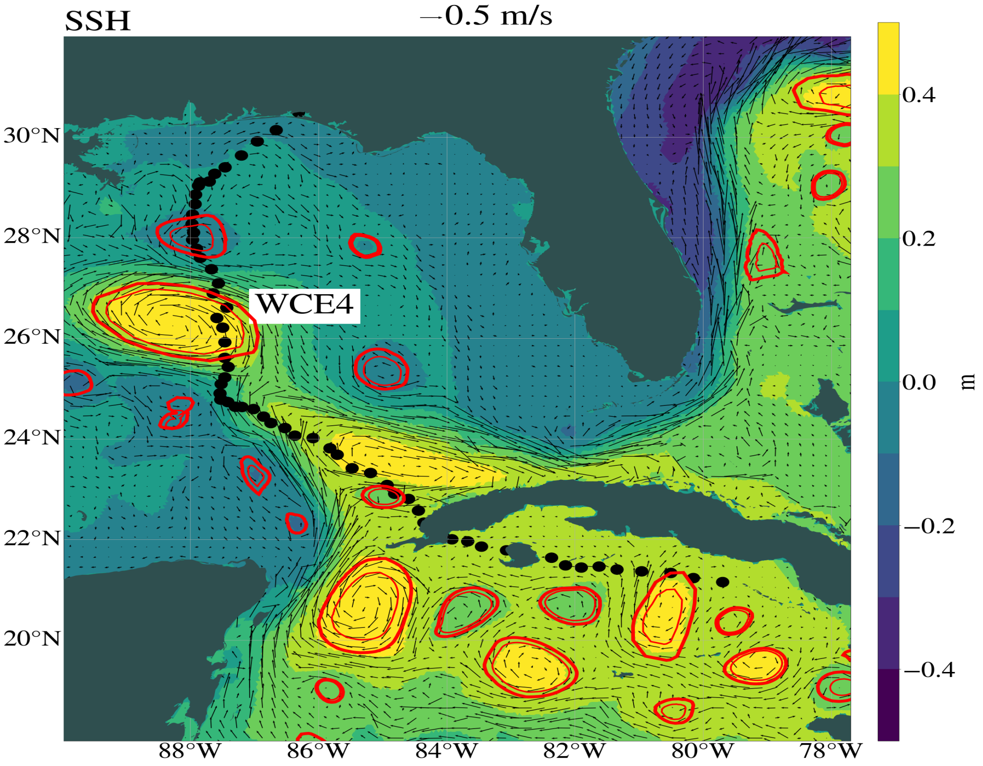
SSH
→0.5 m/s
WCE4
30°N
28°N
26°N
24°N
22°N
20°N
88°W
86°W
84°W
82°W
80°W
78°W
0.4
0.2
0.0
−0.2
−0.4
m

Figure 3.3: Snapshot of sea-surface height overlaid with red contours showing the ocean eddies identified by the algorithm. The surface current is displayed in both plots with black arrows scaled according to the magnitude. The solid black circles indicate the track points of the tropical cyclone, which encounters a large warm-core eddy (WCE4) in the Gulf of Mexico before making landfall further north.

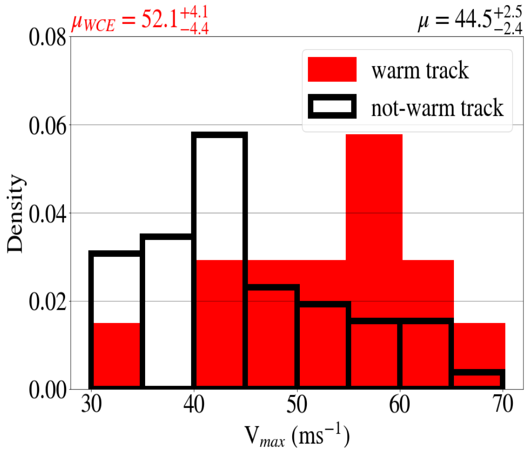

Figure 3.4: Normalised histogram of the peak intensity, V_{max}, for warm-track and not-warm-track tropical cyclones. The mean for the warm-track tropical cyclones, μ_{WCE}, and not-warm-track tropical cyclones, μ, are given with their respective 95% confidence intervals.

3.8.2 *Tropical cyclone statistics for warm-core and cold-core eddies*

Having identified the ocean eddies encountered by the tropical cyclones, I compare the peak intensity of the tropical cyclones that encounter at least one warm-core eddy before reaching peak intensity (warm track) with those that do not (not-warm track). I find that there is a difference in the average peak intensity between the two groups that is statistically significant to the 95 % confidence level. The not-warm-track tropical cyclones reach an average peak intensity of 44.5 ms^{-1}, whereas the warm-track tropical cyclones reach a higher average peak intensity of 52.1 ms^{-1}. The difference between the two is substantial, with the average peak intensity corresponding to category 3 for the warm-track tropical cyclones compared to category 2 for the not-warm track tropical cyclones.

I find a similar difference between warm-track and not-warm track tropical cyclones for the surface latent heat flux. Here, I average the surface latent heat flux for each tropical cyclone from the time it is initially detected to the time it reaches peak intensity. The warm-track tropical cyclones experience on average a track-averaged surface latent heat flux of 1150 Wm^{-2}, which is higher than the 830 Wm^{-2} for the not-warm-track tropical cyclones. Similar to the peak intensity, the difference in the surface latent flux between the two groups is statistically significant to the 95 % confidence level.

While there is a statistically significant difference for peak intensity and the surface latent heat flux, the same is not true for the sea-surface cooling. As with the surface latent heat flux, I average the sea-surface cooling for each tropical cyclone from the time of initial detection to the time of peak intensity. Warm-track tropical cyclones experience on average a slightly weaker track-averaged sea-surface cooling of 1.2 K compared to 1.3 K for not-warm-track tropical cyclones. In contrast to the peak intensity and surface latent heat flux, this difference is not statistically significant to the 95 % confidence level.

Repeating the process for cold-core eddies shows a different relationship between peak intensity, track-averaged surface latent flux and track-averaged sea-surface cooling. Tropical cyclones that encounter at least one cold-core eddy before reaching peak intensity (cold track) reach on average a peak intensity of 46.8 ms^{-1}, which is higher than the value of 45.8 ms^{-1} for those tropical cyclones that do not encounter any cold-core eddies before reaching peak intensity (not-cold track). In contrast to the comparison for warm-core eddies, the difference in average peak intensity between cold-track and not-cold-track tropical cyclones is not statistically significant.

For the track-averaged surface latent heat flux, the difference between cold-track and not-cold-track tropical cyclones is also not statistically significant. While there is no statistically significant difference, it is interesting to note that cold-track tropical cyclones experience a lower track-averaged surface latent heat flux of 830 Wm^{-1} compared to the value of 930 Wm^{-2} for not-cold-track tropical cyclones.

Similarly, there is no statistically significant difference for the track-averaged sea-surface cooling when comparing cold-track with not-cold track tropical cyclones. Again, it is interesting to observe that cold-track tropical cyclones experience on average a larger track-averaged sea-surface cooling of 1.5 K compared to the 1.1 K experienced by not-cold-track tropical cyclones.

3.8.3 *Discussion*

The high frequency of encounters between tropical cyclones and ocean eddies indicates that ocean eddies play an important role for intensity for many of the simulated tropical cyclones. The presence of these eddies along the tropical cyclone tracks influences the strength of sea-surface cooling, surface latent heat flux and, hence, the strength of the negative feedback.

The comparison between warm-track and not-warm-track tropical cyclones suggests that warm-core eddies have a significant effect on tropical cyclone intensity on a global scale. Furthermore, these results are consistent with the notion that warm-core eddies weaken the negative feedback. Despite the higher peak intensity, warm-track tropical cyclones experience a similar level of sea-surface cooling to the not-warm tracks. This discrepancy suggests that warm-core eddies suppress the sea-surface cooling, which allows tropical cyclones to intensify further.

The limitation of the statistical analysis is that it does not provide a definitive answer as to whether warm-core eddies are actually responsible for the difference in average peak intensity. Other factors could be behind the difference in peak intensity and track-averaged surface latent heat flux. If tropical cyclones that reach higher peak intensities have longer tracks, then there is the possibility that these tropical cyclones are more likely to encounter warm-core eddies compared to tropical cyclones with a lower peak intensity and shorter tracks. Further investigation is required to examine the extent to which warm-core eddies are behind the difference in average peak intensity and determine the robustness of these results.

In contrast to the analysis for warm-core eddies, the comparison between the cold-track and not-cold-track tropical cyclones suggests that cold-core eddies do not have a significant effect on tropical cyclone intensity on a global scale. While cold-core eddies may strengthen the negative feedback for individual tropical cyclones, such an effect is not evident across all tropical cyclones. These results can be interpreted in two ways. Either cold-core eddies are not as important for tropical cyclone intensity on a global scale as other environmental factors, or the effect of cold-core eddies is more subtle than strengthening the negative feedback by enhancing the sea-surface cooling. As my analysis examines the effect of cold-core eddies in isolation from warm-core eddies, it is not clear how warm-core eddies affect the difference in peak intensity between the cold-track and not-cold-track tropical cyclones. Differences between cold-track and warm-track tropical cyclones are difficult to interpret, since cold-track tropical cyclones may also encounter warm-core eddies and warm-track tropical cyclones may encounter cold-core eddies.

3.9 CONCLUSIONS

In conclusion, my results suggest that warm-core eddies have a statistically significant impact on peak tropical cyclone intensity on a global scale by weakening the negative feedback. My findings do not indicate that cold-core eddies have a statistically significant impact on peak intensity. Further work is required to see if these results are robust and whether the difference in peak intensity can be directly attributed to warm-core eddies.

One shortcoming of the model that affects the robustness of these results is the pressure-wind relationship. The simulated pressure-wind relationship deviates from the observed pressure-wind relationship, especially for major tropical cyclones. The deviation is likely to be linked to the parameterisation of surface drag and the choice of boundary layer parameterisation. Since the tropical cyclones that encounter at least one warm-core eddy strengthen on average into a major tropical cyclone, choosing a different boundary-layer or surface-drag parameterisation may have a considerable effect on the peak intensity of these tropical cyclones.

Despite the tentative nature of my findings, they open the door to the possibility that the lack of eddy-resolving climate simulations introduces a bias in future projections of tropical cyclone intensity. Resolving warm-core eddies in climate simulations may increase the number of intense tropical cyclones simulated, which would point to current models underestimating the projected increases in intense tropical cyclones.

4

SUMMARY AND CONCLUSIONS

In this thesis, I investigated the impact of warm-core eddies on tropical cyclone intensity. Warm-core eddies are especially pertinent to tropical cyclone intensity, because they have been linked to the rapid intensification of several tropical cyclones. Rapidly intensifying tropical cyclones are both notoriously difficult to forecast and particularly dangerous for coastal communities in their path. A better understanding of how warm-core eddies affect tropical cyclone intensity is required to improve intensity forecasts and to minimise the economic and human costs of landfalling tropical cyclones.

The effect warm-core eddies have on tropical cyclone intensity is often described in the context of a negative feedback. This negative feedback arises because the wind-stress exerted by the tropical cyclone at the sea surface churns the upper ocean, causing the sea surface to cool. This sea-surface cooling leads to a decrease in the surface latent heat flux. By decreasing the surface latent heat flux, the sea-surface cooling acts as a brake on tropical cyclone intensification. Warm-core eddies weaken this negative feedback by suppressing the sea-surface cooling, allowing the tropical cyclone to reach a higher intensity.

To investigate the impact of warm-core eddies on tropical cyclone intensity, I analysed simulations run with a coupled atmosphere-ocean model that captures the negative feedback. The coupled model is similar in complexity to NWP models used for intensity forecasting and simulates the full range of complex physical processes that underlie the negative feedback.

4.1 RESEARCH QUESTION 1

In the first part of my thesis, I examined the role of boundary layer dynamics for tropical cyclone intensity in a coupled atmosphere-ocean model. The key aspects of boundary layer dynamics relevant to tropical cyclone intensity are highlighted in the rotating-convection paradigm for spin up. While these aspects have been shown to be important for tropical cyclone intensity in atmosphere-models, they have not been investigated in coupled atmosphere-ocean models. This led me to my first research question:

Are boundary layer dynamics important for the negative feedback and the tropical cyclone intensity response to a warm-core eddy in coupled atmosphere-ocean models?

To answer this research question, I analysed a coupled simulation of a tropical cyclone that encounters a warm-core eddy using a conceptual framework, which extends the rotating-convection paradigm to include air-sea coupling. I focused on the changes in intensity in the mature phase after the tropical cyclone reaches peak intensity. In the mature phase, the intensity decreases following the formation of a cold wake. This decrease is gradual and then more rapid. Subsequently, the tropical cyclone reintensifies during its encounter with the warm-core eddy.

My results show that the aspects of boundary layer dynamics in the rotating-convection paradigm are crucial to understanding the gradual and rapid decrease in intensity, as well as the reintensification. Moreover, the differing rates at which the intensity decreases cannot be explained without boundary layer dynamics. By modulating these changes in intensity in response to sea-surface cooling, boundary layer dynamics play an important role for the negative feedback and the intensity response of the simulated tropical cyclone to the warm-core eddy.

The central role played by boundary layer dynamics for the negative feedback underscores the importance of accurately representing the boundary layer flow in coupled atmosphere-ocean models. In atmosphere-only models, tropical cyclone intensity has been shown to be sensitive to the choice of boundary layer schemes, which parameterise the diffusion of momentum and heat in the boundary layer that occurs on sub-grid scales (Bu et al., 2017; Gopalakrishnan et al., 2013; Kepert, 2012; Rai et al., 2018; Smith et al., 2014, 2010b; Srinivas et al., 2008). Recently, Zhang et al. (Apr. 2017) show that intensity forecasts of tropical cyclones undergoing rapid intensification are improved when the parameterised vertical diffusion of momentum is reduced (ibid.). They link the improved forecasts to the ability of the model to accurately capture the structural changes in the tropical cyclone circulation, including the strength of boundary layer convergence. Furthermore, they reiterate the need to evaluate model performance based on metrics relating to the structure of the topical cyclone (Zhang et al., 2015b).

To the best of my knowledge, the sensitivity of tropical cyclone intensity and rapid intensification to boundary layer schemes has not been investigated in coupled atmosphere-ocean models. The need to investigate this sensitivity is evident from the study by Raju et al. (Sept. 2011), who show that simulating the rapid intensification of Cyclone Nargis over a warm-core eddy depends on the choice of boundary layer scheme. Despite Cyclone Nargis rapidly intensifying over a warm-core eddy, the authors use an atmosphere-only model.

By being the first study that investigates the effect of a warm-core eddy on the kinematic and thermodynamic structure of the tropical cyclone boundary layer in a coupled atmosphere-ocean model, my results can help researchers understand the sensitivity of tropical cyclone intensity and the negative feedback to boundary layer schemes in coupled atmosphere-ocean models. A comprehensive understanding of this sensitivity in coupled models is crucial to improving intensity forecasts, including for tropical cyclones that rapidly intensify over warm-core eddies.

4.2 RESEARCH QUESTION 2

In the second part of my thesis, I explored the impact of both warm-core and cold-core eddies on tropical cyclone intensity on a global scale. In contrast to warm-core eddies, cold-core eddies enhance sea-surface cooling and strengthen the negative feedback. While warm-core and cold-core eddies, referred to as ocean eddies, have a substantial effect on the strength of the negative feedback for individual tropical cyclones, they are not resolved in global climate simulations. Without global simulations that resolve ocean eddies and tropical cyclones, it is very difficult to foresee the impact of ocean eddies on tropical cyclone intensity. Since no simulation of this kind has been examined in the context of ocean eddies and tropical cyclone intensity, it is not clear whether resolving ocean eddies in climate simulations would affect the projected future changes in intensity. This led me to my second research question:

What is the impact of ocean eddies on tropical cyclone intensity on a global scale in a coupled atmosphere-ocean model?

To answer this research question, I analysed a one-year, global coupled atmosphere-ocean simulation initialised with a realistic ocean-eddy field. I compared the tropical cyclones that encounter a warm-core eddy before reaching peak intensity with those tropical cyclones that do not. Then I compared the tropical cyclones that encounter a cold-core eddy before reaching peak intensity with those that do not.

My results show that the tropical cyclones that encounter warm-core eddies reach on average a higher peak intensity than those that do not. Additionally, the tropical cyclones that encounter warm-core eddies experience a larger surface latent heat flux and a similar degree of sea-surface cooling compared to the remaining tropical cyclones. These results are consistent with the notion that warm-core eddies are weakening the negative feedback by suppressing sea-surface cooling, allowing the tropical cyclones to intensify further.

In contrast to warm-core eddies, tropical cyclones that encounter cold-core eddies do not reach on average a peak intensity that is different from the peak intensity of those that do not. These results suggest that cold-core eddies are less important for tropical cyclones intensity on a global scale than warm-core eddies.

While further work is required to establish the robustness of my results, they indicate that the lack of eddy-resolving climate simulations may lead to biases in future projections of tropical cyclone intensity. Given that warm-core eddies appear to have a larger impact on tropical cyclone intensity than cold-core eddies, resolving ocean eddies may favour rapid intensification and lead to a larger number of intense tropical cyclones being simulated in climate models. However, the exact impact of resolving ocean eddies in climate simulations is not clear due to the underlying complexities of the coupling between the atmosphere and the ocean. Nevertheless, my results underscore the need to examine the impact of resolving eddies on climate simulations in future research.

Further advances in computational power will increase the feasibility of running eddy-resolving climate simulations with a grid spacing similar to current forecasting models. These climate simulations will present new opportunities to study the impact of ocean eddies on tropical cyclones in a warming world. At the same time, the smaller grid spacing will increase the complexity of these climate simulations. If the sensitivity of current forecasting models to boundary layer schemes is anything to go by, an understanding of boundary layer dynamics will be crucial to disentangle the impacts of ocean eddies on tropical cyclone intensity.

Part II

APPENDIX

A

RESPONSE OF A TROPICAL CYCLONE TO A SUBSURFACE OCEAN EDDY AND THE ROLE OF BOUNDARY LAYER DYNAMICS

A.1 ABSTRACT

We analyse a tropical cyclone simulated for a realistic ocean-eddy field using the global, non-hydrostatic, fully-coupled atmosphere-ocean ICOsahedral Nonhydrostatic (ICON) model. After intensifying rapidly, the tropical cyclone decays following its interaction with a cold wake and subsequently reintensifies as it encounters a subsurface, warm-core eddy. To understand the change in the azimuthal-mean structure and intensity of the tropical cyclone, we invoke a conceptual framework, which recognises the importance of both boundary-layer dynamics and air-sea interactions. Crucially, the framework recognises that the change in the mean radius of updraught at the boundary layer top is regulated by the expanding outer tangential wind field through boundary-layer dynamics. The decrease in the average equivalent potential temperature of the boundary-layer updraught during the early decay phase is related to an increase in the mean radius of the updraught rather than air-sea interactions. However, later in the decay phase, air-sea interactions contribute to the decrease, which is accompanied by a decrease in the vertical mass flux in the eyewall updraught and, ultimately, a more pronounced spin-down of the tropical cyclone. Air-sea interactions are important during reintensification also, where the tendencies are reversed, that is, the mean radius of the boundary-layer updraught decreases along with an increase in its average equivalent potential temperature and vertical mass flux. The importance of boundary-layer dynamics to the change in the azimuthal-mean structure is underscored by the ability of a steady-state slab boundary-layer model to predict an increasing and, to a lesser extent, a decreasing radius of forced ascent for periods of decay and reintensification, respectively. Finally, our simulation highlights the importance of the ocean-eddy field for tropical cyclone intensity forecasts, since the simulated warm-core eddy does not display any sea-surface temperature (SST) signal until it is encountered by the tropical cyclone.

A.2 INTRODUCTION

This study examines how the atmospheric boundary layer modulates the intensity of a mature tropical cyclone influenced by a realistic ocean-eddy field in a global, convection-permitting, coupled ocean-atmosphere model run at 5 km grid spacing[1]. The significance of the boundary layer to the spin-up and intensity of tropical cyclones is well established for atmosphere-only models (Montgomery et al., 2014, 2017). However, two crucial aspects of the boundary layer tested in atmosphere-only models remain unexplored in coupled simulations, where tropical cyclone intensity also varies significantly with subsurface ocean conditions. Firstly, boundary-layer dynamics exert control on the location of the updraught at the top of the boundary layer, which determines the location of the eyewall updraught. The location and strength of the eyewall updraught influence the radial advection of absolute angular momentum, M, above the boundary layer, a region where M is approximately conserved. If the eyewall updraught is strong enough, M is advected inwards. Otherwise, M is advected outwards. Secondly, the dynamics of the boundary-layer flow influences the surface latent heat flux, which depends inter alia on the near-surface wind speed. Since the surface latent heat flux also depends on subsurface ocean conditions, these two aspects motivate a closer examination of the boundary layer in coupled atmosphere-ocean models.

---

[1] The grid spacing in ICON is defined as the square root of the area of the triangular cells and is almost constant over the globe.

Studies using coupled atmosphere-ocean models established early on that the wind-stress-induced sea-surface cooling associated with tropical cyclones leads to a decrease in tropical cyclone intensity (Bender et al., 1993; Chang et al., 1979; Khain et al., 1991). The decrease can be significant, with tropical cyclone intensity up to 50% less compared with the case in which there is no sea-surface cooling (Schade et al., 1999). Capturing the sea-surface cooling in coupled models has improved tropical cyclone intensity forecasting, which previously relied on atmosphere-only models (Balaguru et al., 2018; Bender et al., 2000; Mogensen et al., 2017), considerably.

The sea-surface cooling initiated by the tropical cyclone depends on pre-storm subsurface ocean conditions. This is because the subsurface ocean structure influences the ocean processes that are primarily responsible for sea-surface cooling. These processes include entrainment, vertical mixing and upwelling associated with Ekman pumping, where cooler thermocline waters ascend into the mixed layer due to the divergence of warmer surface waters (Price, 1981). Furthermore, the subsurface ocean structure is shaped by background ocean eddies, which are predominantly found near major current systems. Warm-core eddies can limit the sea-surface cooling, whereas cold-core ocean eddies can enhance the sea-surface cooling (Jaimes et al., 2009b, 2016, 2015; Ma et al., 2017). Consequently, background eddies impact tropical cyclone intensity, as shown in numerical models of varying complexity (Lin et al., 2005; Ma et al., 2013; Wu et al., 2007b; Yablonsky et al., 2012; Yan et al., 2017). Warm-core eddies are of particular interest, because they are favourable for rapid intensification, particularly if the background, climatological ocean mixed layer is not deep (Lin et al., 2008). Given its impact on sea-surface cooling and tropical cyclone intensity, the subsurface ocean structure is considered to be of first-order importance for tropical cyclone intensity forecasting (Emanuel, 1999).

Sea-surface cooling influences tropical cyclone intensity by reducing the surface latent heat flux between ocean and atmosphere, which is the primary energy source for tropical cyclones (Emanuel, 1986). However, the process by which tropical cyclone intensity changes is far from straightforward. Recent studies using coupled models turn to Emanuel's influential paradigm to explain changes in tropical cyclone intensity due to a cold wake (Chen et al., 2017; Emanuel, 1995; Emanuel, 1997; Emanuel, 1989; Lee et al., 2014; Li et al., 2019). However, one shortcoming of this paradigm is that, while considering boundary-layer thermodynamics, it does not recognise the importance of atmospheric boundary-layer dynamics to spin up (Montgomery et al., 2014).

Boundary-layer dynamics exert a strong control on the radius at which the boundary-layer inflow turns upwards into the eyewall updraught (Abarca et al., 2015; Nguyen et al., 2002; Persing et al., 2013; Schmidt et al., 2016; Smith et al., 2009; Zhang et al., 2001; Zhang et al., 2015a). The thermodynamic characteristics of the updraught out of the boundary layer determine the rate of diabatic heating within the eyewall updraught (Smith et al., 2016). The boundary-layer updraught also advects tangential momentum vertically, which contributes significantly to spin-up in the eyewall updraught, provided sufficiently large tangential momentum is generated in the boundary layer (Kilroy et al., 2016; Persing et al., 2013; Schmidt et al., 2016; Smith et al., 2009). The tight coupling between the boundary layer and the eyewall updraught is further underscored by the finding that spin-down occurs if the eyewall updraught is not strong enough to accept the boundary-layer updraft (Smith et al., 2018).

Another important aspect of boundary-layer dynamics is the lack of gradient wind balance in the boundary layer. As a result, nonlinear advective terms cannot be neglected from the momentum equations in the boundary layer (Vogl et al., 2009). Kilroy et al. (2016) demonstrated with an atmosphere-only model that nonlinear boundary layer dynamics lead to nonlocal effects, whereby the expanding outer circulation leads to an increasing radius of forced ascent of boundary-layer air at the base of the eyewall updraught. By controlling the radius of forced ascent, boundary-layer dynamics play an active role in the radially outward movement of the eyewall updraught and, ultimately, the accompanying decrease in tropical cyclone intensity.

Although boundary-layer dynamics has been shown to play an important role for the radially outward movement of the eyewall updraught in atmosphere-only simulations, its role has not been examined in coupled simulations. Recent studies of the tropical cyclone cold wake attribute the radially outward movement of the eyewall updraught to decreasing surface latent heat flux and the accompanying weakening deep convection in the eyewall updraught (Chen et al., 2010b, 2017; Guo et al., 2020; Li et al., 2018; Ma, 2020). While these studies do examine the role of boundary-layer dynamics in determining the moisture transported inwards by the boundary layer, they do not examine the role of boundary-layer dynamics in determining the inner-core expansion. However, the foregoing discussion indicates that it is crucial to consider both boundary-layer dynamics and air-sea coupling to understand the inner-core expansion and the accompanying change in tropical cyclone intensity.

In this study, we investigate the influence of boundary-layer dynamics and air-sea coupling on the change in the location of the eyewall updraught and the intensity of a mature tropical cyclone. To this end, we use a simulation of a tropical cyclone run with the fully-coupled ICOsahedral Nonhydrostatic (ICON) model in a global configuration with 5 km horizontal grid spacing for both atmosphere and ocean (Korn, 2017; Zängl et al., 2015). The initialization of the atmosphere and ocean component of the ICON model includes a detailed subsurface ocean structure ahead of the tropical cyclone. The simulated tropical cyclone generates a cold wake that is sensitive to the initial subsurface ocean structure, which includes a warm-core eddy.

A description of the coupled ICON model and the simulation is provided in Section A.3. To set the scene for interpreting the simulation, we outline a simple conceptual framework to understand the coupling between the surface latent heat flux, the deep convection in the eyewall updraught and the boundary layer flow in Section A.4. This framework extends an existing framework to include the additional effects of atmosphere-ocean coupling. In Section A.5, we present results from the ICON simulation for the ocean and the atmosphere, and we discuss the change in tropical cyclone intensity in the context of the conceptual framework. In Section A.6, we extend the study by Kilroy et al. (2016) and run a steady-state, axisymmetric slab boundary-layer model with a prescribed tangential wind field (Smith, 2003). Prescribing the tangential wind field from the ICON simulation allows us to investigate the role of nonlinear boundary layer dynamics in controlling the radii of forced ascent and influencing the change in location of the eyewall updraught. A summary and conclusion follows in Section A.7.

A.3 ICON MODEL DESCRIPTION AND SIMULATION

To study the evolution of a mature tropical cyclone, we analyse a single tropical cyclone from an existing 40-day simulation that was run as part of the development of the 5-km, global, coupled atmosphere-ocean ICON model (Korn, 2017; Zängl et al., 2015). The global configuration allows us to avoid problems arising from a mismatch of physics between a nested region of interest and its boundaries (Emanuel, 2013). We chose this particular simulation because the tropical cyclone in question encounters a warm-core eddy, which provides a compelling case study of tropical cyclone intensity in a coupled model.

Although coupled simulations of tropical cyclones exist with a smaller horizontal grid spacing of 2 - 3 km, this is the first study of a tropical cyclone simulated in a global domain with no nesting and a grid spacing as low as 5 km for both the atmosphere and the ocean (Chen et al., 2017; Li et al., 2019). Because horizontal diffusion parametrised in boundary-layer schemes typically scales with the horizontal grid spacing in mesoscale models, simulated tropical cyclone intensity can increase when the horizontal grid spacing is decreased (Rotunno et al., 2009). At the same time, the effect on tropical cyclone intensity of decreasing the horizontal grid spacing may be limited due to factors that favour intensification at smaller grid spacing being compensated by factors that favour weakening (Fierro et al., 2009). Since our goal is to articulate the importance of boundary-layer dynamics for tropical cyclone intensity in a coupled simulation by analysing the qualitative behaviour of the processes outlined in the conceptual framework (section A.4), reducing the grid spacing is unlikely to change our analysis.

In the ICON simulation, there are 70 vertical levels in the atmosphere with a model top located at a height of 30 km. Nine of these vertical levels lie below 1 km, permitting adequate resolution of the boundary-layer flow. The ocean part of the model has 128 vertical levels, of which 12 are in the uppermost 100 m, and takes into account bottom topography with a maximum depth of 6400 m. The atmosphere and ocean are initialised separately prior to coupling. The atmosphere is initialised with ERA-Interim reanalysis corresponding to August 1, 2013 2013 (Dee et al., 2011). During spin-up of the ocean (not to be confused with tropical cyclone spin-up), the ocean is forced by climatological atmospheric fields. The initialisation of the ocean recreates background oceanic features, including ocean eddies and currents. After the spin-up of the ocean, the atmosphere and ocean are coupled and the model is run for 40 simulation days. Significant computational resources were required for the coupled simulation. A total of 420 nodes were utilised on the Mistral High Performance Computing system at the German Climate Computing Centre (DKRZ), yielding 30 simulated days per day.

Fluxes between the atmosphere and the ocean component are exchanged every 15 minutes. The ICON physics package is, in terms of simulated physical processes, identical to the package incorporated into the ECHAM atmospheric general circulation model (Giorgetta et al., 2018). Vertical transport at subgrid scales via turbulent motion is parameterised as turbulent diffusion. The implemented turbulence closure scheme is outlined in Mauritsen et al. (2007) and Pithan et al. (2015). The tuning of vertical diffusion is achieved through adjustment of the neutral Prandtl number, which is set to 0.7 in our simulation. While the ocean component of ICON resolves long surface gravity waves, short surface gravity waves, in particular breaking surface waves, are not resolved. However, a parameterization for the turbulent kinetic energy source caused by these breaking waves is applied as a simple source term in the turbulent kinetic energy equation of the Gaspar mixing scheme.

The cloud microphysics package includes warm-rain processes and the formation of cloud ice, but no graupel or hail. Although the inclusion of graupel does lead to more intense tropical cyclones, the difference in the simulated intensification rate and final intensity between a 2-ice and 3-ice scheme of the same type is small for strong tropical cyclones (Tao et al., 2011; Wang, 2002). The low sensitivity of the intensification rate and final tropical cyclone intensity may be due to the different microphysics schemes resulting in similar vertical profiles of diabatic heating and similar levels of downdraughts (Wang, 2002). Moreover, tropical cyclone intensity is significantly more sensitive to changes in the downdraught due to the evaporation of rain and cloud water or the melting of ice hydrometeors (Zhu et al., 2006). Another limitation of this model version is that rainwater cannot be advected horizontally. However, the lack of horizontal rainwater advection is likely to have a negligible effect on the distribution of diabatic heating, because water vapour can still be advected horizontally. This means that rainwater that evaporates into water vapour can then be advected horizontally into neighbouring grid cells, before recondensing into rainwater. Given that the distribution of clouds and precipitation in tropical cyclones is determined to a large extent by vertical mass transport (Houze, 2010), the effect of this limitation on the azimuthally averaged distribution of water in a mature tropical cyclone is likely to be minimal.

After performing the analysis of the current simulation, an error was found in the model code relating to the calculation of the wind stress. While the wind stress passed to the atmosphere used the ocean velocity with the wrong sign and an incorrect prefactor, the wind stress passed to the ocean did not include the ocean velocity at all. However, since the atmospheric velocity of the tropical cyclone at the surface is much larger than the underlying ocean velocity, the error in the wind-stress magnitude is relatively small. We do not expect that this error matters for our diagnostics.

A.4 A CONCEPTUAL FRAMEWORK FOR UNDERSTANDING TROPICAL CYCLONE INTENSITY CHANGE

To interpret the evolution of a tropical-cyclone-like vortex in any complex numerical simulation of the type examined here requires a suitable conceptual framework. The framework adopted here is the so-called rotating-convection paradigm (Montgomery et al., 2017), which is an extension of the cooperative paradigm of (Ooyama, 1982; Ooyama, 1969). The extension applies to a three-dimensional flow configuration and includes a boundary-layer spin-up mechanism as articulated by (Smith et al., 2009). Within this framework, we recognise explicitly the role of nonlinear boundary-layer dynamics in controlling the change in the radius of forced ascent at the top of the boundary layer on account of the expanding outer circulation (Kilroy et al., 2016). We extend the framework to consider the effect of atmosphere-ocean coupling on tropical cyclone intensity. This framework has not been used previously to investigate the change in simulated tropical cyclone intensity for coupled atmosphere-ocean models and can be understood as follows.

1. *Air-sea coupling*. Surface latent heat supplied to the tropical cyclone depends on the sea-surface temperature (SST), the near-surface wind speed and the near-surface moisture content. Changes in the surface latent heat flux lead to changes in the equivalent potential temperature, θ_e, in the boundary layer. The value of θ_e determines the buoyancy acquired by the air parcels in the boundary layer and whether they reach the level of free convection. Air parcels that do not reach the level of free convection remain negatively buoyant. Those that reach the level of free convection become positively buoyant and rise into the troposphere with a vertical velocity that depends on θ_e.

2. *Boundary-layer convergence via surface drag*. Surface drag leads to an inflow in the boundary layer. Due to the upward pressure-perturbation force that follows from mass continuity, the converging air is accelerated out of the boundary layer. The resulting vertical mass flux at the top of the boundary layer, $\overline{\rho w}_{BL}$, depends, in part, on the strength of the convergence in the boundary layer. The strength of convergence and the radial location at which the air is directed upwards are determined to a large extent by the nonlinear dynamics of the boundary-layer flow and the expanding outer circulation.

3. *Boundary-layer convergence via eyewall suction*. In addition to the convergence pushing out air mass from the boundary layer, deep convection in the eyewall updraught acts to suck air mass at the top of the boundary layer into the eyewall updraught above (Smith et al., 2015). Consequently, $\overline{\rho w}_{BL}$ depends on boundary-layer convergence via both surface drag and eyewall suction, effects that cannot be separated because of the nonlinearity of the flow dynamics.

4. *Vertical mass flux*. In contrast to $\overline{\rho w}_{BL}$, the vertical mass flux in the eyewall updraught, $\overline{\rho w}_{EW}$, is primarily buoyancy-driven and, therefore, more sensitive to changes in θ_e and ultimately air-sea coupling than to changes in $\overline{\rho w}_{BL}$. The change in $\overline{\rho w}_{EW}$ also depends on how the areal extent of the eyewall updraught changes. The vertical mass fluxes are important because they influence the evolution of the tropical cyclone structure. Due to mass continuity, mass flows out above the boundary layer if $\overline{\rho w}_{EW}$ is smaller than $\overline{\rho w}_{BL}$. Conversely, if $\overline{\rho w}_{EW}$ is greater than $\overline{\rho w}_{BL}$, there is inflow above the boundary layer.

5. *Advection of absolute angular momentum*. Any change of the inflow or outflow above the boundary layer is reflected in the radial advection of absolute angular momentum, M. A weakening inflow above the boundary layer decreases the ability of the tropical cyclone to advect M-surfaces radially inwards. Conversely, a strengthening inflow enhances the ability of the tropical cyclone to advect M-surfaces radially inwards.

6. *Tangential velocity change*. The radial advection of M-surfaces translates into local changes in the tangential velocity, v, which can be seen in the following expression for v in terms of M in the f-plane approximation,

$$v = \frac{M}{r} - \frac{1}{2}fr. \tag{A.1}$$

The radius and Coriolis parameter are given by r and f, respectively.

7. *Feedback on air-sea coupling*. Finally, the local change in the tangential velocity above the boundary layer leads to a change in the radial pressure gradient at the top of the boundary layer (assuming the flow is in approximate gradient-wind balance). This radial pressure gradient is transmitted into the boundary layer and leads to a change in the net radial force there. Through nonlinear boundary-layer dynamics, the change in the net radial force and the expanding outer circulation determine the change in the boundary-layer convergence and the radius of forced ascent. Since the accompanying change in the near-surface wind field influences the radial distribution of surface latent heat flux and, therefore, the air-sea coupling outlined in (1), the interaction between the boundary layer flow and surface latent heat flux forms a feedback loop.

Within this framework, the intensification of a mature tropical cyclone over a warm-core eddy can be understood as follows (please refer to Figure A.1). A higher surface latent heat flux leads to an increase in θ_e at the top of the boundary layer via air-sea coupling. Air parcels with higher θ_e then ascend from the boundary layer into the eyewall updraught at the radius of forced ascent. The vertical mass flux at the top of the boundary layer depends on the convergence due to surface friction and the suction effect of deep convection in the eyewall updraught. Assuming there is no warming aloft, the increase in mean θ_e of air parcels ascending into the eyewall leads to an increase in mean vertical velocity in the eyewall updraught and, if the areal extent of the eyewall updraught does not decrease appreciably, an increase in the vertical mass flux. The inflow and the inward advection of M increase in a vertical layer above the boundary layer at radii outside the eyewall updraught. The corresponding increase in the local tangential velocity increases the radial pressure gradient transmitted into the boundary layer, which changes the net radial force there. The change in the net radial force, along with the expanding outer circulation, leads to a change in the boundary-layer convergence and the radius of forced ascent. While one may expect an increase in the transmitted radial pressure gradient to increase the strength of the boundary-layer convergence and decrease the radius of forced ascent, one cannot know whether this is the case until one performs the calculation, due to the nonlinear nature of boundary-layer dynamics. A strengthening in the boundary-layer convergence would feedback on air-sea coupling, with increasing near-surface wind speed increasing the surface latent heat flux, assuming a constant moisture disequilibrium at the air-sea interface. In reality, moisture disequilibrium is not constant and increases in moisture disequilibrium can be a more efficient way of increasing surface latent heat flux than near-surface wind speed (Jaimes et al., 2021).

As shown in Figure A.1, the decay of a mature tropical cyclone due to a cold wake or interaction with a cold-core eddy can be understood with the same set of processes, but with the tendencies reversed. Again, although one might expect a weakening of boundary-layer convergence and an increase in the radius of forced ascent, one cannot be sure, due to the nonlinear nature of boundary-layer dynamics. In the case of weakening boundary-layer convergence, a negative feedback may occur between the surface latent heat flux and the near-surface wind speed. Note, however, that a negative feedback might also arise for fixed SST, if convergence in the boundary layer is initially strong and $\overline{\rho w}_{\mathrm{BL}}$ is greater than $\overline{\rho w}_{EW}$. In this case, there is an outflow above the boundary layer that spins down the boundary-layer flow (Kilroy et al., 2016; Smith et al., 2018).

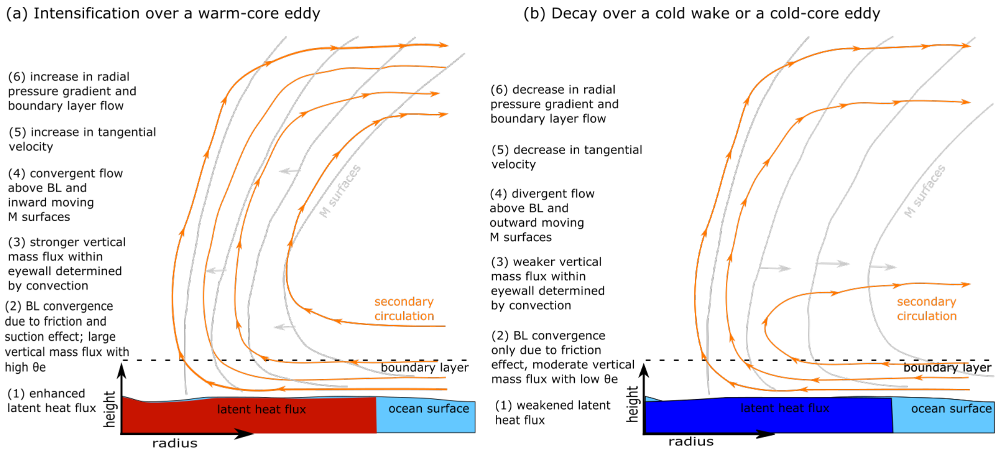
(a) Intensification over a warm-core eddy
(6) increase in radial pressure gradient and boundary layer flow
(5) increase in tangential velocity
(4) convergent flow above BL and inward moving M surfaces
(3) stronger vertical mass flux within eyewall determined by convection
(2) BL convergence due to friction and suction effect; large vertical mass flux with high θe
(1) enhanced latent heat flux
M surfaces
secondary circulation
boundary layer
latent heat flux
ocean surface
height
radius
(b) Decay over a cold wake or a cold-core eddy
(6) decrease in radial pressure gradient and boundary layer flow
(5) decrease in tangential velocity
(4) divergent flow above BL and outward moving M surfaces
(3) weaker vertical mass flux within eyewall determined by convection
(2) BL convergence only due to friction effect, moderate vertical mass flux with low θe
(1) weakened latent heat flux
M surfaces
secondary circulation
boundary layer
latent heat flux
ocean surface
height
radius

Figure A.1: Schematic of the processes outlined in the conceptual framework in the case of (a) intensification over a warm-core eddy and (b) decay over a cold wake.

A.5 TROPICAL CYCLONE IN THE ICON SIMULATION

The tropical cyclone simulated in the coupled ICON model is shown in Figure A.2. It forms in the North Atlantic in the last 10 days of the 40-day simulation, between August 31 and September 9, 2013. These dates coincide with the historical North Atlantic tropical storm *Gabrielle*. In our simulation, the tropical cyclone intensity is considerably larger than in *Gabrielle* and follows a trajectory that runs much closer to the eastern seaboard of North America, as seen in Figure A.2. However, the synoptic forecasting skill of the model is marginal by day 30, and the synoptic ocean eddy field does not represent the ocean eddy field from 2013. Therefore, the simulated tropical cyclone cannot be expected to correspond to any historical tropical cyclone, including tropical storm *Gabrielle*.

In this section, we start with a brief overview of the tropical cyclone in the ICON simulation, including its intensity, structure, and environment. (Section A.5.1). Then we investigate the change in tropical cyclone intensity with the help of the conceptual framework outlined in Section A.4, focusing on the period where the tropical cyclone generates a cold wake and encounters a warm-core eddy. Our investigation consists of three steps. Firstly, we examine the role of the ocean in the surface latent heat flux supplied to the tropical cyclone. Here, we analyse the pre-storm upper-ocean structure (Section A.5.2) and discuss the coupling between the sea-surface cooling and the surface latent heat flux (Section A.5.3). Secondly, we focus on the atmospheric processes that are listed in the conceptual framework, including the thermodynamics of the ascending boundary-layer air (Section A.5.4), the vertical mass fluxes in the eyewall updraught (Section A.5.5), the secondary circulation in and above the boundary layer (Section A.5.6), and the advection of absolute angular momentum (M) at the top of the boundary layer (Section A.5.7). Finally, we draw on our analysis of both the ocean and the atmosphere to discuss the combined importance of ocean-atmosphere coupling and boundary-layer dynamics for the change in tropical cyclone intensity (Section A.5.8).

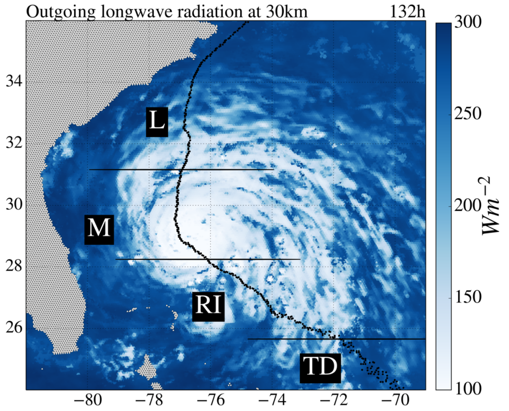

Figure A.2: The outgoing longwave radiation at a height of 30 km, corresponding to the model top, is shown for 132 hours after 31/08/2013 00:00 UTC. The tropical cyclone traverses along the trajectory (dotted line) to higher latitudes. The partitions between stages (see Table 1) are indicated with solid horizontal lines. Here, the data is plotted on the original triangular grid, and land cells are masked out in gray.

A.5.1 *Overview of the simulated tropical cyclone*

A time series of tropical cyclone intensity is shown in Figure A.3. Two conventional measures of tropical cyclone intensity are displayed: the minimum mean sea-level pressure at the centre, P_{min}, and the maximum 10-m wind speed, V_{max}. Between 92 and 116 hours the tropical cyclone undergoes rapid intensification, defined as an increase in V_{max} of more than 15.4 ms^{-1} within 24 hours, into a category 3 hurricane with a peak V_{max} of 52 ms^{-1} and a P_{min} of 933 hPa (Kaplan et al., 2003). In the mature phase, V_{max} initially decreases between 116 and 152 hours: gradually until 136 hours, and then more dramatically up to 152 hours. During this period, the tropical cyclone weakens into a category 2 hurricane. In the final part of the mature phase, the tropical cyclone reintensifies by around 6 ms^{-1} between 152 and 166 hours.

We subdivide the tropical cyclone intensity time series into several phases listed in Table 1. We define the tropical depression phase to be the initial phase before the radius of gales is well defined. The radius of gales refers to the radius at which the wind speed crosses a threshold of 17 ms^{-1}. The tropical depression phase (TD) is followed by the rapid intensification phase (RI), where the radius of gales is well defined. Since the radius of gales is computed from an azimuthal mean, unlike V_{max}, the start of the rapid intensification phase does not exactly coincide with V_{max} exceeding 17 ms^{-1}. We define the subsequent mature phase to start when V_{max} reaches its peak value at 116 hours and to end at 172

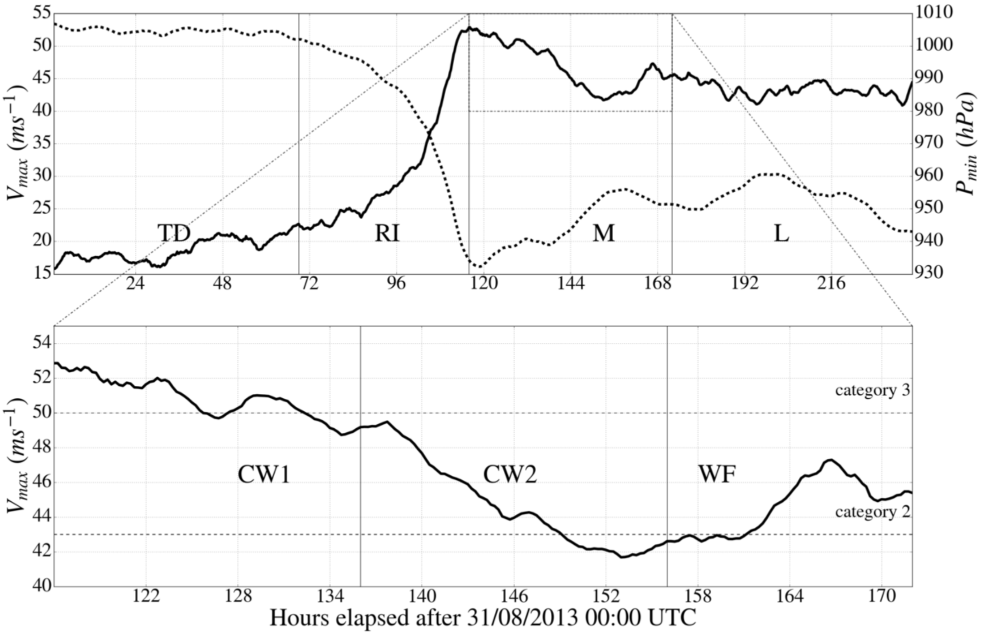

Figure A.3: Top: The 3-hour running mean of the maximum near-surface wind speed, V_{max}, and the minimum sea level pressure, P_{min}, are denoted by a solid line and a dashed line, respectively. Bottom: A blow-up of the maximum near surface wind speed in the mature phase (M). A description of the abbreviations is provided in Table 1.

hours, when the tropical cyclone makes landfall. The mature phase is further subdivided into three subphases. During the cold wake 1 (CW1) phase, the tropical cyclone gradually decays. The tropical cyclone experiences a more rapid decay in the cold wake 2 (CW2) phase. Finally, in the warm feature (WF) phase, the tropical cyclone reintensifies.

Figure A.4 displays horizontal snapshots of vertical velocity and tangential velocity taken at a height of 5 km. The first two panels show the development of a symmetric eyewall updraught during RI (Figure A.4 (a), (b)). The transition from an asymmetric structure to a symmetric eyewall updraught is characteristic of the transition into a mature tropical cyclone (Houze, 2010). The decreasing vertical velocity in the eyewall updraught region during CW1 and CW2 indicates weakening deep convection (Figure A.4 (b) - (d)). Regions of strong convection remain, but these are found away from the eyewall updraught at radii beyond 100 km, where the 30-ms^{-1} tangential velocity contour is located. Towards the end of CW2, convection in the eyewall updraught begins to strengthen, with a substantial increase in the vertical velocity visible during WF (Figure A.4 (e), (f)).

The azimuthal-mean structure of the absolute angular momentum (M) surfaces and the secondary circulation is shown in Figure A.5. As is typical of tropical cyclones, the M-surfaces slope outwards with height and generally have a positive radial gradient. A region of strong inflow is found at the sea surface and a region of outflow is located in the upper troposphere. Connecting the inflow and outflow regions is a region of updraught at small radii that extends vertically throughout the depth of the troposphere. As the secondary circulation strengthens and the eyewall updraught develops during RI, the M-surfaces

Stage	Time (hours after 31/08/2013 00:00 UTC)	Intensity trend	Maximum near-surface wind speed (m/s)
Tropical Depression (TD)	0-69	Nascent tropical cyclone strengthens into tropical storm	15-22
Rapid Intensification (RI)	69-116	Sustained intensification, including instance of rapid intensification	22-52
Mature (M): Cold Wake 1 (CW1)	116-136	Gradual decay	49-52
Mature (M): Cold Wake 2 (CW2)	136-156	Accelerated decay	42-50
Mature (M): Warm Feature (WF)	156-172	Reintensification	42-48
Landfall and Recurvature (L)	172-240	Steady	42-45

Table 1: A list of phases that the simulated tropical cyclone undergoes during its life cycle.

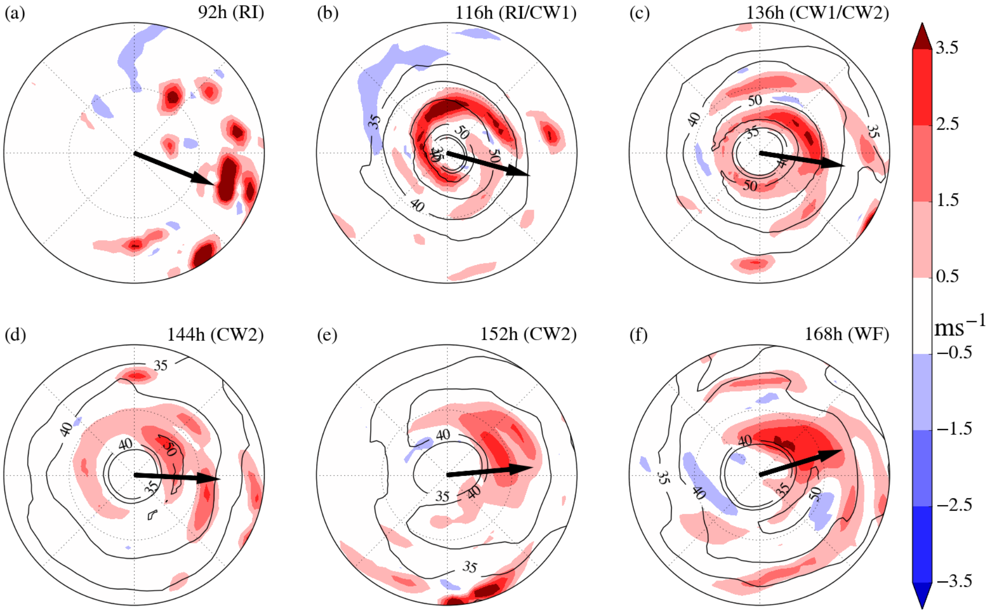

Figure A.4: Horizontal snapshots of vertical velocity (blue and red shading) and tangential velocity (black contours) at a height of 5 km at (a) 92 hours, (b) 116 hours, (c) 136 hours, (d) 144 hours, (e) 152 hours and (f) 168 hours after 31/08/2013 00:00 UTC. For the tangential velocity, contours are shown for 35 ms^{-1}, 40 ms^{-1} and 50 ms^{-1}. The direction of the vertical wind shear, as defined by Kaplan et al. (2003), is indicated by the arrow. Radial grid lines are displayed for 50 km and 100 km.

move radially inwards, indicating a strengthening of the primary circulation (Figure A.5 (a), (b)). During the subsequent weakening of the eyewall updraught during CW1 and CW2, the eyewall updraught moves radially outwards (Figure A.5 (b) - (e)). Simultaneously, the primary circulation strengthens at larger radii, but weakens at smaller radii, where the M-surfaces move outwards. As the eyewall updraught strengthens during WF, it moves radially inwards (Figure A.5 (e), (f)). The primary circulation strengthens throughout the tropical cyclone, which is evident from the inward shift of the M-surfaces.

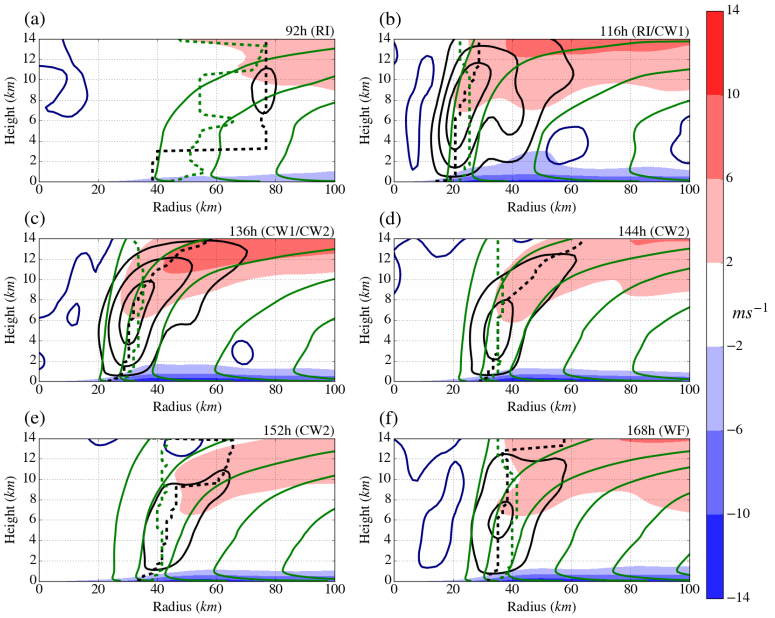

Figure A.5: Azimuthal-mean of flow in tropical cyclone is shown as a 3-hour running mean for 92, 116, 136, 144, 152 and 168 hours after 31/08/2018 00:00 UTC. Contours of the updraught are shown by the solid black lines and correspond to (0.5, 1.0, 1.5) ms^{-1}. The single blue contour shows regions of downdraught. Angular momentum contours are displayed as solid green lines and increase from the centre outwards, corresponding to (1.0, 1.5, 2.0, 2.5, 3.0) $\times$ 10^6 m^{2}s^{-1}. The blue and red shading indicates the inflow and outflow, respectively. The shading corresponds to, from light to dark, (2, 6, 10, 14) ms^{-1}. The radius of maximum vertical velocity is indicated by the black dashed line and the radius of maximum tangential velocity is shown as a green dashed line.

Figure A.6 shows the height of the boundary layer, h, diagnosed for the ICON simulation. Here, h is defined as the height at which the maximum tangential velocity in the tropical cyclone is located (Bryan et al., 2009). During RI, h initially decreases from 1200 to 600 m. During the remainder of RI and the subsequent mature phase, h fluctuates in a range between 600 and 800 m. The vertical level in the ICON model that corresponds most closely to the upper boundary of h in Figure A.6 is located at a height of 780 m. While the boundary layer height is in reality a function of radius (Zhang et al., 2011), we take h to be a constant 780 m with a view to keeping the subsequent analysis simple.

Figure A.7 (a) shows the time series of the surface latent heat flux averaged over an annulus centred on the tropical cyclone centre, which is located at the surface grid cell with the lowest mean sea-level pressure. The annulus has an inner and outer radius that are respectively 10 km less than and 10 km greater than the radius of maximum near-surface wind speed. The surface latent heat flux rises and peaks toward the end of RI at 820 Wm^{-2}. During CW1, the surface latent heat flux reaches a local minimum of around 410 Wm^{-2} and then peaks again at 540 Wm^{-2}. Subsequently, the surface latent heat flux

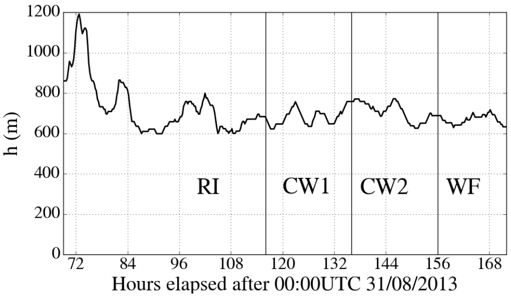

Figure A.6: Time series of the boundary layer height, h, displayed as a 3-hour running mean.

decreases continuously into CW2 and reaches a global minimum of 110 Wm⁻². This global minimum is followed by an increase during the latter stage of CW2 and WF, where the surface latent heat flux peaks at 730 Wm⁻².

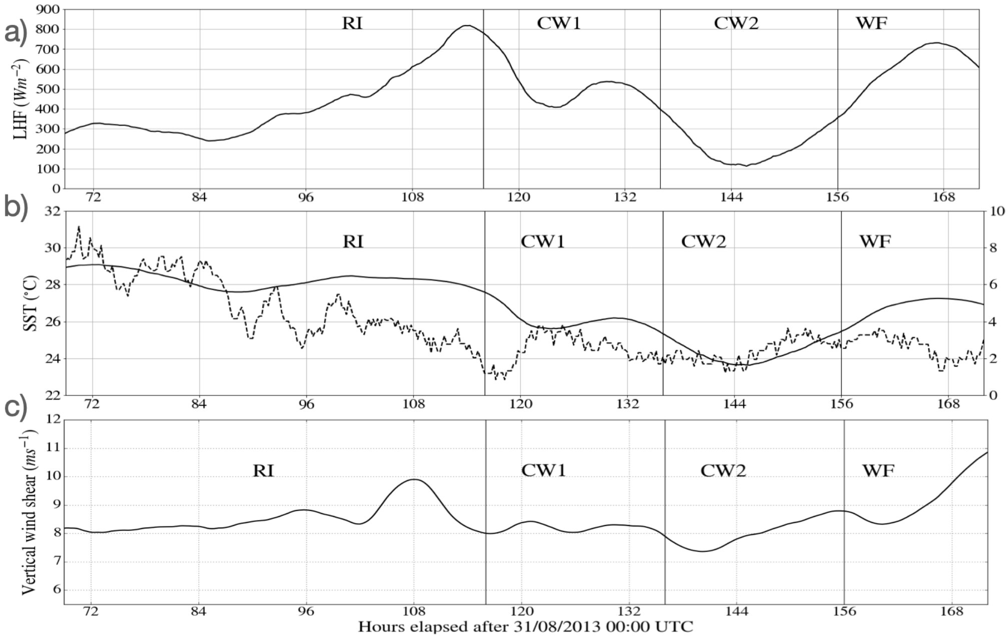

Figure A.7: Time series of (a) surface latent heat flux (LHF), (b) SST (solid line) and translational speed (V_{trans}) and (c) vertical wind shear. All variables are displayed as 3-hour running means. LHF and SST are averaged over an annulus which extends 10 km inside and 10 km outside the radius of maximum near-surface wind speed. The vertical wind shear is computed from the average horizontal wind vector over a circular anulus spanning a radial interval between 200 km and 800 km.

A time series of SST is plotted in Figure A.7 (b). Here, SST is averaged over the same time-varying annulus as for the surface latent heat flux. During RI, SST fluctuates between 29.0 °C and 27.3 °C. In the mature phase, SST experiences two minima and maxima that coincide with the respective minima and maxima of the surface latent heat flux. During CW1, a local minimum of 25.6 °C is followed by a local maximum of 26.2 °C. Subsequently, SST reaches a global minimum of 23.6 °C during CW2, before recovering and peaking at 27.2 °C in WF.

The time series of the translational speed, V_{trans}, is also shown in Figure A.7 (b). A positive correlation and time lag are evident between SST and V_{trans}. Initially, V_{trans} shows a clear downward trend, decreasing from 9 ms^{-1} during RI. During the mature phase, a positive correlation and time lag between SST and V_{trans} are evident from a similar set of minima and maxima in V_{trans}. The first minimum at 1 ms^{-1} occurs at the start of CW1 and is quickly followed by a maximum close to 4 ms^{-1}. After this maximum, V_{trans} decreases steadily until 144 hours (CW2) to approximately 2 ms^{-1}. Subsequently, V_{trans} increases in the latter part of CW2 and then remains between 3 and 4 ms^{-1} until 160 hours (WF).

Figure A.7 (c) shows the vertical wind shear of the environment, which is defined as the difference between the average horizontal wind vectors on the 200- and 850-hPa surface computed for a radius between 200 and 800 km (Kaplan et al., 2003). The vertical wind shear remains fairly constant at around 8 ms^{-1} during CW1, CW2 and the initial stage of WF before increasing.

While the moderate to large vertical wind shear may reduce the maximum tropical cyclone intensity reached in RI (Wong et al., 2004), a constant vertical wind shear is unlikely to be responsible for the different decay rates in CW1 and CW2. Since increasing vertical wind shear is associated with decay, the reintensification during WF cannot be due to the concurrent increase in vertical wind shear.

Instead, the change in tropical cyclone intensity in the mature phase is strongly correlated to the changes in SST and surface latent heat flux. The decay during CW1 and CW2 occurs as the SST and surface latent heat flux drop, with a faster rate of decay during CW2 coinciding with lower SST and surface latent heat flux than in CW1. Similarly, the reintensification during the latter stage of CW2 and WF is accompanied by increasing SST and surface latent heat flux. There is also a time lag between the change in SST and surface latent heat flux and the intensity. The peak in intensity at the start of CW1 occurs two hours after the surface latent heat flux peaks. During CW2, the intensity only reaches its minimum value eight hours after both the SST and the surface latent heat flux do so.

A.5.2 *Upper-ocean structure and sea-surface cooling*

Figure A.8 (a) shows the pre-storm upper-ocean heat content, OHC, for the region traversed by the tropical cyclone in the mature phase (CW1, CW2, WF). Values of OHC are computed following Leipper et al. (1972), where OHC is defined as the deviation of the upper-ocean temperature from 26 °C integrated over all depths between the surface and the 26-°C isotherm. Physically, OHC can be interpreted as the anomalous heat content in the upper ocean where the temperature exceeds 26 °C. The pre-storm OHC does not exceed 40 kJ/cm^2 along the section of the trajectory traversed during CW1 and CW2. However, the pre-storm OHC is much larger for the WF section of the trajectory and reaches a maximum between 80 and 90 kJ/cm^2.

The higher pre-storm OHC for the WF section of the trajectory corresponds to a warm-core eddy. Situated at 30.5° N -77° E, the warm-core eddy lies directly on the trajectory of the tropical cyclone. The surface current reveals an anticyclonic signature that is char-

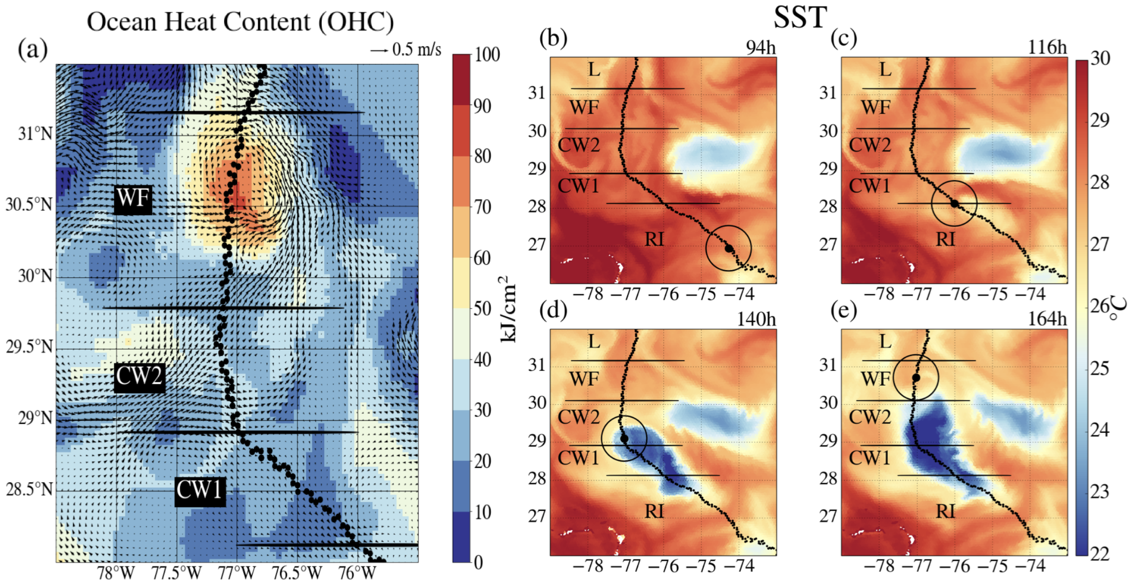

Figure A.8: Snapshots of (a) pre-storm ocean heat content (OHC) at 0 hours and SST at (b) 94 hours (RI), (c) 116 hours (RI/CW1), (d) 140 hours (CW2) and (e) 164 hours (WF) after 31/08/2013 00:00 UTC. The horizontal surface current is shown in (a) by the black arrows. The tropical cyclone traverses northwards along the trajectory indicated by the dotted line in all the snapshots. The position of the tropical cyclone is shown by the black circle. The partitions between the stages (see Table 1) are indicated with solid horizontal lines. The SST snapshots are plotted on the original triangular grid.

acteristic of warm-core eddies (Figure A.8 (a)). Although the warm-core eddy is clearly visible from the pre-storm OHC and the sea-surface height (not shown), it is concealed in the pre-storm SST field shown in Figure A.8 (b).

The presence of this concealed, subsurface warm-core eddy reduces the sea-surface cooling locally (Figure A.8 (b) - (e)). The reduced sea-surface cooling is consistent with weaker entrainment cooling in a deeper mixed layer (not shown), where less wind-driven kinetic energy is available for turbulent mixing because more energy is lost to the thermocline via internal near-inertial waves (Gill, 1984; Jaimes et al., 2009b; Linden, 1975). The higher SST associated with the reduced sea-surface cooling over the warm-core eddy contrasts with the lower SST trailing behind the tropical cyclone (Figure A.8 (e)). The lower SST is typical of a cold wake associated with tropical cyclones. In agreement with previous work, the sea-surface cooling is stronger on the right-hand side of the trajectory, and the strongest sea surface cooling is found in the rear part of the cold wake away from the inner core, which is typical for tropical cyclones in the North Atlantic (Chang et al., 1978; Cione et al., 2003; Price, 1981). While the effect of warm-core eddies on the surface latent heat flux and change in intensity has been studied before, this is the first study to examine the influence of a warm-core eddy at depth on the kinematic structure of the boundary layer with a fully three-dimensional eddy-resolving simulation.

A.5.3 *Influence of sea-surface cooling on surface latent heat flux*

Figure A.9 shows the azimuthal-mean SST, moisture disequilibrium at the air-sea interface, surface latent heat flux, and near-surface wind speed. During RI, the SST reflects the ambient SST and changes over time, while remaining relatively uniform in the radial direction (Figure A.9 (a)). A cold wake signal is evident during CW1 from the lower SST and the positive radial gradient in SST at 120 hours. This cold-wake signal is superseded by an increase in SST and then a second, more prolonged cold-wake signal. The second cold-wake signal displays stronger sea-surface cooling during CW2 than in CW1; note the lower SST and the larger positive radial gradient in SST. The variation in the sea-surface cooling may be due to the change in the translational speed (Chang et al., 1978, 1979; Price, 1981). The time series in Figure A.7 (b) shows that the sea-surface cooling during both CW1 and CW2 follows a decrease in V_{trans}. The stronger sea surface cooling in CW2 may also be related to the increasing size of the tropical cyclone (not shown), with a radius of gales increasing from 120 km at the start of CW1 to 250 km at the beginning of CW2 (Pun et al., 2018). During WF, the high SST associated with the subsurface warm-core eddy contrasts with the low SST in CW1 and CW2 (Figure A.9 (a)).

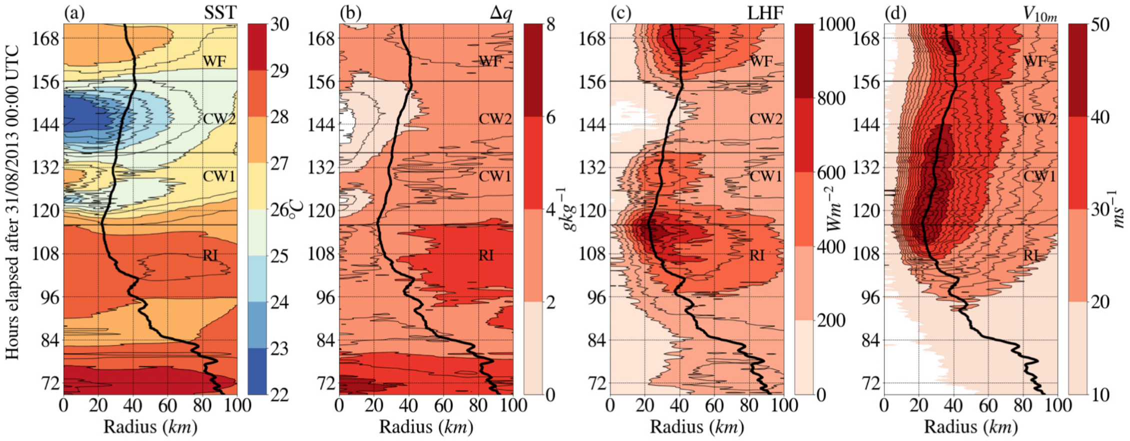

Figure A.9: Hovmöller plots of azimuthally averaged (a) SST, (b) moisture disequilibrium at the air-sea interface, (c) surface latent heat flux and (d) near-surface wind speed for the innermost 100 km. The spacing of the thin black contours for each of the plots are (a) 1 °C, (b) 1 gkg^{-1}, (c), 100 Wm^{-2} and (d) 2 ms^{-1}. The 3-hour running mean of the radius of maximum near-surface wind speed, $R_{surfmax}$, is shown as a thick solid black line in all four plots.

The decrease in the moisture disequilibrium at the air-sea interface, Δq, during CW1 and CW2 is positively correlated to the decreasing SST (Figure A.9 (a), (b)). This correlation is evident from the positive radial gradient seen during CW2 for both SST and Δq inside a 50 km radius. Similarly, the increasing Δq is closely correlated to the increasing SST during the latter stage of CW2 and WF. The change in Δq is reflected by the decrease and increase in the surface latent heat flux during the mature phase (Figure A.9 (b), (c)). The pronounced change in surface latent heat flux during the mature phase is consistent with the high sensitivity of surface latent heat flux to SST in regions with large near-surface wind speed (Cione et al., 2003).

The correlation between the changes in the surface latent heat flux and the near-surface wind speed, V_{10m}, is weaker during the mature phase (CW1, CW2, WF) than in RI (Figure A.9 (c), (d)). During RI, the increase in the surface latent flux at the radius of maximum near-surface wind speed, $R_{surfmax}$, is consistent with the simultaneous increase in V_{10m}. At the end of RI, the peak in surface latent heat flux at $R_{surfmax}$ coincides temporally and spatially with the peak in V_{10m}. At larger radii, the change in the surface latent flux during RI is influenced by changes in Δq. Between 96 and 120 hours, the surface latent heat flux exceeds 400 Wm^{-2} over a region extending from $R_{surfmax}$ out to 100 km. The radial extent of the 400 Wm^{-2} contour decreases substantially in the latter part of CW1. This decrease is consistent with the simultaneous decrease in SST and Δq, rather than the local increase in V_{10m} seen from the expanding contours in Figure A.9 (d). While the maximum surface latent heat flux occurs at $R_{surfmax}$ during CW1, the same is not true for CW2. Instead, the maximum surface latent heat flux during CW2 occurs at a radius larger than $R_{surfmax}$, because the surface latent heat flux is dominated by the decrease in SST and Δq. During the latter stage of CW2 and WF, the sudden increase in surface latent heat flux from $R_{surfmax}$ out to 100 km cannot be explained by a sudden local increase in V_{10m}, but rather by the jump in SST and Δq. More generally, this period of reintensification is an example of increasing SST and Δq being an effective way to increase the surface latent heat flux in a warm-ocean regime (Jaimes et al., 2021). The foregoing analysis shows that the change in the areal-averaged surface latent heat flux in Figure A.7 (a) is dominated by changes in SST and Δq in the mature phase.

A.5.4 *Equivalent potential temperature of ascending boundary layer air*

The changes in the surface latent heat flux lead to changes in the equivalent potential temperature, θ_e, in the boundary layer, which in turn determine the buoyancy of air parcels there. Only air parcels with positive buoyancy at the top of the boundary layer are able to rise into the eyewall updraught, with a vertical velocity that depends on the magnitude of the buoyancy. Figure A.10 shows radius-height snapshots and a Hovmöller plot at the boundary-layer top for the azimuthal-mean equivalent potential temperature, $\overline{\theta_e}$, and the vertical velocity. As the tropical cyclone intensifies and becomes increasingly axisymmetric during RI, the radial gradient of $\overline{\theta_e}$ becomes negative throughout the innermost 100 km (Figure A.10 (a), (b), (g)). The largest negative radial gradient is found inside a 20 km radius, where the $\overline{\theta_e}$ contours become increasingly vertical throughout the depth of the boundary layer. During CW1, the decreasing average surface latent heat flux is accompanied by a decrease in $\overline{\theta_e}$ inside a 20 km radius: note how the dark red shading in the inner core disappears and the negative radial gradient decreases (Figure A.10 (b), (c), (g)). In contrast, $\overline{\theta_e}$ continues to increase between a 20 and 40 km radius throughout the depth of the boundary layer. At radii beyond 40 km, the $\overline{\theta_e}$ contours are not vertical and the boundary layer is not well mixed. During CW2, the decrease in the average surface latent heat flux to a global minimum is accompanied by a substantial drop in $\overline{\theta_e}$ inside a 40 km radius throughout the depth of the boundary layer (Figure A.10 (c), (d), (g)). Beyond a 40 km radius, $\overline{\theta_e}$ decreases in the upper boundary layer, as shown by the descending dark blue region of low $\overline{\theta_e}$. Conversely, the increase in average surface latent heat flux during the latter stage of CW2 and WF is accompanied by an increase in $\overline{\theta_e}$ inside a 40 km radius throughout the depth of the boundary layer. At radii beyond 40 km, $\overline{\theta_e}$ continues to decrease (Figure A.10 ((d) - (g)).

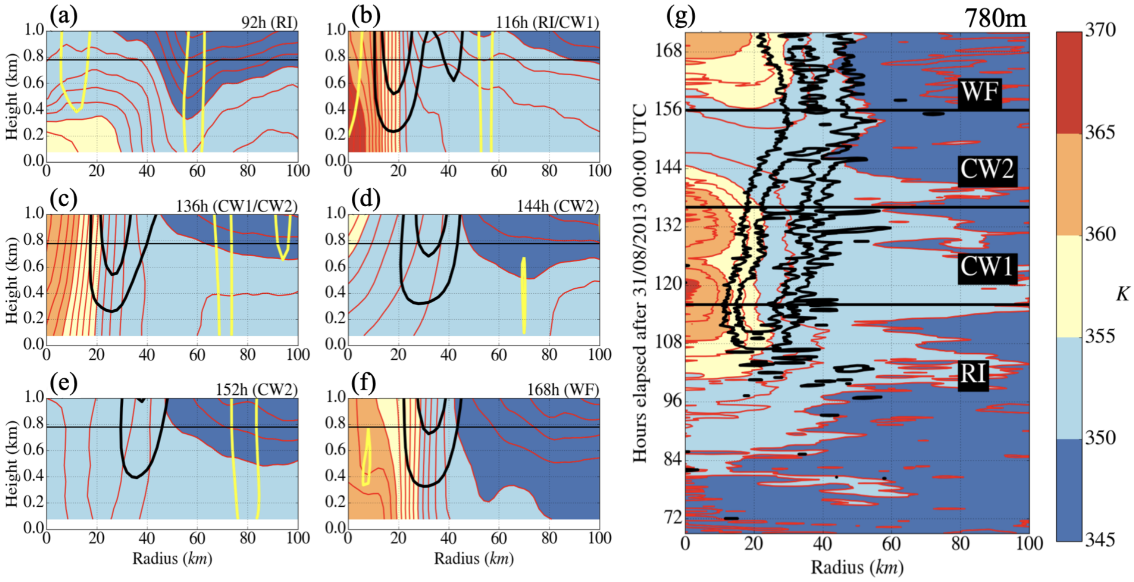

Figure A.10: The azimuthal-mean of equivalent potential temperature, $\overline{\theta_e}$, and vertical velocity are displayed as ((a) - (f)) six instantaneous, radius-height snapshots and (g) a Hovmöller plot at the boundary layer top at 780 m. The vertical snapshots are shown for (a) 92 hours, (b) 116 hours, (c) 136 hours, (d) 144 hours, (e) 152 hours and (e) 168 hours after 31/08/2013 00:00 UTC. The horizontal black lines ((a) - (f)) indicates the top of the boundary layer at 780 m. Note that the colorbar and contour values are identical for both the vertical snapshots and the Hovmöller plot. The spacing between the red $\overline{\theta_e}$ contours is 1 K in panels (a) - (f) and 2.5 K in panel (g). The thick black contours ((a) - (g)) correspond to an updraught of 0.25 ms^{-1} and 0.5 ms^{-1}. The bright yellow contour in panels (a) - (f) indicates the regions of downdraught (zero vertical velocity). For visual clarity the yellow contour is not included in panel (g).

Figure A.11 shows the same $\overline{\theta_e}$ in Figure A.10 (g) averaged over all radii where the vertical velocity exceeds 0.25 ms^{-1}, $\langle\overline{\theta_e}\rangle_{up}$, as well as the mean radius of this updraught region, $\langle R\rangle_{up}$. During CW1, $\langle\overline{\theta_e}\rangle_{up}$ decreases on account of a negative radial gradient in $\overline{\theta_e}$ and an increasing $\langle R\rangle_{up}$. The transient decrease in $\overline{\theta_e}$ inside a 20 km radius does not have a large effect on $\langle\overline{\theta_e}\rangle_{up}$, because the corresponding updraught approximately extends from 15- to 40 km radius. During CW2, $\langle\overline{\theta_e}\rangle_{up}$ decreases faster than in CW1 on account of both an increasing $\langle R\rangle_{up}$ and the local decrease in $\overline{\theta_e}$ inside a 40 km radius. Conversely, $\langle\overline{\theta_e}\rangle_{up}$ increases during the latter stage of CW2 and WF, due to both the the local increase in $\overline{\theta_e}$ inside a 40 km radius and, from the end of CW2 onwards, a decreasing $\langle R\rangle_{up}$.

Besides decreasing surface latent heat flux, vortex-tilt induced downdraughts in a large vertical-wind-shear environment can bring low-θ_e air into the boundary layer at radii beyond the eyewall updraught and reduce θ_e there (Molinari et al., 2013; Wadler et al.,

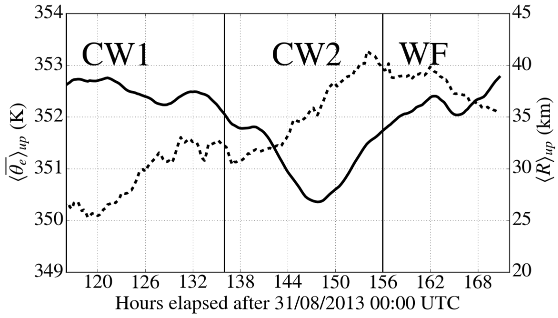

Figure A.11: Time series of the azimuthal-mean equivalent potential temperature at 780 m averaged over all radii where vertical velocity exceeds 0.25 ms^{-1}, $\langle\overline{\theta_e}\rangle_{up}$, and the mean updraught radius where the vertical velocity exceeds 0.25 ms^{-1}, $\langle R\rangle_{up}$. Both variables are shown as a 3-hour running mean.

2018; Zhang et al., 2017a). Riemer et al. (2010) show that the pattern of anomalously low-θ_e air is inherently asymmetric and that the downward flux of low-θ_e air increases with increasing vertical wind shear and decreasing intensity. To quantify the flushing of low-θ_e air into the boundary layer, Riemer et al. (ibid.) examine the downward flux of θ_e, DFX, which they define as,

$$\text{DFX} = w_{-}\theta_e', \tag{A.2}$$

where w_{-} is the vertical velocity in the downdraught region and θ_e' is the deviation of the local θ_e from the azimuthal mean, $\overline{\theta_e}$. Regions of downdraught with anomalously low θ_e are positive. Note that regions of updraught with anomalously high θ_e will also yield positive values of DFX.

Figure A.12 shows the DFX and the vertical velocity at the top of the boundary layer at 780 m[2] height. The positive values of DFX are found mainly in the eyewall updraught region, corresponding to ascending air parcels with anomalously high θ_e. While positive DFX values in the downdraught regions widely exceed 0.5 Ks^{-1} in Riemer et al. (ibid.) for a comparable wind shear of 10 ms^{-1}, they are weaker than 0.5 Ks^{-1} in Figure A.12, with the exception of Figure A.12 (a) at 92 hours.

The small downward flux of low-θ_e air suggests that the flushing of low-θ_e is less important for the decrease in $\langle\overline{\theta_e}\rangle_{up}$ during CW1 and CW2 than the change in surface latent heat fluxes. The low $\overline{\theta_e}$ contours that descend into the boundary layer (Figure A.10 (c)-(f)) are instead likely to be due due to drier environmental air as the tropical cyclone moves to higher latitudes (not shown).

The foregoing analysis points to an important role played by the changes in the surface latent heat flux in determining the accompanying changes in $\overline{\theta_e}$. Both the changes in $\overline{\theta_e}$ and the mean radius of the boundary-layer updraught determine the changes in buoyancy of ascending air parcels at the top of the boundary layer, which is reflected in $\langle\overline{\theta_e}\rangle_{up}$.

---

[2] Note that Riemer et al. (2010) calculate the DFX at the top of the inflow layer at 1.5 km, and not at the top of the boundary layer.

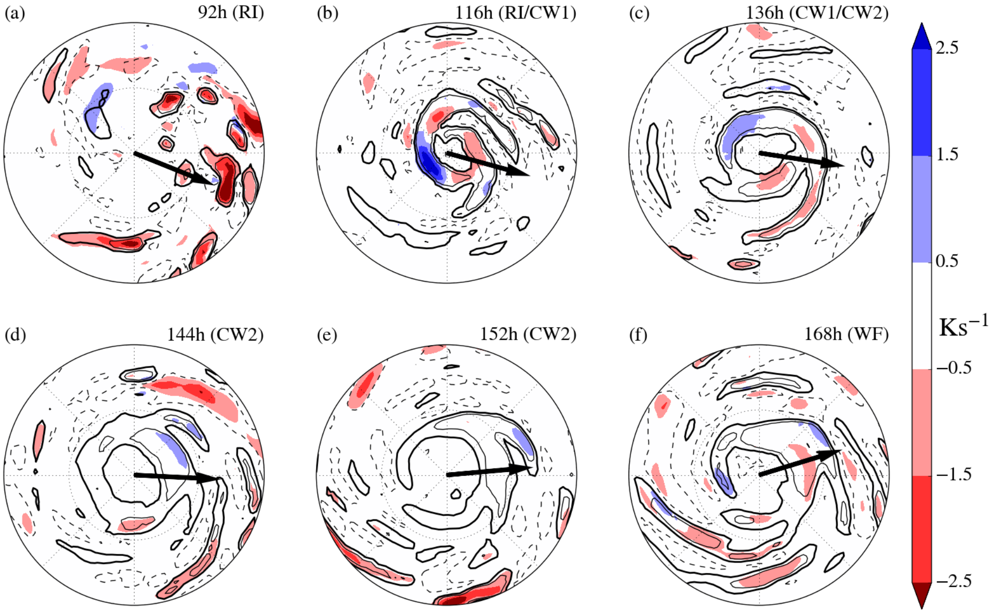

Figure A.12: Instantaneous horizontal snapshots of the downward flux of θ_e', DFX, (blue and red shading) and vertical velocity (black contours) at a height of 780 m at (a) 92 hours, (b) 116 hours, (c) 136 hours, (d) 144 hours, (e) 152 hours and (f) 168 hours after 31/08/2013 00:00 UTC. Contours are displayed for a vertical velocity of -0.1 ms^{-1} (dashed), 0.25 ms^{-1} (thick), and 0.5 ms^{-1} (thin). The direction of the vertical wind shear is indicated by the arrow. Radial grid lines are displayed for 50 km and 100 km.

A.5.5 *Vertical mass flux*

While the equivalent potential temperature of the air parcels in the boundary layer determines their buoyancy, the ability of the eyewall updraught to accept ascending boundary-layer air depends on the difference between the vertical mass flux within the eyewall updraught and its base at the top of the boundary layer. Figure A.13 displays the vertical mass flux averaged over radii between zero and 60 km for heights of 780 m, $\overline{\rho w}_{780\mathrm{m}}$, and 5 km, $\overline{\rho w}_{5\mathrm{km}}$, respectively. The eyewall updraught at 5 km height lies inside a 60 km radius, as shown by the 0.5 ms^{-1} contour in Figure A.5. During RI, $\overline{\rho w}_{780\mathrm{m}}$ and $\overline{\rho w}_{5\mathrm{km}}$ increase. The increasing gap between $\overline{\rho w}_{780\mathrm{m}}$ and $\overline{\rho w}_{5\mathrm{km}}$ shows that the strengthening convection in the eyewall updraught is increasingly able to accept the vertical mass flux from the boundary layer. During CW1, $\overline{\rho w}_{780\mathrm{m}}$ and $\overline{\rho w}_{5\mathrm{km}}$ remain relatively constant. During CW2, $\overline{\rho w}_{5\mathrm{km}}$ falls rapidly at first and then continues to decrease more gradually. A similar rapid fall is not seen for $\overline{\rho w}_{780\mathrm{m}}$, which decreases gradually throughout CW2. This discrepancy shows that while deep convection weakens substantially in the eyewall updraught, boundary-layer convergence remains relatively strong. Consequently, the deep convection in the eyewall updraught is less able to ventilate the vertical mass flux from the boundary layer. As a result, there is substantial weakening of the inflow into the eyewall updraught from above the boundary layer, as seen in Section A.5.6. During the latter stage of CW2 and WF, $\overline{\rho w}_{780\mathrm{m}}$ and $\overline{\rho w}_{5\mathrm{km}}$ experience a sharp increase and peak before decreasing again, which is consistent with a substantial strengthening of deep convection (Figure A.4 (e), (f)).

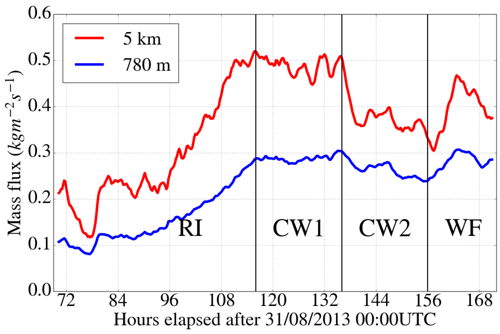

Figure A.13: Upward mass fluxes averaged within a radius of 60 km are shown as a 3-hour running mean for a height of 780 m (blue) and 5 km (red).

A.5.6 *Updraught and inflow*

The difference between the vertical mass flux in the eyewall updraught at around 5 km height, where the vertical velocities are largest, and at its base at the top of the boundary layer determines the strength of the radial inflow above the boundary layer. The azimuthal-mean inflow and updraught for the lowermost 4 km is displayed in Figure A.14. During CW1 and CW2, the inflow strengthens between 92 and 116 hours (Figure A.14 (a), (b)). During the mature phase, the inflows above and below 1 km do not weaken in unison. Comparing the 1 ms^{-1} and 2 ms^{-1} contours in Figure A.14 (b) and (c) reveals a weakening of the inflow inside a 100 km radius during CW1. In contrast, the 5 and 10 ms^{-1} contours show that the inflow in the lowermost 1 km remains relatively constant. The inflow also reflects the radially outward movement of the eyewall updraught. From Figure A.14 (c) and (d), it is evident that the inflow inside a 100 km radius continues to weaken above 1 km in CW2, while the inflow below 1 km remains relatively constant.

As the eyewall moves radially inwards during WF, the inflow strengthens both above and below 1 km within the innermost 100 km, as shown by the 1, 5, and 10 ms^{-1} contours (Figure A.14 (e), (f)). The strengthening inflow indicated by the 1 ms^{-1} contour coincides with a second updraught region that is weaker than the primary updraught region and is located between a radius of 50 km and 100 km. This second updraught region is associated with a spiral band rather than a secondary eyewall, as seen from the plane-view plot of vertical velocity in Figure A.4 (e) and Figure A.4 (f).

A.5.7 *Absolute angular momentum*

The changing radial inflow in a vertical layer above the boundary layer leads to changes in the radial advection of absolute angular momentum (M) surfaces. Figure A.15 displays a Hovmöller plot of the M-surfaces and the vertical velocity at the top of the boundary

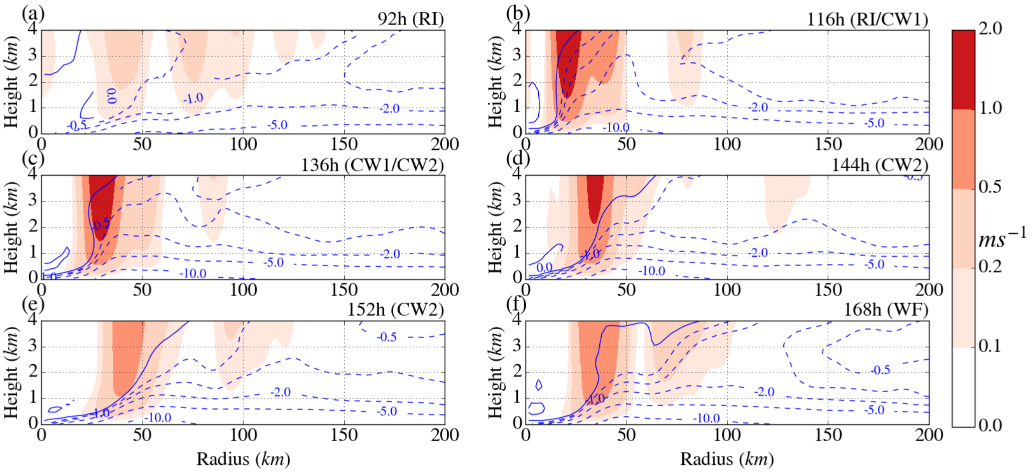

Figure A.14: Azimuthal-mean of secondary circulation shown as a 3-hour running mean for 92, 116, 136, 144, 152 and 168 hours after 31/08/2018 00:00 UTC. The red shading indicates the magnitude of vertical velocity. Inflow contours are displayed as blue lines, corresponding to (0.0,0.5,1.0,2.0,5.0,10.0) ms^{-1}.

layer. During RI, the M contours move radially inwards over time for all radii inside 100 km. During CW1, the M contours inside the updraught region (characterised by a vertical velocity greater than 0.25 ms^{-1}) move radially outwards, as seen from the 1 × 10^{6} m^{2}s^{-1} and 1.5 × 10^{6} m^{2}s^{-1} contours. The M contours at larger radii continue to move radially inwards in the intervening period. During CW2, in contrast, all the displayed M contours move outwards over time. Although the radial flow beyond the eyewall updraught region is directed inwards during CW2, the vertical advection of low M from below leads to the displayed M contours moving outwards. During the latter stage of CW2 and WF, the displayed M contours move inwards inside a radius of 100 km.

A.5.8 *Discussion*

The foregoing analysis allows us to understand the evolution of the azimuthal-mean structure and intensity of the tropical cyclone during the mature phase in terms of the conceptual framework outlined in Section A.4. In the following, we synthesise the foregoing analysis and discuss the change in azimuthal-mean structure and intensity separately for the initial period of decay, the latter period of decay, and the period of reintensification. Comparing and contrasting the three different periods offers an insight into the importance of boundary-layer dynamics and air-sea coupling. The schematic in Figure A.1 outlining the conceptual framework used for the preceding analysis may prove useful in the following discussion.

During CW1, the wind-stress-induced sea-surface cooling leads to a decrease in the SST averaged within the radius of maximum near-surface wind. The decrease in SST and the accompanying decrease in the moisture disequilibrium at the air-sea interface, Δq, dominate the overall decrease in the average surface latent heat flux within the same radius.

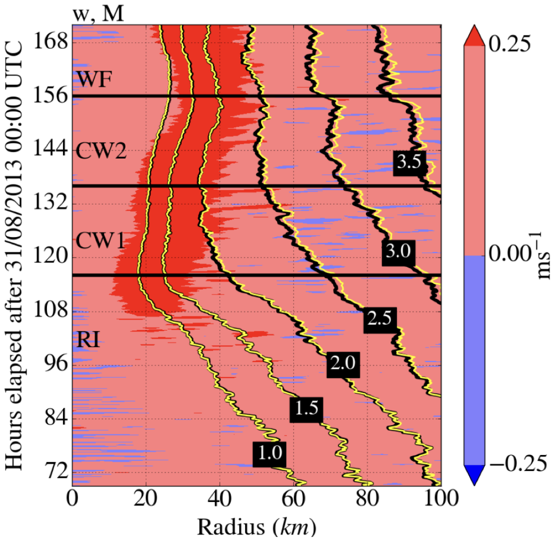

Figure A.15: Hovmöller plot of angular momentum (M) and vertical velocity. The M contours at a height of 780 m and 620 m are shown as black and yellow lines, respectively. The contours are displayed for (1.0, 1.5, 2.0, 2.5, 3.0, 3.5) × 10^6 m^2s^{-1}. The shading indicates the vertical velocity at 780 m according to the colorbar.

The average surface latent heat flux reaches a local minimum, which is accompanied by a transient decrease in the azimuthal-mean equivalent potential temperature at the top of the boundary layer, $\overline{\theta_e}$, inside a 20 km radius. However, the transient decrease in $\overline{\theta_e}$ does not have a large influence on the mean $\overline{\theta_e}$ of air ascending into the eyewall updraught at the top of the boundary layer that is characterised by vertical velocities exceeding 0.25 ms^{-1}, $\langle\overline{\theta_e}\rangle_{up}$. This is because the corresponding updraught region at the top of the boundary layer extends from 15-40 km radius. Hence, $\langle\overline{\theta_e}\rangle_{up}$ is not appreciably affected by the decrease in the average surface latent heat flux. During CW1, the mean radius of the eyewall updraught increases on account of nonlinear boundary-layer dynamics in the presence of the expanding outer circulation. As the mean radius of the updraught increases, $\langle\overline{\theta_e}\rangle_{up}$ decreases. The decreasing $\langle\overline{\theta_e}\rangle_{up}$ reduces the local buoyancy of air parcels in the eyewall updraught, which leads to a decrease in the vertical velocity in the eyewall updraught. While the vertical velocity decreases at a height of 5 km, which is in the middle troposphere, the average vertical mass flux remains steady[3] within a radius of 60 km, which includes the outward-moving eyewall updraught. Since the difference between the vertical mass flux of the eyewall updraught in the middle troposphere and at the base of the eyewall updraught remains large, the eyewall updraught is more than able to accept the ascending boundary-layer air and produce a strong radial inflow in a vertical layer above the boundary layer at radii beyond the eyewall updraught. In turn, the radial inflow draws absolute angular momentum (M) surfaces, leading to a local increase in the tangential wind speed. Because the tangential wind speed above the boundary layer remains in gradient-wind balance to a good approximation (not shown), the local increase in the tangential wind speed increases the local radial pressure gradient, which is transmitted essentially unchanged into the boundary layer. The increase in the radial pressure gradient in the boundary layer changes the net radial force in the boundary layer at radii beyond the eyewall updraught. As shown by Kilroy et al. (2016), the expanding outer circulation leads to an increase in the mean radius of the air ascending into the eyewall updraught through nonlinear boundary-layer dynamics.

---

[3] Since the areal extent of the eyewall updraught increases, decreasing vertical velocity does not necessarily equate to a decreasing vertical mass flux.

During CW2, the decreasing translational speed of the tropical cyclone leads to stronger sea-surface cooling and a further decrease in the average SST. As in CW1, the decrease in the average SST and the accompanying decrease in Δq during CW2 are primarily responsible for the decrease in the average surface latent heat flux, all of which reach a global minimum for the RI phase and the mature phase. The decrease in the surface latent heat flux is accompanied by a decrease in $\overline{\theta_e}$ at the top of the boundary layer inside a 100 km radius. Consequently, $\langle\overline{\theta_e}\rangle_{up}$ decreases faster than in CW1 on account of both the local decrease in $\overline{\theta_e}$ and the increasing mean radius of the ascending air controlled by the expanding outer circulation. As before, the decreasing $\langle\overline{\theta_e}\rangle_{up}$ reduces the local buoyancy and the vertical velocity in the eyewall updraught. In contrast to CW1, the decrease in the vertical velocity is accompanied by a decrease in the vertical mass flux in the eyewall updraught. Nevertheless, the vertical mass flux in the eyewall updraught remains larger than that at its base. Hence, the eyewall updraught is still able to accept all the ascending boundary-layer air, although the radial inflow weakens in a vertical layer above the boundary layer at radii beyond the eyewall updraught. The weaker radial inflow, combined with the vertical advection of low M from within the boundary layer, leads to M-surfaces moving radially outwards above the boundary layer at radii beyond the eyewall updraught up to 100 km radius. Within this radial interval, the tangential wind speed at the top of the boundary layer decreases along with the radial pressure gradient transmitted into the boundary layer. The decrease in the radial pressure gradient changes the net radial force in the boundary layer. Through nonlinear boundary-layer dynamics, the changes in the net radial force, together with the expanding outer circulation, lead to an accelerated increase in the mean radius of air ascending into the eyewall updraught compared with CW1.

During the latter stage of CW2 and WF, the foregoing tendencies are reversed. The subsurface warm-core eddy reduces the strength of sea-surface cooling and the average SST increases. The increase in the average SST and the accompanying increase in Δq are primarily responsible for the increase in average surface latent heat flux. The increase in the surface latent heat flux is accompanied by an increase in $\overline{\theta_e}$ at the top of the boundary layer at radii inside 40 km. The value of $\langle\overline{\theta_e}\rangle_{up}$ increases because of both the local increase in $\overline{\theta_e}$ and the decreasing mean radius of the updraught, leading to an increase in the local buoyancy and the vertical velocity in the eyewall updraught. The increase in vertical velocity is accompanied by a sharp increase in the vertical mass flux in the eyewall updraught. Since the difference between the vertical mass flux within and at the base of the inward-moving eyewall updraught increases, the eyewall updraught is more able to accept the ascending boundary-layer air than during the decay in CW2. As a result, the radial inflow strengthens above the boundary layer and M-surfaces are drawn inwards at radii beyond the eyewall updraught. Correspondingly, the tangential wind speed at the top of the boundary layer increases along with the radial pressure gradient transmitted into the boundary layer at radii beyond the eyewall updraught. Again, through nonlinear boundary-layer dynamics, the strengthening outer circulation leads to a decrease in the mean radius of air ascending into the eyewall updraught, although a part of this decrease may be associated with the local suction effects of the increasing vertical mass flux, which are not captured by boundary-layer dynamics.

The outward-moving eyewall updraught in CW1 resembles the simulation in Kilroy et al. (2016) with constant SST, because the decrease in average surface latent heat flux does not have an appreciable effect on the thermodynamics of air ascending from the boundary layer into the eyewall updraught, captured by $\langle\overline{\theta_e}\rangle_{up}$. In CW2, by contrast, the decrease in $\langle\overline{\theta_e}\rangle_{up}$ cannot be explained without air-sea coupling. Air-sea coupling is also crucial also during the latter stage of CW2 and WF, where the increase in the average surface latent heat flux is accompanied by an increase in $\langle\overline{\theta_e}\rangle_{up}$ and a burst in eyewall convection.

The foregoing discussion shows that the change in SST and surface latent heat flux alone do not fully explain the changes in tropical cyclone intensity. Instead, it is necessary to consider both air-sea interactions and boundary-layer dynamics in order to acquire a complete picture of the changes in the azimuthal-mean structure and intensity of the simulated tropical cyclone.

Although repeating the coupled simulation at higher resolution may improve the robustness of the foregoing results, there are several reasons to believe that the qualitative behaviour described above would not change. Firstly, Fierro et al. (2009) found that the amplitudes of low-wavenumber asymmetries decrease with finer grid spacing from 5 to 1 km, suggesting that azimuthal-mean analysis would be appropriate down to at least a grid spacing of 1 km. Secondly, the most severe impact on the above results is likely to be connected to the diffusivity of the boundary-layer scheme. In models with overly diffusive boundary-layer schemes, the boundary-layer spin-up mechanism tends to be weaker (Smith et al., 2010a). This is because the boundary-layer depth scales with the square root of the eddy diffusivity (Smith, 1968). Since deeper boundary layers tend to have a weaker inflow, the eddy diffusivity affects the inward advection of M surfaces in the boundary layer. Nevertheless, the preceding analysis shows good agreement with the conceptual framework and this is unlikely to change with a less diffusive boundary-layer scheme. This agreement highlights the importance of understanding the individual processes within the conceptual framework, which recognises the role of boundary-layer dynamics and air-sea coupling for changes in tropical cyclone intensity.

A.6 THE ROLE OF BOUNDARY LAYER DYNAMICS FOR INTENSITY

As outlined in the conceptual framework (Section 3), the expanding outer circulation determines the change in both the boundary-layer convergence and the radius of forced ascent through boundary-layer dynamics. In Section 4, we articulated how these aspects of boundary-layer dynamics influence the decay and reintensification of a tropical cyclone simulated in the coupled atmosphere-ocean ICON model. However, we did not provide evidence for the expanding outer circulation controlling the increase in the mean updraught radius at the top of the boundary layer on account of boundary-layer dynamics as the tropical cyclone decays. Nor did we demonstrate a similar control when the mean updraught radius decreases during reintensification.

In this section, we follow Kilroy et al. (2016) and compare the ICON simulation with a steady-state slab boundary-layer model (Smith, 2003). By indicating the change in the radius of forced ascent in the presence of an expanding circulation, the comparison with the slab boundary layer provides an insight as to whether the expanding circulation is controlling the change in the radius of forced ascent in the ICON simulation.

A.6.1 *Slab boundary layer model*

The slab boundary-layer model solves for the radial velocity, $u_b(r)$, and tangential velocity, $v_b(r)$, in the boundary layer as a function of radius, r. The equations governing the steady-state slab boundary-layer model used here are derived from the momentum and continuity equations (see appendix). Therefore, the solution is based on dynamical considerations only; surface latent heat flux and inner-core convection in the eyewall are not included explicitly . Nonlinear terms, which are particularly large and cannot be neglected in the boundary layer, are retained in the momentum equations (Vogl et al., 2009). A steady-state model is appropriate here, because the boundary layer is thin and reacts to changes in the radial pressure gradient on short time-scales (Kilroy et al., 2016).

The boundary conditions for the slab boundary-layer model are the radial pressure gradient at the top of the boundary layer at height, h, and the frictional drag at the sea surface. We neglect the momentum flux into the boundary layer at h due to vertical diffusion, which is assumed to be small compared to the surface term. The radial pressure gradient at h is derived from the tangential velocity, assumed to be in gradient wind balance, and is transmitted into the slab boundary layer. The surface momentum flux is derived from the standard bulk aerodynamic formula and depends on wind speed and a drag coefficient, C_D. Density does not enter in the equations, because the fluid is assumed to be homogeneous.

For reasons outlined in Section A.5.1, we prescribe a fixed h of 780 m for the slab boundary-layer model. The tangential velocity from the corresponding vertical level is then used for the upper boundary condition. The choice of 780 m is also consistent with the assumption of gradient wind balance at h, which is satisfied during the mature phase in the ICON simulation to a good approximation (not shown).

We implement a function for C_D in the slab boundary-layer model that is compatible with observations (Black et al., 2007) and is given by,

$$C_D = C_{D0} + C_{D1}\left(1 - e^{-\alpha_d v_g}\right). \tag{A.3}$$

The gradient wind speed at the top of the boundary layer is denoted by v_g. When v_g is zero, C_D is equal to C_{D0}. For small v_g, C_D approximates a linear function of v_g. For large v_g, C_D asymptotically approaches $C_{D0} + C_{D1}$. The coefficients, C_{D0}, C_{D1} and α_d are set to 0.7×10^{-3}, 1.4×10^{-3} and 5.5×10^{-2}, respectively. These coefficients are chosen to fit C_D in the ICON model as closely as possible. With a view to keeping the model simple, we accept that an exact fit is not possible, because C_D in the ICON model is a more complicated function that is not only dependent on wind speed, but also consistent with the model's turbulence scheme.

A.6.2 *Results from the slab boundary layer model*

To facilitate a fair comparison with the slab boundary-layer model, the tangential and radial velocity in the ICON simulation are averaged over the lowermost 780 m. As shown in Figure A.16, the slab boundary-layer model captures the outward shift of v_b contours during CW1 and CW2. The slopes of the v_b contours in the slab boundary-layer model are in good agreement with the ICON simulation. For WF, the slab boundary layer correctly predicts that the v_b contours within a radius of 50 km no longer move outwards. However, while the inner edge of the solution moves inward, the slab boundary-layer model is unable to capture the full extent of the contraction in the ICON simulation; the v_b contours between 40 and 60 km do not move inwards. Note that a comparison is not possible at small radii, because the slab boundary layer solution breaks down when u_b goes to zero, shown by the cut-off.

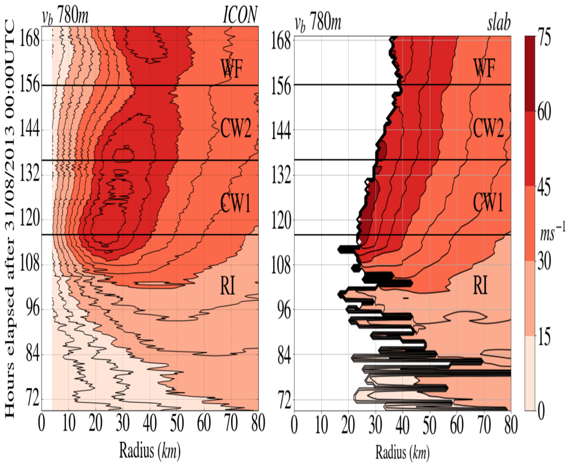

Figure A.16: The tangential velocity in the boundary layer, v_b, is displayed as a Hovmöller plot for the ICON (left) and the slab boundary layer model (right). For the ICON simulation, v_b represents a vertical average of tangential velocity over the lower 780 m in the atmosphere.

The comparison for u_b is shown in Figure A.17. Although u_b is consistently larger in the slab boundary-layer model, the slab boundary-layer model correctly predicts the expansion of u_b contours during CW1 and CW2 followed by the contraction in WF. Moreover, there is good agreement with the strengthening between the latter half of CW2 and WF.

A.6.3 *Discussion of results from the slab boundary layer model*

One cannot expect to avoid quantitative differences when comparing the ICON simulation with the highly idealised slab boundary layer model. Kepert (2010) showed that the slab boundary-layer model tends to overestimate the inflow strength, which is consistent with our results. At the same time, the weaker boundary-layer flow in the ICON simulation may be linked to excessive vertical diffusion in the ICON model (Zhang et al., 2010). An indication of excessive vertical diffusion is the relatively weak vertical gradient of inflow in the

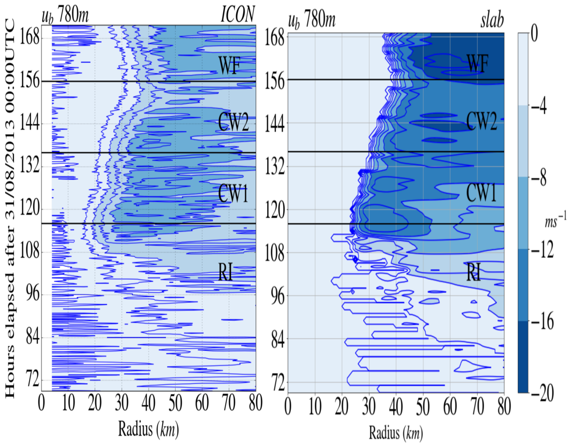

Figure A.17: The radial velocity in the boundary layer, u_b, is displayed as a Hovmöller plot for the ICON simulation (left) and the slab boundary layer model (right). For the ICON simulation, u_b represents a vertical average of tangential velocity over the lower 780 m in the atmosphere.

boundary layer (not shown) (Gopalakrishnan et al., 2013). Combined with the sensitivity of the slab boundary-layer model to h, as well as the lack of consensus on the definition of h, it does not make sense to provide an interpretation of small quantitative differences for our purposes (Zhang et al., 2011).

Despite its limitations, the slab boundary-layer model provides an important qualitative insight into the change in the radius of forced ascent at the top of the boundary layer, because its governing equations are parabolic. Information in parabolic equations flows in the direction of the physical flow, which is radially inwards in the slab boundary-layer model. Consequently, u_b and v_b at a given radius do not depend on the solution at smaller radii. For this reason, the slab boundary-layer model does not include the convective suction effect described in Section A.4.

The results for CW1 and CW2 are similar to the findings in Kilroy et al. (2016) for a decaying tropical cyclone and constant SST, where the slab boundary-layer model predicted the expansion of the u_b and v_b contours. As with Kilroy et al. (ibid.), the expansion of the u_b and v_b contours show that an increasing radius of forced ascent is being controlled by the expanding outer circulation in the ICON simulation via boundary-layer dynamics.

Similar to CW1 and CW2, the slab boundary-layer model can predict the contraction of the u_b contours and the innermost v_b contour. Again, the agreement between the ICON simulation and slab boundary layer shows that a decreasing radius of forced ascent is being determined by the expanding outer circulation through boundary-layer dynamics. The inability of the slab boundary-layer model to capture the full extent of the contraction of the v_b contours during WF is likely to be related to the enhanced convective suction effect discussed in Section A.5.8.

A.7 SUMMARY AND CONCLUSIONS

We examine how the atmospheric boundary layer modulates the intensity of a mature tropical cyclone influenced by a realistic ocean-eddy field in a fully coupled atmosphere-ocean model. To this end, we analyse a tropical cyclone simulated in the ICON model with a global, nonhydrostatic configuration and a horizontal grid spacing of 5 km. After reaching peak intensity, the simulated tropical cyclone experiences a period of decay following the interaction with its cold wake and subsequently reintensifies as it encounters a subsurface, warm-core eddy. The changes in the azimuthal-mean structure and intensity are analysed with the help of a conceptual framework that recognises the importance of boundary-layer dynamics, as well as the role played by air-sea interactions. A key part of the framework is the recognition that the change in the mean radius of updraught at the boundary-layer top is regulated by the expanding outer tangential wind field through boundary-layer dynamics.

Our study shows that the outward movement of the eyewall updraught associated with the cold wake is not due to air-sea interactions alone. During the early decay phase, the decrease in the average equivalent potential temperature of the boundary-layer updraught is related to an increase in the mean radius of the updraught rather than the decreasing SST and surface latent heat flux. However, later in the decay phase the decreasing SST and surface latent heat flux contribute to the decrease in equivalent potential temperature of the boundary-layer updraught. The accompanying decrease in the vertical mass flux in the interior of the eyewall updraught causes the radial inflow above the boundary layer to weaken, which ultimately leads to a more pronounced spin-down than earlier in the decay phase.

Similarly, boundary-layer dynamics and air-sea interactions both play an important role for the inward movement of the eyewall updraught in the reintensification phase, where the tendencies are reversed. The average equivalent potential temperature of the boundary-layer updraught is related to the decrease in the mean radius of the updraught, as well as the increase in local equivalent potential temperature arising from increasing SST and surface latent heat flux. The accompanying increase in vertical mass flux leads to a strengthening radial inflow above the boundary layer and spin-up of the tropical cyclone.

The ability of a steady-state slab boundary-layer model to predict the increase in the radius of forced ascent during the decay phase and, to a lesser extent, the subsequent decrease during reintensification provides evidence for the boundary-layer mechanism, first articulated by Kilroy et al. (ibid.), in a coupled atmosphere-ocean simulation. Namely, that the change in the radius of forced ascent is controlled by the expanding outer circulation on account of nonlinear boundary-layer dynamics. In turn, the change in the radius of forced ascent influences deep convection in the eyewall updraught, which then feeds back on the boundary-layer flow.

In addition, this study highlights another layer of complexity to the coupling between surface latent heat flux, SST, and near-surface wind speed through boundary layer dynamics. The near-surface wind speed and the change in surface latent heat flux are linked to the boundary-layer flow and depend on whether convergence in the boundary layer is dominated by the nonlinear dynamics of the boundary-layer flow or the suction effect. Thus, any feedback between surface latent heat flux and tropical cyclone intensity in coupled models ultimately involves nonlinear boundary-layer dynamics.

Taken together, the foregoing results show that boundary-layer dynamics should be incorporated into any explanation of changes in tropical cyclone intensity in response to sea-surface cooling in coupled atmosphere-ocean models with a realistic ocean-eddy field.

Further work is required to establish the robustness of these results for various degrees of sea-surface cooling and vertical wind shear. This is because sea-surface cooling tends to be highly asymmetric and vertical wind shear induces strong asymmetries in the tropical cyclone circulation. Such asymmetries are not captured in an axisymmetric framework. The asymmetric downdraughts associated with vertical wind shear and vortex tilt have been shown in previous studies to have a substantial effect on the boundary-layer thermodynamics, but it is not clear how these changes would affect the radius of forced ascent at the top of the boundary layer in a coupled atmosphere-ocean model. Further, recent studies have demonstrated that the sea-surface cooling can lead to the formation of a stable boundary layer over the asymmetric cold wake, which leads to asymmetries in the boundary layer flow. Again, it is unclear to what extent this asymmetric flow influences the radius of forced ascent.

Finally, this is the first study that investigates the effect of a warm-core eddy at depth on the kinematic structure of the tropical cyclone boundary layer with a fully three-dimensional eddy-resolving simulation. While the warm-core eddy is able to sustain a large surface latent heat flux and reduce sea-surface cooling due to a large ocean heat content, the degree of reintensification is inextricably linked to the decreasing radius of forced ascent and the accompanying changes in the kinematic and thermodynamic structure of the boundary layer. Conversely, our results suggest that boundary-layer dynamics play an important role in sea-surface cooling in coupled atmosphere-ocean simulations. Specifically, understanding the link between the outer circulation and radius of forced ascent through boundary-layer dynamics may improve predictions of tropical cyclone size, which is an important factor for sea-surface cooling.

A.8 ACKNOWLEDGEMENTS

The authors would like to thank Rene Redler, Monika Esch and Helmuth Haak, who ran the DYAMOND++ simulation at the Max Planck Institute for Meteorology, for making the ICON data available to us. The authors would also like to thank the DKRZ for providing computing resources. This paper is a contribution to the project L4 (Energy-Consistent Ocean-Atmosphere Coupling) of the Collaborative Research Centre TRR 181 "Energy Transfer in Atmosphere and Ocean" funded by the Deutsche Forschungsgemeinschaft (DFG, German Research Foundation) – project no. 274762653. Finally, the authors are grateful for the helpful feedback they received from three anonymous reviewers.

A.9 APPENDIX: SLAB BOUNDARY LAYER MODEL

The equations in the slab boundary layer are solved for the radial velocity, $u_b(r)$, tangential velocity, $v_b(r)$ and the vertical velocity, $w_h(r)$. Since the equations are steady state, the equations are solved separately for each time step. That is, a unique $u_b(r)$, $v_b(r)$ and $w_h(r)$ are obtained for each time step. Assuming that $u_b(r)$ and $v_b(r)$ are in geostrophic balance (not gradient wind balance) at a large radius, $r = R$, allows the equations to be solved for $u_b(R)$ and $v_b(R)$. The complete solutions to these equations are then obtained by incrementally integrating $u_b(r)$ and $v_b(r)$ radially inwards. As an intermediate step between each integration, the vertical velocity, $w_h(r)$, is computed with the local values of $u_b(r)$ and $v_b(r)$.

The equations are formulated on an f-plane in cylindrical polar coordinates and are given by,

$$\frac{du_b}{dr} = \frac{w_{h-}}{h} - \frac{(v_g^2 - v_b^2)}{ru_b} - \frac{f(v_g - v_b)}{u_b} - \frac{C_D}{h}(u_b^2 + v_b^2)^{\frac{1}{2}} \tag{A.4}$$

$$\frac{dv_b}{dr} = \frac{w_{h-}}{h}\frac{(v_b - v_g)}{u_b} - \left(\frac{v_b}{r} + f\right) - \frac{C_D}{h}(u_b^2 + v_b^2)^{\frac{1}{2}}\frac{v_b}{u_b} \tag{A.5}$$

$$w_h = \frac{h}{1+\alpha}\left[\frac{1}{u_b}\left\{\frac{v_g^2 - v_b^2}{r} + f(v_g - v_b) + \frac{C_D}{h}(u_b^2 + v_b^2)^{\frac{1}{2}}\right\} - \frac{u_b}{r}\right]. \tag{A.6}$$

The slab boundary-layer model treats the boundary layer as a single slab with no variation in the vertical, so that u_b and v_b are functions of radius only. Multiplying Equation A.4 by u_b gives the radial momentum equation. Similarly, multiplying Equation A.5 by u_b returns the tangential momentum equation. The terms on the left-hand side of Equation A.4 and A.5 correspond to the radial advection of radial momentum and tangential momentum, respectively. The first term on the right-hand side of these equations relate to the vertical advection of momentum. The term w_{h-} is related to w_h by $w_{h-} = \frac{1}{2}(w_h - |w_h|)$. For the case of negative w_h, w_{h-} and w_h have the same magnitude. If w_h is positive, w_{h-} is zero. Physically, this means that only downward advection of momentum from above the boundary layer influences the dynamics in the boundary layer, and not the upward advection of momentum out of the boundary layer. The second and third terms on the right-hand side in Equation A.4 are equivalent to the agradient force per unit mass divided by u_b. Here, v_g and f are the gradient wind above the boundary layer and the Coriolis parameter, respectively. The agradient force per unit mass, given by $(v_g^2 - v_b^2)/r + f(v_g - v_b)$, is the sum of the Coriolis and centrifugal forces for v_g minus the sum of Coriolis and centrifugal forces for v_b. The agradient force represents the radial force imbalance between the radial pressure gradient in the slab boundary layer, which is given by the sum of Coriolis and centrifugal forces for v_g, and the Coriolis and centrifugal forces in the slab boundary layer. When the agradient force is zero, the flow is in gradient wind balance. Hence, the agradient force quantifies the deviation of the flow from gradient wind balance. Finally, the last term in Equation A.4 and A.5 represents the effect of friction at the surface, which depends on the drag coefficient, C_D, and the horizontal wind speed, $(u_b^2 + v_b^2)^{\frac{1}{2}}$. For further information on this boundary-layer model, the reader is referred to Smith, 2003.

B

THE IMPACT OF OCEAN EDDIES ON TROPICAL CYCLONE INTENSITY IN A ONE-YEAR, GLOBAL COUPLED ATMOSPHERE-OCEAN SIMULATION

B.1 ABSTRACT

We study the impact of ocean eddies on tropical cyclone intensity with a one-year, global simulation run with the coupled atmosphere-ocean ICOsahedral Nonhydrostatic (ICON) model. The ocean component is initialised with atmospheric forcing prior to coupling, permitting the formation of background oceanic features, including ocean eddies and currents. The model simulates a reasonable climatology with a total of 66 tropical cyclones that are category 1 or stronger and 24 major tropical cyclones (category 3 - 5). Encounters between the tropical cyclones and ocean eddies are common. In total, 107 ocean eddies are encountered by the tropical cyclones, of which 63 are cold-core eddies and 44 are warm-core eddies. More than 70% of the tropical cyclones encounter at least one ocean eddy and 45% encounter two or more. Our analysis reveals that tropical cyclones that encounter warm-core eddies reach on average a higher peak intensity, whereas cold-core eddies do not have an effect on the average peak intensity. If these results prove to be robust, they point to a potential bias in future projections of tropical cyclone intensity, which are based on global climate simulations that do not resolve ocean eddies.

B.2 INTRODUCTION

This study examines whether ocean eddies have an effect on tropical cyclone intensity in a one-year, global, convection-permitting, coupled ocean–atmosphere simulation with 5-km horizontal grid spacing. Ocean eddies influence tropical cyclone intensity by possessing a subsurface structure that differs from that of the ambient ocean. When a tropical cyclone encounters an ocean eddy, the sudden change in the subsurface ocean structure changes the strength of the sea-surface cooling induced by the tropical cyclone. By impacting the strength of the sea-surface cooling, ocean eddies influence the surface latent heat flux, which is the primary energy source for tropical cyclones (Emanuel, 1986). Warm-core eddies can sustain a large surface latent heat flux, which can lead to a substantial increase in tropical cyclone intensity (Kumar et al., 2021).

The surface latent heat flux is a function of the moisture disequilibrium and the near-surface wind speed, of which the former depends on SST. A decrease in SST associated with sea-surface cooling equates to a decrease in surface latent heat flux if the near-surface wind speed and the near-surface specific humidity fields are held constant in time. In reality, near-surface wind speed and near-surface specific humidity are not constant. However, numerical studies using coupled atmosphere-ocean models have shown that sea-surface cooling results in tropical cyclones with smaller surface latent heat fluxes and lower maximum intensities, compared to the case where sea-surface cooling is absent (Bender et al., 1993; Chang et al., 1979; Khain et al., 1991). The importance of sea-surface cooling for tropical cyclone intensity is exemplified by the improvement in intensity forecasting displayed by coupled atmosphere-ocean models, which capture sea-surface cooling, over the atmosphere-only models that do not (Balaguru et al., 2018; Bender et al., 2000; Mogensen et al., 2017).

The relation between sea-surface cooling, surface latent heat flux and maximum intensity is often conceptualised as a negative feedback. As the tropical cyclone intensifies, the sea-surface cooling increases in magnitude on account of increasing wind-stress at the air-sea interface and due to the upward mixing of colder water masses. This sea-surface cooling leads in turn to a decrease in surface latent heat flux that acts to prevent the tropical cyclone from intensifying further. By influencing the degree of sea-surface cooling, the subsurface ocean structure affects the strength of this negative feedback and, ultimately, the tropical cyclone intensity. Given the importance of the subsurface ocean structure for sea-surface cooling, the subsurface ocean structure is considered to be of first-order importance for tropical cyclone intensity forecasting (Emanuel, 1999).

Ocean eddies are a feature of the subsurface ocean that are of particular interest for tropical cyclone intensity forecasting. Observational studies have shown that tropical cyclones encountering warm-core eddies appear to weaken the negative feedback by suppressing sea-surface cooling and maintaining a high surface latent heat flux, leading to intensification and, in the case of Hurricane Katrina (2005) and Hurricane Opal (1995), rapid intensification (Ali et al., 2007; Jaimes et al., 2009b, 2016; Lin et al., 2005; Patnaik et al., 2014; Shay et al., 2000). Conversely, observations of tropical cyclone decay has been linked to cold-core eddies that strengthen the negative feedback by enhancing sea-surface cooling and reducing surface latent heat flux (Jaimes et al., 2009b; Patnaik et al., 2014). The aforementioned effect of warm-core and cold-core eddies on tropical cyclone intensity has been demonstrated by numerous modelling studies of varying complexity (Hong et al., 2000; Lin et al., 2005; Ma et al., 2013; Wu et al., 2007b; Yan et al., 2017).

Warm-core eddies tend to suppress sea-surface cooling because they possess a deeper mixed layer with a higher ocean heat content (OHC) than their surroundings. Cold-core eddies tend to enhance sea-surface cooling due to their shallower mixed layer and lower OHC compared to the ambient environment. However, the cooling of the mixed layer and, ultimately, the sea surface under tropical cyclone forcing depends not only on the vertical thermal structure of the ocean eddy but also on the the circulation of the eddy. Jaimes et al. (Oct. 2011) found that the anticyclonic circulation of warm-core eddies suppressed mixed-layer cooling due to downwelling, weak stratification over the deep warm water column and the vertical dispersion of near-inertial energy. Conversely, the cyclonic circulation of cold-core eddies favours mixed-layer cooling through a combination of upwelling, strong stratification and the trapping of near-inertial energy that enhances vertical-shear driven mixing at the base of the mixed layer. Yablonsky et al. (Mar. 2012) demonstrated the possibility of the anticyclonic circulation of a warm-core eddy positioned to the right of the track (in the Northern Hemisphere) to advect colder waters under the tropical cyclone centre, such that the warm-core eddy weakens the intensity. The sea-surface cooling is also a function of the background oceanic flow in which the ocean eddy is embedded. While wind forcing leads to upwelling under the tropical cyclone centre for an ocean intially at rest (O'Brien et al., 1967), this is not necessarily the case for a geostrophic ocean, where the upwelling depends on the projection of the wind stress vector on the geostrophic flow (Jaimes et al., 2009b).

While numerous studies provide compelling evidence of ocean eddies playing an important role for tropical cyclone intensity in individual case studies, it is not clear how often tropical cyclones encounter ocean eddies on a global scale. Analysis of best-track data and satellite altimetry by Ma et al. (2017)showed that 90% of tropical cyclones in the western Pacific between 2002 and 2011 encounter ocean eddies, suggesting that such encounters may be common on a global scale. However, even if tropical cyclones encounter ocean eddies often, it is not clear what impact they would have on tropical cyclone intensity. This is partly because ocean eddies vary substantially in size and structure, but also because the aforementioned negative feedback mechanism is a highly idealised simplification of the physics that govern the tropical cyclone, the ocean eddy and the coupling between the atmosphere and the ocean.

Strictly speaking, the surface wind-stress, and hence the sea-surface cooling, depends on the near-surface wind speed rather than the tropical cyclone intensity, which refers to the maximum near-surface wind speed. The total time-integrated wind-stress forcing at a given point is also a function of tropical cyclone size and translation speed, with larger and slower moving tropical cyclones taking longer to pass overhead. Therefore, the degree to which an ocean eddy suppresses or enhances the sea-surface cooling depends on the near-surface wind field, the size and the translation speed.

Furthermore, the relationship between surface latent heat flux and tropical cyclone intensity is highly non-linear. The complexities of how tropical cyclone intensity changes in response to a change in surface latent heat flux can be understood with a basic conceptual model of a mature, axisymmetric tropical cyclone (Kumar et al., 2021; Montgomery et al., 2017; Ooyama, 1982; Ooyama, 1969). An intensifying tropical cyclone corresponds to a vortex spinning up with angular momentum surfaces moving inwards. Conversely, a decaying tropical cyclone equates to a vortex spinning down with angular momentum surfaces moving outwards. While a decrease in surface latent heat flux can reduce the buoyancy of boundary layer air that rises into the eyewall above, the radius at which the converging boundary layer air is forced upwards depends on boundary layer dynamics (Kilroy et al., 2016; Kumar et al., 2021; Smith et al., 2009). Therefore, both boundary layer dynamics and thermodynamics influence the eyewall convection, and hence the transverse overturning circulation in a tropical cyclone. Depending on the advection of angular momentum surfaces by the overturning circulation, the tropical cyclone proceeds to spin up or down. Taken together with other environmental factors that affect tropical cyclone intensity, such as vertical wind shear (Frank et al., 2001; Kaplan et al., 2003; Wong et al., 2004), the highly coupled nature of the tropical cyclone circulation makes foreseeing the response of tropical cyclone intensity to ocean eddies more difficult.

In this study, we investigate the impact of ocean eddies on tropical cyclone intensity on a global scale. To this end, we analyse a one-year simulation run with the global, convection-permitting, coupled atmosphere-ocean ICON model with a 5-km horizontal grid spacing. Background oceanic features, including ocean eddies, are recreated through a spin-up process of the ocean prior to coupling with the atmosphere (not to be confused with tropical cyclone spin up). The analysis is divided into two main parts. Firstly, we use a tracking algorithm to extract the tropical cyclone tracks and compare the tropical cyclone climatology simulated in the model with the observational record. We also identify the ocean eddies that are intersected by the tropical cyclone tracks. Then, we analyse the effect of ocean eddies on tropical cyclone intensity by sorting the simulated tropical cyclones according to whether they encounter WCEs or CCEs. We compare the peak intensity, track-averaged SST, and track-averaged surface latent heat flux to see if there is a statistically significant difference between these groups. A description of the model and the simulation is given in Section B.3. The algorithms used to track the tropical cyclones and identify ocean eddies are outlined in Section B.4. An overview of the tropical cyclone climatology is given in Section B.5, followed by the analysis of the impact of WCEs and CCEs in Section B.6 and the conclusion in Section B.7.

B.3 ICON MODEL DESCRIPTION AND SIMULATION

To study the effect of ocean eddies on tropical cyclone intensity, we analyse an existing one-year simulation run as part of the development of the 5-km, global, coupled atmosphere–ocean ICON model (Korn, 2017; Zängl et al., 2015). The atmosphere has a total of 70 vertical levels with a model top at a height of 30 km. The lowermost nine vertical levels lie below 1 km, ensuring adequate resolution of the boundary layer flow. The ocean includes bottom topography and 128 vertical levels. Similar to the atmosphere, the 12 levels in the uppermost 100 m of the ocean allow for sufficient resolution of the vertical structure of ocean eddies. The model time steps for the atmosphere and ocean are 30 seconds and 90 seconds, respectively. Fluxes are exchanged between the atmosphere and the ocean every 15 minutes.

The ICON physics package for the atmosphere is based on the physics package implemented in the ECHAM model developed at the Max Planck Institute for Meteorology (Giorgetta et al., 2018). Crucially, convection is not parameterised in our simulation. The cloud physics scheme simulates both ice and water hydrometeors. The vertical transport at subgrid scales via turbulent motion is parameterised with a Smagorinsky diffusion scheme. Vertical mixing in the upper ocean is parameterised with a turbulent kinetic energy (TKE) scheme (Gaspar et al., 1990). The ocean resolves long surface gravity waves, but does not resolve short surface gravity waves, including breaking surface waves. However, the TKE associated with these breaking surface waves appears as a source term in the TKE equation of the Gaspar mixing scheme.

The atmosphere was initialised using remapped ECMWF operational analysis data for 20th January 2020 (Dee et al., 2011). The ocean was spun up by applying climatological atmospheric forcing from the fifth generation ECMWF atmospheric dataset (ERA5). The spin up process recreates background oceanic features, including currents and ocean eddies. Following the atmospheric initialization and ocean spin up, the atmosphere and ocean are run in coupled mode for one year until 20th January 2021.

B.4 ALGORITHMS FOR TRACKING TROPICAL CYCLONES AND IDENTIFYING OCEAN EDDIES

To analyse the impact of ocean eddies on tropical cyclone intensity, it is necessary to identify the tropical cyclones and the ocean eddies they encounter from the ICON output data. We first derive the tropical cyclone tracks globally and then identify ocean eddies locally for each tropical cyclone within a region enclosing the track. Since the location of ocean eddies changes little over the typical lifetime of a tropical cyclone, the ocean eddies are only identified at the time step when the tropical cyclone is initially detected and not at all time steps throughout the tropical cyclone's lifetime.

B.4.1 *Tropical-cyclone tracking algorithm*

Our tropical-cyclone tracking algorithm uses the mean sea-level pressure and the 10-m wind speed between 40° S and 40° N. The algorithm starts at the first simulation time step and loops over all the time steps in ascending order. For each time step, the algorithm is divided into two steps: (1) updating the tracks for pre-existing tropical cyclones and (2) detecting new tropical cyclones. In step (1), the tracking algorithm computes the lowest mean-sea level pressure within a radius of 400 km of each tropical-cyclone track point from the previous time step. If the lowest mean sea-level pressure is less than 999 hPa, the coordinate of the corresponding grid cell is added to the track. Otherwise, the track is terminated. All the grid cells within a 400-km radius of any detected tropical cyclone centre are masked in the input data to avoid double counting. In step (2), the tracking algorithm takes the masked input fields and searches for the grid cell with the lowest mean sea-level pressure. If the mean sea-level pressure is less than 990 hPa and the maximum near-surface wind speed within a radius of 400 km exceeds 17 m/s, the coordinate of the corresponding grid cell is taken to be the start of a new track. If the minimum mean sea-level pressure is less than 990 hPa, but the maximum near-surface wind speed is less than 17 m/s, no new track is added. In both cases, the algorithm masks out all grid cells within 400 km of the minimum mean sea-level pressure and then repeats the procedure for the minimum mean sea-level pressure of the remaining grid cells. The algorithm continues to search for new grid cells, until there are no cells remaining with a mean sea-level pressure less than 990 hPa. Once this point is reached, the algorithm moves to the next time step.

Implementing our own tracking algorithm instead of a pre-existing algorithm maximises flexibility in adjusting thresholds that are suited to the tropical cyclones simulated on the ICON model's unstructured grid. This approach is justified because there is a lack of consensus on the ideal tracking algorithm; the thresholds and input variables used in tracking algorithms, with the exception of the 10-m wind speed, vary substantially in global climate simulations (Horn et al., 2014). Consistent with other tracking algorithms, the 10-m wind speed is the key variable for detection and tracking in our algorithm. The 10-m wind thresholds used in tracking algorithms is typically lower than the threshold of 17 ms^{-1} in observations, with the exact threshold depending on the grid spacing of the model. However, for a grid spacing of 50 km, the recommended 10-m wind threshold deviates by less than 1 ms^{-1} from 17 ms^{-1} and quickly converges on 17 ms^{-1} as grid spacing decreases further (Walsh et al., 2007). Given the grid spacing in the ICON model is substantially smaller than 50 km, we assume 17 ms^{-1} to be an appropriate threshold for detecting tropical cyclones in the ICON simulation. We filter out tropical storms as a post-processing step by removing those tropical cyclones with a maximum 10-m wind speed that does not exceed 33 ms^{-1}. Removing the tropical storms allows us to focus on stronger tropical cyclones where the wind forcing is larger and the strength of the negative feedback is presumably stronger. Since warm-core thresholds are less important for strong tropical cyclones that already have a distinct warm core (ibid.), our algorithm does not scan the temperature field for a warm core.

B.4.2 *Eddy-identification algorithm*

Our eddy-identification algorithm follows Matsuoka et al. (2016) with a different method for computing the eddy's outer boundary. Furthermore, we do not implement the tracking aspect of their algorithm, because we only seek to identify ocean eddies at a single time step. The identification of each eddy centre and its respective inner boundary is identical to their algorithm and takes as inputs the sea surface height (SSH) and the Okubo-Weiss parameter. The Okubo-Weiss parameter is defined as the stress squared plus the strain squared minus vorticity and is negative for ocean eddies. Our method for computing the outer boundary is based on the circulation of the surface current, rather than the surface-current-magnitude threshold used in Matsuoka et al. (2016) that is optimised for eddies in the vicinity of the Pacific Kuroshio current and not necessarily appropriate for other ocean basins. However, it is not clear if our method functions better on a global scale. For each tropical cyclone, we select a rectangular domain with a latitude and longitude interval equal to that spanned by the track plus a buffer of 5 ° for each of the four sides. This buffer ensures that the selected domain includes the full radial extent of the tropical cyclone at all points along its track.

The algorithm searches the selected domain for grid cells that correspond to the centre of an ocean eddy. We define an eddy centre as a minimum or maximum in SSH where the Okubo-Weiss parameter is negative. To qualify as an SSH minimum or maximum, the grid cell and its neighbours must satisfy the conditions imposed by the 9x9 filter shown in Figure B.1. To apply the 9x9 filter, the SSH field is interpolated onto a rectangular grid with a grid spacing of 0.1 °. After all eddy centres are computed, the algorithm proceeds to define the inner and outer boundary of each eddy. The inner boundary is a contour of constant SSH. To determine the SSH value of the inner-boundary contour, the algorithm computes the radius from the eddy centre to the nearest SSH inflection point for 20 equally spaced polar angles ranging from 0 to 360 degrees. The smallest radius is selected and the SSH at the corresponding inflection point defines the inner-boundary contour. The outer boundary is defined by a contour that is identical in shape to the inner-boundary contour, but may be larger by a scale factor. The chosen scale factor maximizes the circulation of the surface current and is constrained to lie between one and two.

An example of the eddy inner and outer boundaries computed with the algorithm is shown in Figure B.2. The same set of eddy contours are shown overlaid on the Okubo-Weiss parameter field and the SSH field in Figure B.2 a) and b), respectively. The algorithm

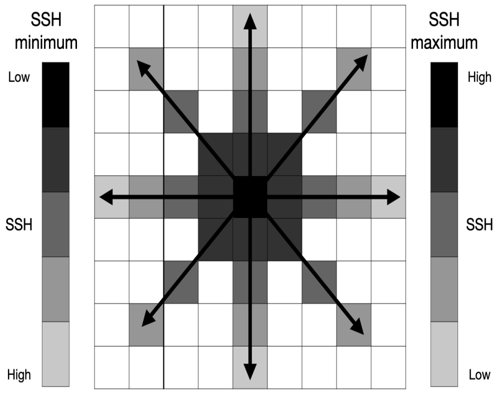

Figure B.1: Schematic of the 9x9 filter adapted from Matsuoka et al., 2016. Each square represents a single grid cell. If the eddy is associated with an SSH minimum, the SSH successively increases from the central cell (black) outwards for each of the 8 paths (arrows) separately. SSH values on different paths are not compared. If the eddy is associated with an SSH maximum, the SSH successively decreases along the same paths.

is able to capture most of the ocean eddies which appear as coherent features with a negative Okubo-Weiss parameter surrounded by a rotational flow. However, there are also a number of false positives, which may influence the statistics in this study. Despite identifying false positives, the algorithm is sufficient in the sense that it does correctly identify features that are clearly ocean eddies.

As outlined above, the outer-eddy boundaries are constrained to have the same shape as the inner-eddy boundaries. This constraint yields outer-eddy boundaries that sometime deviate markedly from the actual outer-eddy boundary. However, the precise shape of the outer-eddy boundary presumably has a smaller effect on the number of intersections between eddies and tropical cyclone tracks compared to the size and location of the eddies. Moreover, there is no consensus on the definition of the outer-eddy boundary; methods to determine the outer-eddy boundary analyse various fields, including streamline functions, SSH signatures, the Q-Criterion and the Okubo-Weiss parameter (Chaigneau et al., 2008; Chelton et al., 2011; Williams et al., 2011; Yi et al., 2014). For these reasons, we believe our algorithm is sufficient for the purposes of this study.

B.5 TROPICAL CYCLONE CLIMATOLOGY

In the following section, we provide a overview of the tropical cyclone climatology simulated by the ICON model. We start by presenting the tropical cyclone tracks in Section B.5.1, followed by a comparison between the simulated tropical cyclone intensity and frequency with the observational record in Section B.5.2. In Section B.5.3, we examine the simulated pressure-wind relationship. Finally, we examine the sea-surface cooling associated with the tropical cyclones and the number of eddies they encounter in Section B.5.4 and Section B.5.5, respectively.

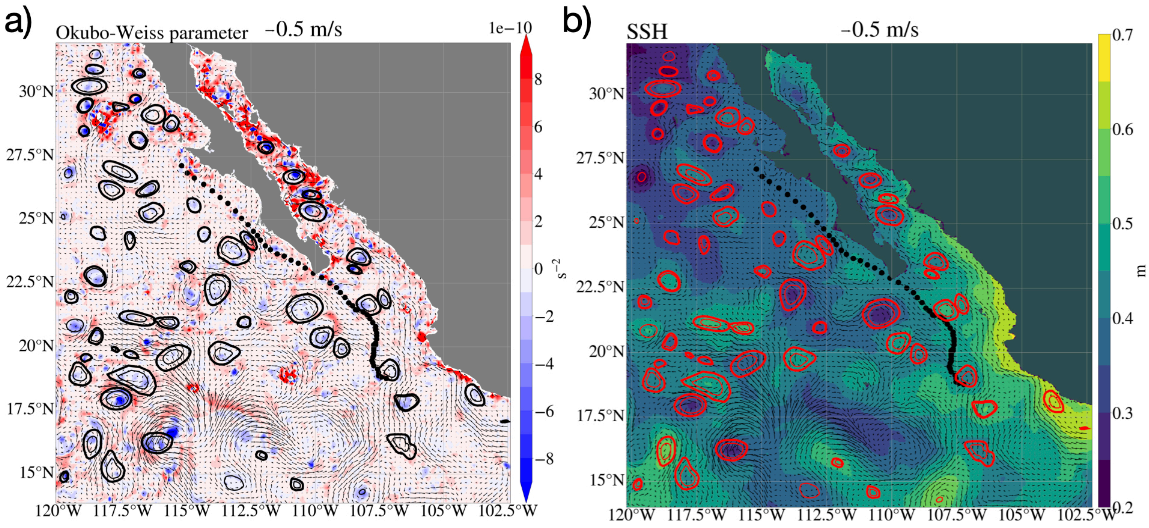

Figure B.2: Two plots of the ocean eddies identified for a single track off the west coast of Mexico overlaid on a) the Okubo-Weiss parameter and b) the sea surface height. The inner- and outer-eddy contours are shown as thin and thick loops, respectively. The surface current is displayed in both plots with black arrows scaled according to the magnitude. The track points are also indicated in both plots by solid black circles.

B.5.1 *Tracks*

The tropical cyclone tracks are displayed in Figure B.3. The tracks are located in the Pacific Ocean, the Southern Indian Ocean and the North Atlantic Ocean, including the Gulf of Mexico. Besides the lack of tracks in the North Indian Ocean, the geographical region covered by the tracks and the greater number of tracks in the Northern Hemisphere than the Southern Hemisphere is in agreement with tropical cyclone climatology. Note that only tropical cyclones with a maximum intensity of at least 33 m/s, corresponding to category 1 on the Saffir-Simpson scale, remain after the post-processing step of the tracking algorithm. The tracks do not extend south of 40° S and north of 40° N, because this is the domain of the input fields used by the tracking algorithm. The choice of domain prevents the algorithm from detecting erroneously long tracks, which arise because the algorithm often does not terminate the tracks for tropical cyclones that leave this domain due to the lower climatological mean sea-level pressure at high latitudes. Although in reality tropical cyclone tracks extend beyond 40° S and 40° N, tropical cyclone genesis occurs within this domain (Gray, 1975). Correspondingly, we do not expect the number of tracks to be affected by our choice of domain.

B.5.2 *Intensity and frequency*

As shown in Table 2, the 66 tropical cyclones (Category 1 - 5) in the ICON simulation is substantially larger than the 45 tropical cyclones observed in 2020 and the yearly mean of 47.5 tropical cyclones between 1981 and 2010. The number of simulated tropical cyclones

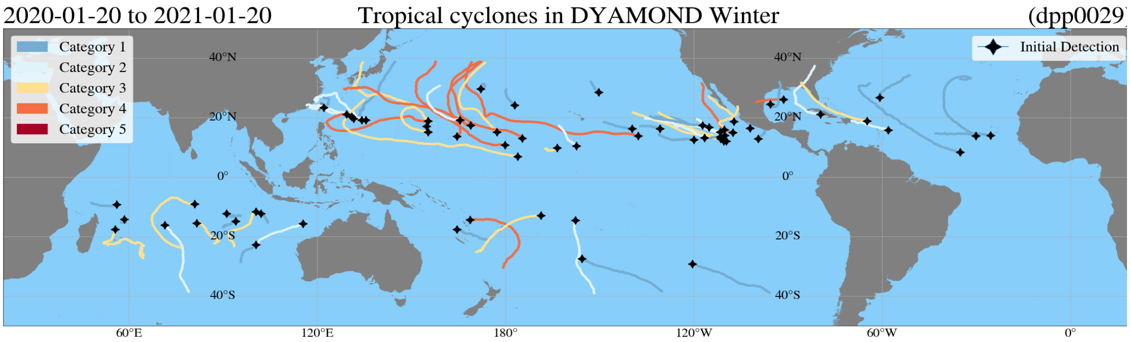
2020-01-20 to 2021-01-20
Tropical cyclones in DYAMOND Winter
(dpp0029
Category 1
Category 2
Category 3
Category 4
Category 5
Initial Detection
40°N
20°N
0°
20°S
40°S
60°E
120°E
180°
120°W
60°W
0°

Figure B.3: Global map of tropical cyclone tracks in the simulation. The black marker denotes the location at which each tropical cyclone is initially detected. The tracks are colour-coded according to the peak intensity reached by the tropical cyclone over its lifetime.

Storm type	Simulation count	Observation count (2020)	Mean count (1981-2010)	Record count (1972-2020)
Tropical cyclone (Category 1-5)	66	45	47.5	59 (2018, 2020)
Major tropical cyclone (Category 3-5)	24	21	23.4	39 (1990, 1992, 2018)
Accumulated cyclone energy (ACE $\times 10^4$ kt^2)	697.7 (excluding tropical storms)	579.9	770.2	1163.1 (1992)

Table 2: Table comparing the simulated frequency of tropical cyclones and simulated accumalated cyclone energy with observations. Note that the simulated time period starts on 21st January 2020 and ends on 21st January 2021, whereas the observed values refer strictly to the year 2020. The observational data is taken from: NOAA National Centers for Environmental Information, State of the Climate: Tropical Cyclones for Annual 2020, published online January 2021, retrieved on April 20, 2021 from `https://www.ncdc.noaa.gov/sotc/tropical-cyclones/202013`.

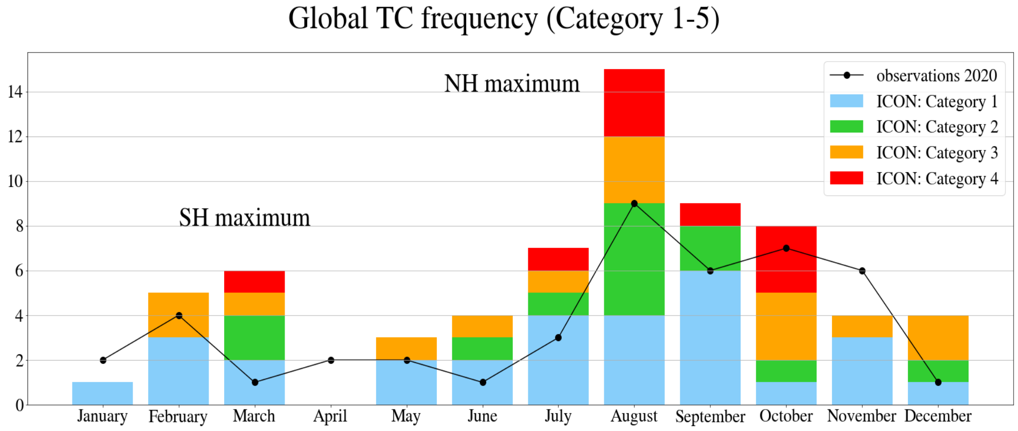

Figure B.4: Comparison between simulated monthly tropical-cyclone frequency across the globe with observations from 2020. The frequency for the simulated tropical cyclones is shown as a stacked bar chart sorted according to category. Observed values for 2020 are shown as black dots. Observations are taken from the same source as for Table 2.

also exceeds the yearly record between 1972 and 2020 of 59. However, there is good agreement in terms of major tropical cyclones, defined as being category 3 or stronger. The 24 simulated major tropical cyclones is similar to the observed number of 21 in 2020 and the yearly mean of 23.4 between 1981 and 2010. The number of major tropical cyclones is much lower than the record of 39 for the period from 1972 until 2020. Also, the accumulated cyclone energy (ACE), which is a measure of tropical cyclone frequency, intensity and duration, lies between the observed ACE for 2020 and the mean ACE.

Figure B.4 shows the global monthly frequency of tropical cyclones for the ICON simulation and for observations in 2020. The simulated monthly frequency exceeds that of the observations for all months, with the exception of January, April and November. The simulated monthly frequency peaks in August, which is consistent with the observations and reflects the higher frequency of tropical cyclones in the Northern Hemisphere compared to the Southern Hemisphere. A smaller peak in March corresponds to the height of the tropical cyclone season simulated in the Southern Hemisphere. In the observations, this peak occurs in February, a month earlier than in the simulation. No tropical cyclones are simulated in April.

Figure B.4 also shows the breakdown of monthly frequency by category. None of the simulated tropical cyclones intensify into category 5 tropical cyclones. The months with the highest frequency of major tropical cyclones are August and October with 6 each. All the category 4 tropical cyclones in the Northern Hemisphere occur between the beginning of July and the end of October, the four months with the largest number of tropical cyclones. Apart from one category 4 tropical cyclone in the Gulf of Mexico, all category 4 tropical cyclones are found in the Pacific (Figure B.3).

The tendency for the model to simulate too many tropical cyclones throughout the year may be linked to the simulated large-scale environment being too conducive to tropical cyclone genesis. Environmental factors that are conducive to genesis include high SST and low vertical wind shear, which are accounted for in genesis indices (Menkes et al., 2012).

The representation of the Madden-Julian Oscillation, which is highly model dependent, may also be a contributing factor for the discrepancy between the simulated and the observed monthly frequency (Satoh et al., 2012). The Madden-Julian Oscillation is one of the main sources of predictability on intraseasonal time scale in the tropics and modulates tropical cyclone frequency globally (Camargo et al., 2009, 2016; Klotzbach, 2014; Klotzbach et al., 2015). On the other hand, there are large differences in tropical cyclone frequency across models with similar genesis indices, which suggests that the frequency is more strongly controlled by the simulated dynamics of the tropical cyclone circulation rather than the large-scale environment (Camargo, 2013; Camargo et al., 2016).

B.5.3 *Pressure-wind relationship*

Figure B.5 shows the pressure-wind relationship for the ICON simulation compared with the observed relationship for 2020. The ICON pressure-wind relationship has a steeper negative gradient than the observed relationship. For category 1 tropical cyclones, there is a substantial overlap between the simulated and observational data points. At wind speeds corresponding to category 2 or higher, the simulated tropical cyclones generally have a lower pressure than the observed tropical cyclones. The pressure gap between the observed and simulated tropical cyclones increases with increasing wind speed.

The deviation between the pressure-wind relationship may be related to the surface drag coefficient in the model. Bao et al. (Oct. 2012) demonstrated that switching from a surface drag coefficient that increases linearly with wind speed to a coefficient that increases linearly and then plateaus at high wind speeds yields tropical cyclones with a larger minimum pressure but a similar wind speed. As the surface drag coefficient in the ICON model increases linearly with wind speed, modifying the wind dependence so that the drag coefficient plateaus at high wind speeds may bring the simulated pressure-wind relationship closer to the observed relationship. Bao et al. (Oct. 2012) also show that the choice of boundary layer mixing scheme and other subgrid parameterisations have a tangible impact on both the minimum pressure and maximum wind speed by influencing the kinematic structure of the tropical cyclone. It should be noted that the data points correspond to surface fields in the boundary layer, where gradient wind balance does not hold. Therefore, caution should be applied when invoking gradient wind balance to interpret the differences in the pressure-wind relationship.

B.5.4 *Sea-surface cooling*

We define the sea-surface cooling at each track point, ΔSST, as the change in SST from 24 hours before to 24 hours after the tropical cyclone is directly overhead. The SST at both time steps is an average over the circular region centred on the track point with a radius equal to the radius of maximum wind speed when the tropical cyclone is directly overhead.

Figure B.6 shows the time series of ΔSST averaged over all tropical cyclones of the same category. Before averaging, all the time series are centred on the time step where the ΔSST is most negative, which corresponds to the strongest sea-surface cooling. The magnitude

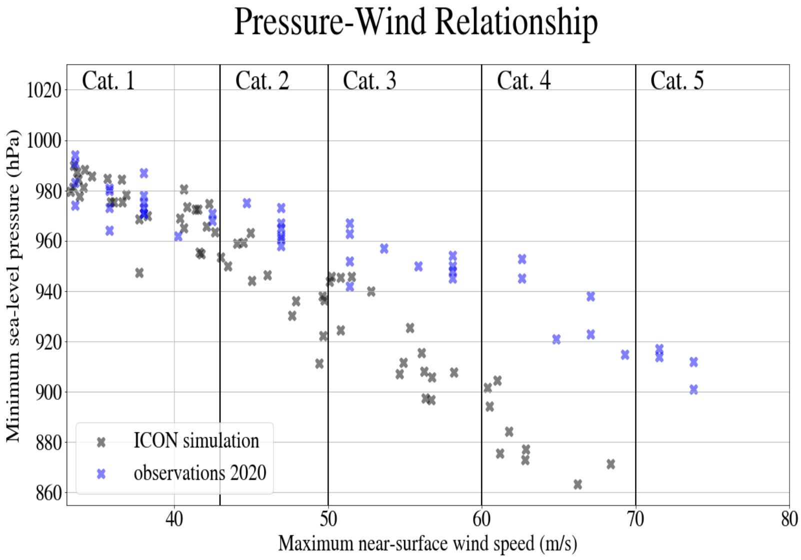

Figure B.5: Comparison between the simulated pressure-wind relationship and the observed pressure-wind relationship for 2020. The observations are taken from the same source as in Table 2.

of ΔSST increases going from category 1 to category 4, indicating that, on average, the maximum strength of the sea-surface cooling increases with increasing tropical cyclone intensity.

Figure B.7 shows a scatter plot of ΔSST averaged along each track, $\overline{\Delta SST}$, plotted against the maximum near-surface wind speed attained by the corresponding tropical cyclone. In contrast to ΔSST, $\overline{\Delta SST}$ does not display a clear increase in magnitude with increasing intensity. The data points with error bars show the average $\overline{\Delta SST}$ for each category and the associated standard deviations. While the average $\overline{\Delta SST}$ increases in magnitude from category 1 to category 2, there is a relatively small increase between category 2 and category 3. Similarly, the average $\overline{\Delta SST}$ displays a relatively small increase between category 3 and 4. Although the method to calculate ΔSST differs slightly, the relative small increase in the magnitude of average $\overline{\Delta SST}$ above category 2 is broadly in agreement with the observational study by Lloyd et al. (Feb. 2011).

B.5.5 *Tropical-cyclone-eddy encounters*

We define an encounter between a tropical cyclone and an ocean eddy when at least one track point lies within the eddy's outer-boundary contour. This definition is conservative, given that tropical cyclones typically have a much larger radius than ocean eddies. Nevertheless, we choose this definition, because the inner region of the tropical cyclone is where the surface latent heat flux is most sensitive to sea-surface cooling on account of high wind speeds (Cione et al., 2003). According to this definition, there are a total of 107 ocean eddies that are encountered by the tropical cyclones in the ICON simulation. Of these ocean eddies, 63 are cold-core eddies (CCE) and 44 are warm-core eddies (WCE). The larger

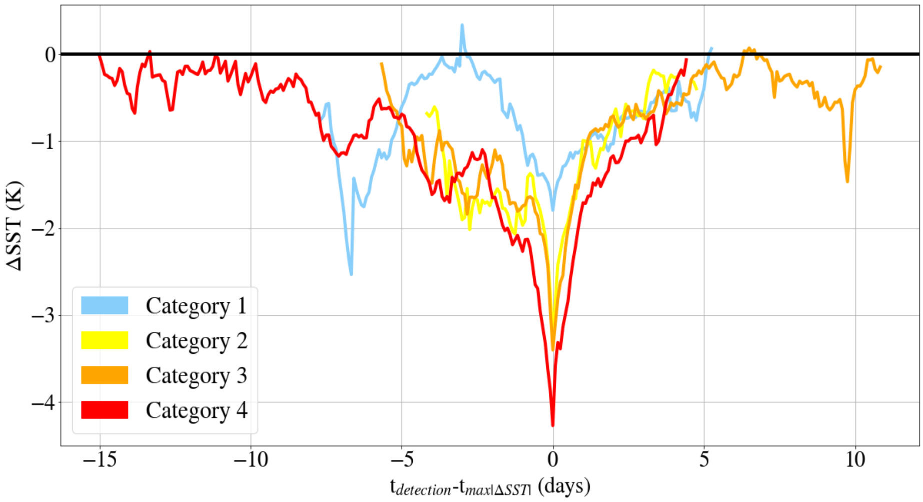

Figure B.6: Simulated sea-surface cooling averaged across all tropical cyclones of the same category. Prior to averaging, all the time series are centred on the time step where sea-surface cooling is strongest, i.e. ΔSST is most negative.

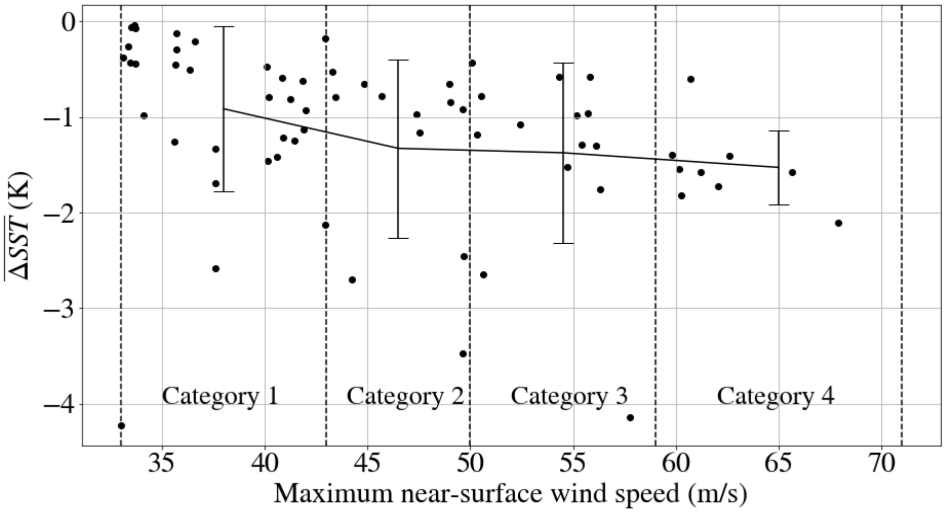

Figure B.7: Scatter plot of track-averaged sea-surface cooling plotted against the maximum near-surface wind speed obtained by the tropical cyclone. The vertical lines represent the binned averages and the standard deviations for each category.

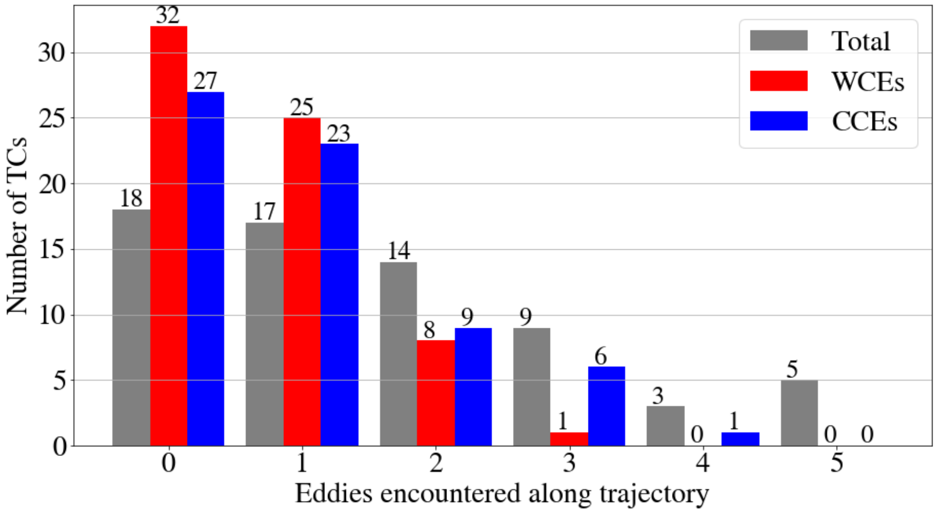

Figure B.8: Grouped bar chart showing the number of tropical cyclones that encounter n ocean eddies, where n = 0, 1, 2, 3, 4 and 5. The grey bars display the number of tropical cyclones that encounter a total of n ocean eddies, where n is a sum of the number of warm-core eddies (WCEs) and cold-core eddies (CCEs). The red and blue bars display the number of tropical cyclones that encounter a total of n WCEs and n CCEs, respectively. The exact numbers are displayed on top of each bar.

number of CCEs encountered than WCEs is in agreement with Ma et al. (2017), who focus on the Northwest Pacific. As shown in Figure B.8, 18 tropical cyclones encounter no ocean eddies. The remaining 48 tropical cyclones encounter at least one ocean eddy, of which 31 encounter two or more. Figure B.8 also displays the number of tropical-cyclone-eddy encounters for WCEs and CCEs separately. The number of tropical cyclones that encounter no WCEs is larger than the number of tropical cyclone that encounter no CCEs. Similarly, the number of tropical cyclones that encounter one WCE is larger than the number of tropical cyclone that encounter one CCE. The trend reverses for two encounters or more, where more tropical cyclones encounter CCEs than WCEs. The differing distribution for WCEs and CCEs reflects the larger number of CCEs than WCEs encountered across all tropical cyclones.

B.6 IMPACT OF OCEAN EDDIES ON TC INTENSITY

The large number of encounters between ocean eddies and tropical cyclones makes this simulation a rich data set that enables us to explore the impact of ocean eddies on tropical cyclone intensity. In the following, we examine this impact for warm-core eddies (WCEs) and cold core eddies (CCEs) separately. To determine whether WCEs have a statistically significant impact on tropical cyclone intensity, we divide the tropical cyclones into two groups: those that encounter at least one WCE before reaching peak intensity (warm-track tropical cyclones) and those that do not (not-warm-track tropical cyclones). Subsequently, we compare the average peak intensity for these two groups. To further understand the

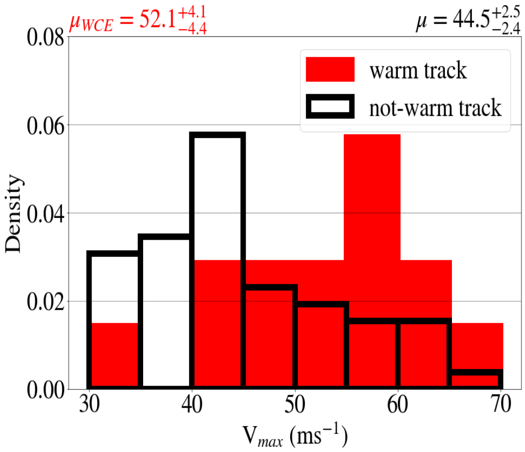

Figure B.9: Normalised histogram of the peak intensity, V_{max}, for warm-track and not-warm-track tropical cyclones. The mean for the warm-core-track tropical cyclones, μ_{WCE}, and not-warm-track tropical cyclones, μ, are given with their respective 95% confidence intervals.

effect of WCEs in terms of the negative feedback between tropical cyclone intensity and sea-surface cooling, we also analyse the surface latent heat flux and sea-surface cooling for each tropical cyclone averaged over all track points before the tropical cyclone reaches peak intensity. Finally, we repeat the same analysis for the CCEs, where the tropical cyclones are divided into those that encounter at least one CCE before reaching peak intensity (cold-track tropical cyclones) and those that do not (not-cold-track tropical cyclones).

B.6.1 *Warm-core eddies*

There are a total of 14 warm-track tropical cyclones. The distributions of peak intensity, V_{max}, for the warm-track and the remaining 52 not-warm-track tropical cyclones are shown as a normalised histogram in Figure B.9. Compared to the distribution for the not-warm-track tropical cyclones, the distribution for the warm-track tropical cyclones is shifted to the right. The rightward shift is evident from the peak in the distributions, which is located at the interval 55-60 ms^{-1} for the warm-track tropical cyclones compared to the lower 45-50 ms^{-1} for the not-warm-track tropical cyclones. As a result, the mean V_{max} is higher at 52.1 ms^{-1} for the warm-track tropical cyclones compared to 44.5 ms^{-1} for the not-warm-track tropical cyclones. The difference between the means is statistically significant at the 95% confidence level. The difference of 7.5 ms^{-1} between the two means is substantial, with the mean corresponding to category 3 for warm-track tropical cyclones but only category 2 for the not-warm-track tropical cyclones.

Figure B.10 a) displays the normalised histogram for the track-averaged surface latent heat flux before the tropical cyclone reaches peak intensity, $\overline{\mathrm{LHF}}$. Similar to the distributions of V_{max}, the distribution for the warm-track tropical cyclones is shifted to the right compared to the not-warm-track tropical cyclones. Again, the rightward shift is reflected in the peak and the mean of the distributions. The peak of the distribution for the warm-track tropical cyclones lies in the 750-1250 Wm^{-2} range compared to the peak in the lower 250-

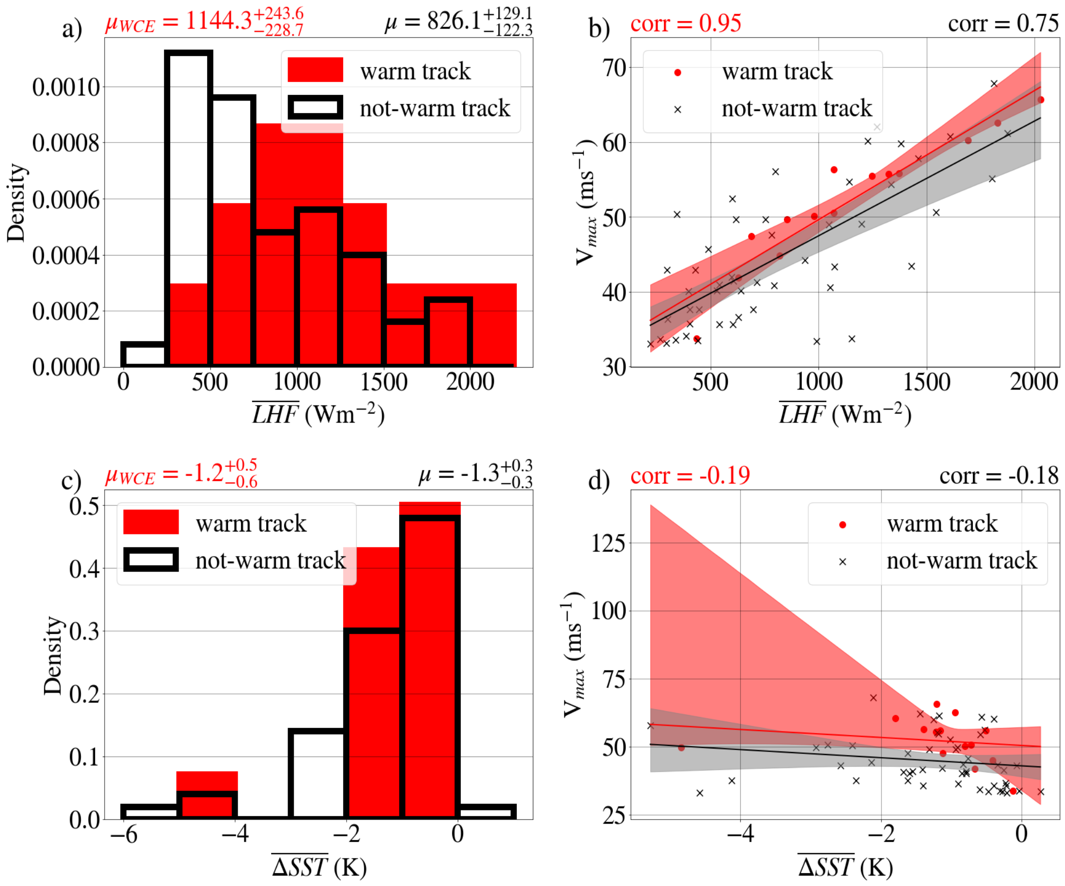

Figure B.10: Four panel plots comparing warm-track tropical cyclones with not-warm-track tropical cyclones. Panel a) is a histogram of the track-averaged surface latent heat flux, $\overline{\mathrm{LHF}}$. Panel b) is a scatter plot of the peak intensity, V_{max}, against $\overline{\mathrm{LHF}}$. Panel c) is a histogram of the track-averaged sea-surface cooling, $\overline{\Delta SST}$. Panel d) is a scatter plot of V_{max} against $\overline{\Delta SST}$. The correlation coefficients, lines of best fit and corresponding 95% confidence intervals are shown for the scatter plots. The means for the histograms are indicated at the top of panel a) and panel c).

500 Wm^{-2} range for the not-warm-track tropical cyclones. The mean $\overline{\mathrm{LHF}}$ is higher at 1147 Wm^{-2} for the warm-track tropical cyclones than the 826 Wm^{-2} for the not-warm-track tropical cyclones. Similar to V_{vmax}, the difference in the means is statistically significant at the 95% confidence level.

Figure B.10 b) shows a scatter plot of V_{max} against $\overline{\mathrm{LHF}}$ for each for the two groups. The warm-track tropical cyclones display a strong positive correlation of 0.95 compared with the weaker positive correlation of 0.75 for the not-warm-track tropical cyclones. The corresponding lines of best fit and their respective 95% confidence intervals are also shown in Figure B.10 b). For a given $\overline{\mathrm{LHF}}$, V_{max} is larger for the warm-track line of best fit than for the not-warm-track line of best fit. However, the confidence intervals overlap.

Figure B.10 c) shows the normalised histogram for the track-averaged change in SST before the tropical cyclone reaches peak intensity, $\overline{\Delta SST}$. The distributions are similar in

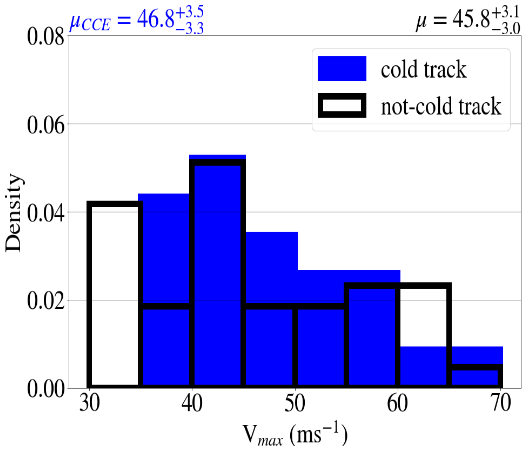

Figure B.11: Same as Figure B.9 but for cold-track and not-cold-track tropical cyclones.

appearance, with the most frequent cooling occurring bar between -1 K and 0 K and the second most frequent cooling occurring between -2 K and -1 K. For warm-track tropical cyclones, the mean $\overline{\Delta SST}$ is -1.2 K, which is slightly higher than the mean $\overline{\Delta SST}$ of -1.3 K for not-warm-track tropical cyclones. However, this difference is not statistically significant at the 95% confidence level.

Figure B.10 d) shows a scatter plot of V_{max} against $\overline{\Delta SST}$ for each of the two groups. Both warm-track and not-warm-track tropical cyclones display a similar weak negative correlation of -0.19 and -0.18 respectively. The corresponding lines of best fit and their respective 95% confidence intervals are also shown in Figure B.10 d). For a given $\overline{\Delta SST}$, V_{max} is larger for the warm-track line of best fit than for the not-warm-track line of best fit. Apart from an interval between approximately -1.5 K and 1.0 K, the confidence intervals overlap.

B.6.2 *Cold-core eddies*

There are a total of 23 cold-track tropical cyclones. The distributions of peak intensity, V_{max}, for the cold-track and the remaining 43 not-cold-track tropical cyclones are shown as a normalised histogram in Figure B.11. Both distributions peak in the range 40-45 ms^{-1}. The mean V_{max} for the cold-track tropical cyclones of 46.8 ms^{-1} is higher than the mean V_{max} of 45.8 ms^{-1} for the not-cold-track tropical cyclones. In contrast to the analysis of the warm-core eddies in the previous section, the difference between the mean V_{max} of both distributions is not statistically significant at the 95% confidence level.

Figure B.12 a) displays the normalised histogram for the track-averaged surface latent heat flux before the tropical cyclone reaches peak intensity, $\overline{\text{LHF}}$. Compared to the distribution for the not-cold-track tropical cyclones, the distribution for the cold-track tropical cyclones is skewed to the left. Correspondingly, the mean $\overline{\text{LHF}}$ is lower at 833 Wm^{-2} for the cold-track tropical cyclones compared to the mean $\overline{\text{LHF}}$ of 932.3 for the not-cold-track tropical cyclones. However, similar to V_{max}, the difference in the means is not statistically significant at the 95% confidence level.

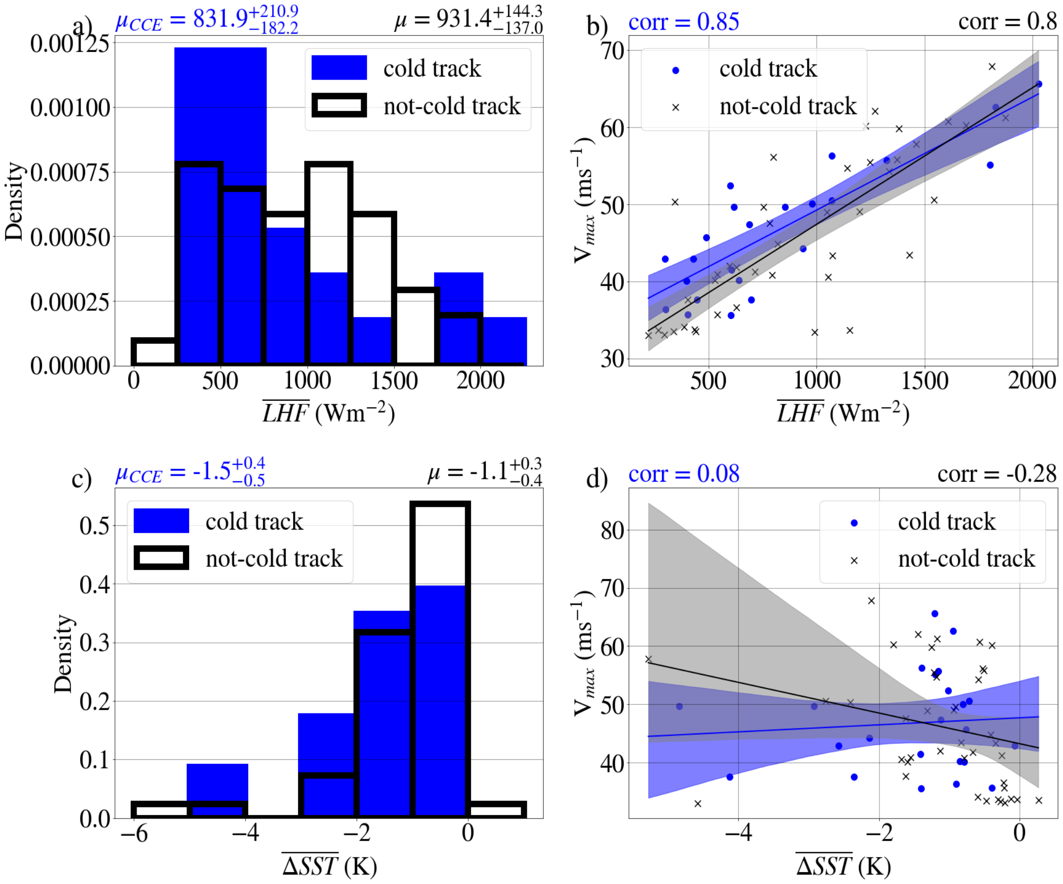

Figure B.12: Same as Figure B.10 but for cold-track and not-cold-track tropical cyclones.

Figure B.12 b) shows a scatter plot of V_{max} against $\overline{LHF}$ for each of the two groups. The cold-track tropical cyclones display a strong positive correlation of 0.85 compared with the weaker positive correlation of 0.8 for the not-cold-track tropical cyclones. The correlation for the cold-track tropical cyclones is less that the correlation for the warm-track tropical cyclones shown in Figure B.10 b). The corresponding lines of best fit and their respective 95% confidence intervals for the cold-track and not-cold-track tropical cyclones are also shown in Figure B.12 b). In contrast to the equivalent scatter plot for the warm-core eddy analysis, the lines of best fit intersect each other. Moreover, the overlap between the confidence intervals is larger compared to the same scatter plot for the warm-core eddy analysis.

Figure B.12 c) shows the normalised histogram for $\overline{\Delta SST}$. The distributions are similar in appearance, with the most frequent cooling occurring between -1 K and 0 K and the second most frequent cooling occurring between -2 K and -1 K. For cold-track tropical cyclones, the mean $\overline{\Delta SST}$ is -1.5 K, which is lower than the mean of -1.1 K for not-cold-track tropical cyclones. However, similar to the warm-core eddy analysis, this difference is not statistically significant at the 95% confidence level.

Figure B.12 d) shows a scatter plot of V_{max} against $\overline{\Delta SST}$ for each of the two groups. While not-cold-track tropical cyclones have a weak negative correlation of -0.28, the cold-track tropical cyclones have a negligible positive correlation of 0.08. The large difference between the gradients of the lines of best fit reflects the large scatter of both the cold-track and not-cold-track data points. In addition, the lines of best fit intersect and the confidence intervals overlap to a greater extent compared to the equivalent plot for the warm-core eddy analysis.

B.6.3 *Discussion*

The above results indicate that WCEs have a substantial impact on peak intensity on a global scale. The warm-track tropical cyclones reach on average a higher peak intensity than the not-warm-track tropical cyclones. Despite reaching a higher peak intensity, warm-track tropical cyclones experience a similar average sea-surface cooling prior to reaching peak intensity compared to not-warm-track tropical cyclones. This discrepancy suggests that WCEs are suppressing sea-surface cooling, which in turn sustains the larger average surface latent heat flux experienced on average by warm-track tropical cyclones.

The results also point to tropical cyclones that encounter WCEs requiring a smaller surface latent heat flux to achieve the same peak intensity. The reason may be that warm-track tropical cyclones intensify more rapidly and then reach peak intensity shortly after crossing the WCE due to the ensuing sea-surface cooling. Conversely, tropical cyclones that intensify more slowly may experience a larger surface latent heat flux for a longer period of time before they reach peak intensity, corresponding to a larger average surface latent heat flux compared to warm-track tropical cyclones.

In contrast to WCEs, CCEs do not have a statistically significant impact on the average peak intensity. Taken together with the lack of a statistically significant difference between the means for the average surface latent heat flux and the sea-surface cooling, it is not clear how cold-core eddies affect peak intensity. The lack of statistical significance may be due to the cold-track tropical cyclones also encountering WCEs, resulting in a large spread of peak intensities. These results suggest that CCEs have a weaker effect on average peak intensity compared to WCEs and that CCEs may be of secondary importance for peak intensity.

B.7 SUMMARY AND CONCLUSION

We conduct the first study on the impact of ocean eddies on tropical cyclone intensity on a global scale. To this end, we analyse a one year, global coupled atmosphere-ocean simulation run with the ICON model with a horizontal grid spacing of 5 km. Spinning up the ocean prior to coupling with the atmosphere leads to the formation of warm-core eddies and cold-core eddies, as well as other oceanic features, such as boundary currents.

The tropical cyclones in the one-year global simulation display reasonable tropical cyclone climatology in line with observations. With the exception of the North Indian Ocean, tropical cyclones are simulated in all ocean basins where they typically occur. Although the number of tropical cyclones that are category 1 or stronger exceeds the record count, the 24 major tropical cyclones (category 3 - 5) simulated is close to the mean number of 23.4 for the period from 1981 to 2010. The monthly variation in tropical cyclone frequency reflects the climatological asymmetry between the Northern and Southern Hemisphere, with a large peak in the August and a smaller peak in March. The pressure-wind relationship displays a typical negative correlation, although the model tends to simulate tropical cyclones with a lower central mean sea-level pressure compared to observations. The simulated strengthening of sea-surface cooling with increasing category is also is in line with observations. The ability of the model to simulate a reasonable tropical cyclone climatology provides confidence in the suitability of the simulation to study the impact of ocean eddies on tropical cyclone intensity.

To investigate the impact of the warm-core and cold-core eddies on tropical cyclone intensity, we focus on the peak intensity reached by the simulated tropical cyclones. For the analysis of the warm-core eddies, we divide the tropical cyclones into those that encounter at least one warm-core eddy prior to reaching peak intensity and those that do not. We proceed by examining the track-averaged surface latent heat flux and sea-surface cooling from the initial detection up to the time of peak intensity. We then repeat this analysis for the cold-core eddies.

Our results indicate that warm-core eddies have a substantial impact on the peak intensity attained by the simulated tropical cyclones. The tropical cyclones that encounter at least one warm-core eddy prior to reaching peak intensity reach an average peak intensity corresponding to category 3. By contrast, those tropical cyclones that do not encounter any warm-core eddies prior to peak intensity attain an average peak intensity equivalent to category 2. The higher average peak intensity of the tropical cyclones that encounter warm-core eddies is associated with a higher mean track-averaged surface latent heat flux but a similar mean track-averaged sea-surface cooling. This result is consistent with warm-core eddies sustaining large surface latent heat flux by suppressing sea-surface cooling. Moreover, the relationship between the peak intensity and track-averaged surface latent heat flux suggest that warm-core eddies may result in tropical cyclones to intensify and reach peak intensity sooner compared to the case where the tropical cyclones does not encounter any warm-core eddies.

In contrast to warm-core eddies, we find that cold-core eddies do not have a clear impact on average peak intensity. When a tropical cyclone encounters both a cold-core eddy and warm-core eddy prior to peak intensity, the effect of the former may be masked by the effect of the latter. Given the lack of a robust signal, cold-core eddies may be of secondary importance for peak intensity on a global scale as opposed to warm-core eddies.

Finally, our results are relevant for future projections of tropical cyclone intensity. Although most future projections predict an increase in the global proportion of intense tropical cyclones (category 4 and 5), they are based on global climate simulations that do not resolve ocean eddies (Knutson et al., 2020). Given that our results point to a substantial impact of warm-core on tropical cyclone intensity on a global scale, the lack of eddy resolving climate simulation may introduce a bias in future projections of tropical cyclone intensity.

B.8 ACKNOWLEDGEMENTS

The authors would like to thank the members of the Sapphire team at the Max Planck Institute for Meteorology for providing the ICON simulation data. The simulation itself would not have been possible without the substantial computing power provided by the Mistral High Performance Computing system maintained by the German Climate Computing Centre (DKRZ).

BIBLIOGRAPHY

Abarca, S. F., M. T. Montgomery, and J. C. McWilliams (2015). "The azimuthally averaged boundary layer structure of a numerically simulated major hurricane." In: *Journal of Advances in Modeling Earth Systems* 7.3, pp. 1207–1219. ISSN: 19422466. DOI: 10.1002/2015MS000457. URL: http://doi.wiley.com/10.1002/2015MS000457.

Alam, E. and D. Dominey-Howes (May 2015). "A new catalogue of tropical cyclones of the northern Bay of Bengal and the distribution and effects of selected landfalling events in Bangladesh." In: *International Journal of Climatology* 35 (6). or example, just 5 of global tropical cyclones originate in the Bay of Bengal, but adjacent countries including Bangladesh, India and Myanmar (Figure 1) experience more than 75 of the global casualties (Chowdhury, 2002).<br/>Bangladesh alone experiences about 50 of all global casualties, even though it is only affected by about 1 of all annual tropical cyclones (Ali, 1999)<br/>Table 1 has list of reasons cited for death<br/>, pp. 801–835. ISSN: 08998418. DOI: 10.1002/joc.4035. URL: https://onlinelibrary.wiley.com/doi/10.1002/joc.4035.

Ali, A. (Aug. 1999). "Climate change impacts and adaptation assessment in Bangladesh." In: *Climate Research* 12 (2-3 SPEC. ISS. 6), pp. 109–116. ISSN: 0936577X. DOI: 10.3354/cr012109. URL: https://ui.adsabs.harvard.edu/abs/1999ClRes..12..109A/abstract.

Ali, M. M., P. S. V Jagadeesh, and S. Jain (Feb. 2007). "Effects of eddies on Bay of Bengal cyclone intensity." In: *Eos, Transactions American Geophysical Union* 88 (8), pp. 93–95. ISSN: 00963941. DOI: 10.1029/2007EO080001. URL: http://doi.wiley.com/10.1029/2007EO080001.

Bacmeister, J. T., K. A. Reed, C. Hannay, P. Lawrence, S. Bates, J. E. Truesdale, N. Rosenbloom, and M. Levy (Feb. 2018). "Projected changes in tropical cyclone activity under future warming scenarios using a high-resolution climate model." In: *Climatic Change* 146 (3-4), pp. 547–560. ISSN: 15731480. DOI: 10.1007/s10584-016-1750-x. URL: https://link.springer.com/article/10.1007/s10584-016-1750-x.

Balaguru, K., G. R. Foltz, L. R. Leung, S. M. Hagos, and D. R. Judi (2018). "On the use of ocean dynamic temperature for hurricane intensity forecasting." In: *Weather and Forecasting* 33.2, pp. 411–418. ISSN: 15200434. DOI: 10.1175/waf-d-17-0143.1.

Bao, J. W., S. G. Gopalakrishnan, S. A. Michelson, F. D. Marks, and M. T. Montgomery (Oct. 2012). "Impact of physics representations in the HWRFX on simulated hurricane structure and pressure-wind relationships." In: *Monthly Weather Review* 140 (10), pp. 3278–3299. ISSN: 00270644. DOI: 10.1175/MWR-D-11-00332.1. URL: http://www.hfip.org/.

Bauer, P., A. Thorpe, and G. Brunet (Sept. 2015). *The quiet revolution of numerical weather prediction*. DOI: 10.1038/nature14956. URL: https://www.nature.com/articles/nature14956.

Bender, M. A., I. Ginis, and Y. Kurihara (1993). "Numerical simulations of tropical cyclone-ocean interaction with a high-resolution coupled model." In: *Journal of Geophysical Research* 98.D12, pp. 23245–23263. ISSN: 01480227. DOI: 10.1029/93jd02370.

Bender, M. A. and I. Ginis (2000). “Real-Case Simulations of Hurricane–Ocean Interaction Using A High-Resolution Coupled Model: Effects on Hurricane Intensity.” In: *http://dx.doi.org/10.1175/1520-0493(2000)128<0917:RCSOHO>2.0.CO;2* 128.4, pp. 917–946. DOI: `10.1175/1520-0493(2000)128<0917:RCSOHO>2.0.CO;2`.

Bender, M. A., I. Ginis, R. Tuleya, B. Thomas, and T. Marchok (Dec. 2007). “The operational GFDL coupled Hurricane-Ocean prediction system and a summary of its performance.” In: *Monthly Weather Review* 135 (12), pp. 3965–3989. ISSN: 00270644. DOI: `10.1175/2007MWR2032.1`. URL: `https://journals.ametsoc.org/view/journals/mwre/135/12/2007mwr2032.1.xml`.

Bender, M. A., T. R. Knutson, R. E. Tuleya, J. J. Sirutis, G. A. Vecchi, S. T. Garner, and I. M. Held (Jan. 2010). “Modeled impact of anthropogenic warming on the frequency of intense Atlantic hurricanes.” In: *Science* 327 (5964), pp. 454–458. ISSN: 00368075. DOI: `10.1126/science.1180568`. URL: `https://www.science.org/doi/10.1126/science.1180568`.

Bhatia, K., G. Vecchi, H. Murakami, S. Underwood, and J. Kossin (Oct. 2018). “Projected response of tropical cyclone intensity and intensification in a global climate model.” In: *Journal of Climate* 31 (20), pp. 8281–8303. ISSN: 08948755. DOI: `10.1175/JCLI-D-17-0898.1`. URL: `www.ametsoc.org/PUBSReuseLicenses`.

Black, P. G., E. A. D’Asaro, W. M. Drennan, J. R. French, P. P. Niiler, T. B. Sanford, E. J. Terrill, E. J. Walsh, and J. A. Zhang (2007). “Air-sea exchange in hurricanes: Synthesis of observations from the coupled boundary layer air-sea transfer experiment.” In: *Bulletin of the American Meteorological Society* 88.3, pp. 357–374. ISSN: 00030007. DOI: `10.1175/BAMS-88-3-357`.

Brokaw, R. J., B. Subrahmanyam, C. B. Trott, and A. Chaigneau (Feb. 2020). “Eddy Surface Characteristics and Vertical Structure in the Gulf of Mexico from Satellite Observations and Model Simulations.” In: *Journal of Geophysical Research: Oceans* 125 (2), e2019JC015538. ISSN: 2169-9275. DOI: `10.1029/2019JC015538`. URL: `https://onlinelibrary.wiley.com/doi/10.1029/2019JC015538`.

Bryan, G. H. and R. Rotunno (2009). “The Maximum Intensity of Tropical Cyclones in Axisymmetric Numerical Model Simulations.” In: *Monthly Weather Review* 137.6, pp. 1770–1789. ISSN: 0027-0644. DOI: `10.1175/2008MWR2709.1`. URL: `http://journals.ametsoc.org/doi/10.1175/2008MWR2709.1`.

Bu, Y. P., R. G. Fovell, and K. L. Corbosiero (Apr. 2017). “The influences of boundary layer mixing and cloud-radiative forcing on tropical cyclone size.” In: *Journal of the Atmospheric Sciences* 74 (4), pp. 1273–1292. ISSN: 15200469. DOI: `10.1175/JAS-D-16-0231.1`. URL: `www.ametsoc.org/PUBSReuseLicenses`.

Camargo, S. J. (Dec. 2013). “Global and regional aspects of tropical cyclone activity in the CMIP5 models.” In: *Journal of Climate* 26 (24), pp. 9880–9902. ISSN: 08948755. DOI: `10.1175/JCLI-D-12-00549.1`. URL: `http://www.ec.gc.ca`.

Camargo, S. J., M. C. Wheeler, and A. H. Sobel (Oct. 2009). “Diagnosis of the MJO modulation of tropical cyclogenesis using an empirical index.” In: *Journal of the Atmospheric Sciences* 66 (10), pp. 3061–3074. ISSN: 00224928. DOI: `10.1175/2009JAS3101.1`. URL: `https://journals.ametsoc.org/view/journals/atsc/66/10/2009jas3101.1.xml`.

Camargo, S. J. and A. A. Wing (Mar. 2016). "Tropical cyclones in climate models." In: *WIREs Climate Change* 7 (2), pp. 211–237. ISSN: 1757-7780. DOI: `10.1002/wcc.373`. URL: `https://onlinelibrary.wiley.com/doi/10.1002/wcc.373`.

Chaigneau, A., A. Gizolme, and C. Grados (Oct. 2008). "Mesoscale eddies off Peru in altimeter records: Identification algorithms and eddy spatio-temporal patterns." In: *Progress in Oceanography* 79 (2-4), pp. 106–119. ISSN: 00796611. DOI: `10.1016/j.pocean.2008.10.013`.

Chang, S. W. and R. A. Anthes (1978). "Numerical Simulations of the Ocean's Nonlinear, Baroclinic Response to Translating hurricanes." In: *Journal of Physical Oceanography* 8.3, pp. 468–480. DOI: `10.1175/1520-0485(1978)008<0468:NSOTON>2.0.CO;2`.

Chang, S. W. and R. A. Anthes (1979). "The Mutual Response of the Tropical Cyclone and the Ocean." In: *Journal of Physical Oceanography* 9.1, pp. 128–135. ISSN: 0022-3670. DOI: `10.1175/1520-0485(1979)009<0128:tmrott>2.0.co;2`.

Chelton, D. B., M. G. Schlax, and R. M. Samelson (Oct. 2011). "Global observations of nonlinear mesoscale eddies." In: *Progress in Oceanography* 91 (2), pp. 167–216. ISSN: 00796611. DOI: `10.1016/j.pocean.2011.01.002`.

Chelton, D. B., M. G. Schlax, R. M. Samelson, and R. A. de Szoeke (Aug. 2007). "Global observations of large oceanic eddies." In: *Geophysical Research Letters* 34 (15). ISSN: 00948276. DOI: `10.1029/2007GL030812`. URL: `http://doi.wiley.com/10.1029/2007GL030812`.

Chen, S., T. J. Campbell, H. Jin, S. Gaberšek, R. M. Hodur, and P. Martin (2010a). "Effect of Two-Way Air-Sea Coupling in High and Low Wind Speed Regimes." In: *Monthly Weather Review* 138.9, pp. 3579–3602. DOI: `10.1175/2009mwr3119.1`. URL: `https://doi.org/10.1175%2F2009mwr3119.1`.

Chen, S., T. J. Campbell, H. Jin, S. Gaberšek, R. M. Hodur, and P. Martin (2010b). "Effect of two-way air-sea coupling in high and low wind speed regimes." In: *Monthly Weather Review* 138.9, pp. 3579–3602. ISSN: 00270644. DOI: `10.1175/2009MWR3119.1`.

Chen, S., R. L. Elsberry, and P. A. Harr (2017). "Modeling Interaction of a Tropical Cyclone with Its Cold Wake." In: *Journal of the Atmospheric Sciences* 74.12, pp. 3981–4001. ISSN: 0022-4928. DOI: `10.1175/JAS-D-16-0246.1`.

Christensen, J. H. et al. (Jan. 2013). *Climate phenomena and their relevance for future regional climate change*. DOI: `10.1017/CBO9781107415324.028`. URL: `https://yonsei.pure.elsevier.com/en/publications/climate-phenomena-and-their-relevance-for-future-regional-climate`.

Cione, J. J. and E. W. Uhlhorn (2003). "Sea Surface Temperature Variability in Hurricanes: Implications with Respect to Intensity Change." In: *Monthly Weather Review* 131.8, pp. 1783–1796. DOI: `10.1175//2562.1`.

DeMaria, M., J. L. Franklin, M. J. Onderlinde, and J. Kaplan (May 2021). "Operational Forecasting of Tropical Cyclone Rapid Intensification at the National Hurricane Center." In: *Atmosphere* 12 (6), p. 683. ISSN: 2073-4433. DOI: `10.3390/atmos12060683`. URL: `https://www.mdpi.com/2073-4433/12/6/683`.

DeMaria, M., C. R. Sampson, J. A. Knaff, and K. D. Musgrave (2014). "Is Tropical Cyclone Intensity Guidance Improving?" In: *Bulletin of the American Meteorological Society* 95.3, pp. 387–398. DOI: `10.1175/BAMS-D-12-00240.1`. eprint: `https://doi.org/10.1175/BAMS-D-12-00240.1`. URL: `https://doi.org/10.1175/BAMS-D-12-00240.1`.

Dee, D. P. et al. (2011). "The ERA-Interim reanalysis: configuration and performance of the data assimilation system." In: *Quarterly Journal of the Royal Meteorological Society* 137.656, pp. 553–597. doi: `https://doi.org/10.1002/qj.828`. eprint: `https://rmets.onlinelibrary.wiley.com/doi/pdf/10.1002/qj.828`. url: `https://rmets.onlinelibrary.wiley.com/doi/abs/10.1002/qj.828`.

Demaria, M. and J. Kaplan (June 1994). "A statistical hurricane intensity prediction scheme (SHIPS) for the Atlantic Basin." In: *Weather Forecasting* 9 (2), pp. 209–220. issn: 0882-8156. doi: `10.1175/1520-0434(1994)009<0209:ASHIPS>2.0.CO;2`. url: `https://journals.ametsoc.org/view/journals/wefo/9/2/1520-0434_1994_009_0209_aships_2_0_co_2.xml`.

Emanuel, K. A. (1986). "An Air-Sea Interaction Theory for Tropical Cyclones. Part I: Steady-State Maintenance." In: *Journal of the Atmospheric Sciences* 43.6, pp. 585–605. issn: 0022-4928. doi: `10.1175/1520-0469(1986)043<0585:AASITF>2.0.CO;2`.

Emanuel, K. A. (2013). "Downscaling CMIP5 climate models shows increased tropical cyclone activity over the 21st century." In: *Proceedings of the National Academy of Sciences of the United States of America* 110.30, pp. 12219–12224.

Emanuel, K. A. (1995). "Sensitivity of Tropical Cyclones to Surface Exchange Coefficients and a Revised Steady-State Model incorporating Eye Dynamics." In: *Journal of the Atmospheric Sciences* 52.22, pp. 3969–3976. issn: 0022-4928. doi: `10.1175/1520-0469(1995)052<3969:SOTCTS>2.0.CO;2`.

Emanuel, K. A. (1997). "Some Aspects of Hurricane Inner-Core Dynamics and Energetics." In: *Journal of the Atmospheric Sciences* 54.8, pp. 1014–1026. doi: `10.1175/1520-0469(1997)054<1014:SAOHIC>2.0.CO;2`.

Emanuel, K. A. (1989). "The Finite-Amplitude Nature of Tropical Cyclogenesis." In: *Journal of the Atmospheric Sciences* 46.22, pp. 3431–3456. issn: 0022-4928. doi: `10.1175/1520-0469(1989)046<3431:TFANOT>2.0.CO;2`.

Emanuel, K. A. (1999). "Thermodynamic control of hurricane intensity." In: *Nature* 401, pp. 665–669. issn: 00280836. doi: `10.1038/44326`.

Emanuel, K. (2005). *Divine Wind*. Oxford University Press. isbn: 9780195149418.

Fierro, A. O., R. F. Rogers, F. D. Marks, and D. S. Nolan (2009). "The Impact of Horizontal Grid Spacing on the Microphysical and Kinematic Structures of Strong Tropical Cyclones Simulated with the WRF-ARW Model." In: *Monthly Weather Review* 137.11, pp. 3717–3743. doi: `10.1175/2009mwr2946.1`. url: `https://doi.org/10.1175%2F2009mwr2946.1`.

Frank, N. L. and S. A. Husain (June 1971). "The Deadliest Tropical Cyclone in History." In: *Bulletin of the American Meteorological Society* 52 (6). Detailed acount of East Pakistan TC of 1970<br/>Death toll and damage to crops and houses<br/>Bangladesh particuarlyl vulnerable to storm surge due to high astronomical tide (20ft storm surge in 1970)<br/>Difficulty in communicating danger - reserve most severe warning for most severe TCs<br/>, pp. 438–445. issn: 0003-0007. doi: `10.1175/1520-0477(1971)052<0438:tdtcih>2.0.co;2`. url: `https://journals.ametsoc.org/view/journals/bams/52/6/1520-0477_1971_052_0438_tdtcih_2_0_co_2.xml`.

Frank, W. M. and E. A. Ritchie (2001). "Effects of Vertical Wind Shear on the Intensity and Structure of Numerically Simulated Hurricanes." In: *Monthly Weather Review* 129.9, pp. 2249–2269. ISSN: 0027-0644. DOI: 10.1175/1520-0493(2001)129<2249:EOVWSO>2.0.CO;2.

Gaspar, P., Y. Grégoris, and J.-M. Lefevre (1990). "A simple eddy kinetic energy model for simulations of the oceanic vertical mixing: Tests at station Papa and long-term upper ocean study site." In: *Journal of Geophysical Research: Oceans* 95.C9, pp. 16179–16193. DOI: https://doi.org/10.1029/JC095iC09p16179. eprint: https://agupubs.onlinelibrary.wiley.com/doi/pdf/10.1029/JC095iC09p16179. URL: https://agupubs.onlinelibrary.wiley.com/doi/abs/10.1029/JC095iC09p16179.

Gill, A. E. (1984). "On the Behavior of Internal Waves in the Wakes of Storms." In: *Journal of Physical Oceanography* 14, pp. 1129–1151.

Giorgetta, M. A. et al. (2018). "ICON-A, the Atmosphere Component of the ICON Earth System Model: I. Model Description." In: *Journal of Advances in Modeling Earth Systems* 10.7, pp. 1613–1637. ISSN: 19422466. DOI: 10.1029/2017MS001242.

Gopalakrishnan, S. et al. (2021). *2020 HFIP RD Activities Summary: Recent Results and Operational Implementation*. United States. National Oceanic, Atmospheric Administration. Office of Oceanic, and Atmospheric Research.;National Weather Service (U.S.) DOI: 10.25923/718E-6232. URL: https://repository.library.noaa.gov/view/noaa/31443.

Gopalakrishnan, S. G., F. Marks, J. A. Zhang, X. Zhang, J.-W. Bao, and V. Tallapragada (2013). "A Study of the Impacts of Vertical Diffusion on the Structure and Intensity of the Tropical Cyclones Using the High-Resolution HWRF System." In: *Journal of the Atmospheric Sciences* 70.2, pp. 524 –541. DOI: 10.1175/JAS-D-11-0340.1. URL: https://journals.ametsoc.org/view/journals/atsc/70/2/jas-d-11-0340.1.xml.

Gray, W. M. (1975). "Tropical cyclone genesis." PhD thesis. Colorado State University. Libraries.

Guo, T., Y. Sun, L. Liu, and Z. Zhong (2020). "The Impact of Storm-Induced SST Cooling on Storm Size and Destructiveness: Results from Atmosphere-Ocean Coupled Simulations." In: *Journal of Meteorological Research* 34.5, pp. 1068–1081. DOI: 10.1007/s13351-020-0001-2. URL: https://doi.org/10.1007%2Fs13351-020-0001-2.

Hellin, J., M. Haigh, and F. Marks (May 1999). "Rainfall characteristics of hurricane mitch." In: *Nature* 399 (6734), p. 316. ISSN: 00280836. DOI: 10.1038/20577. URL: www.nature.com.

Hong, X., S. W. Chang, S. Raman, L. K. Shay, and R. Hodur (2000). "The Interaction between Hurricane Opal (1995) and a Warm Core Ring in the Gulf of Mexico." In: *Monthly Weather Review* 128.5, pp. 1347–1365. DOI: 10.1175/1520-0493(2000)128<1347:tibhoa>2.0.co;2. URL: https://doi.org/10.1175%2F1520-0493%282000%29128%3C1347%3Atibhoa%3E2.0.co%3B2.

Horn, M. et al. (Dec. 2014). "Tracking scheme dependence of simulated tropical cyclone response to idealized climate simulations." In: *Journal of Climate* 27 (24), pp. 9197–9213. ISSN: 08948755. DOI: 10.1175/JCLI-D-14-00200.1. URL: http://www.usclivar.org/.

Houze, R. A. (2010). "Clouds in tropical cyclones." In: *Monthly Weather Review* 138.2, pp. 293–344. ISSN: 00270644. DOI: 10.1175/2009MWR2989.1.

Jaimes, B. and L. K. Shay (2009a). "Mixed Layer Cooling in Mesoscale Oceanic Eddies during Hurricanes Katrina and Rita." In: *Monthly Weather Review* 137.12, pp. 4188–4207. DOI: 10.1175/2009MWR2849.1. eprint: https://doi.org/10.1175/2009MWR2849.1. URL: https://doi.org/10.1175/2009MWR2849.1.

Jaimes, B. and L. K. Shay (2009b). “Mixed Layer Cooling in Mesoscale Oceanic Eddies during Hurricanes Katrina and Rita.” In: *Monthly Weather Review* 137.12, pp. 4188–4207. DOI: 10.1175/2009MWR2849.1.

Jaimes, B., L. K. Shay, and J. K. Brewster (2016). “Observed air-sea interactions in tropical cyclone Isaac over Loop Current mesoscale eddy features.” In: *Dynamics of Atmospheres and Oceans* 76.The Loop Current Dynamics Experiment, pp. 306–324. ISSN: 03770265. DOI: 10.1016/j.dynatmoce.2016.03.001.

Jaimes, B., L. K. Shay, and G. R. Halliwell (Oct. 2011). “The Response of Quasigeostrophic Oceanic Vortices to Tropical Cyclone Forcing.” In: *Journal of Physical Oceanography* 41 (10). SST cooling depends on whether eddy is cyclonic or anticyclonic <br/><br/>Rotation rate of eddy proportional to vertical mixing and shear<br/><br/><br/>Good point to see other references and see which papers cited this work, pp. 1965–1985. ISSN: 0022-3670. DOI: 10.1175/JPO-D-11-06.1. URL: http://journals.ametsoc.org/doi/10.1175/JPO-D-11-06.1.

Jaimes, B., L. K. Shay, and E. W. Uhlhorn (2015). “Enthalpy and Momentum Fluxes during Hurricane Earl Relative to Underlying Ocean Features.” In: *Monthly Weather Review* 143.1, pp. 111–131. ISSN: 0027-0644. DOI: 10.1175/MWR-D-13-00277.1.

Jaimes, B., L. K. Shay, J. B. Wadler, and J. E. Rudzin (2021). “On the Hyperbolicity of the Bulk Air-Sea Heat Flux Functions: Insights into the Efficiency of Air-Sea Moisture Disequilibrium for Tropical Cyclone Intensification.” In: *Monthly Weather Review* 149.5, pp. 1517–1534. DOI: 10.1175/mwr-d-20-0324.1. URL: https://doi.org/10.1175%2Fmwr-d-20-0324.1.

Jayne, S. R., D. Roemmich, N. Zilberman, S. C. Riser, K. S. Johnson, G. C. Johnson, and S. R. Piotrowicz (June 2017). “The Argo Program: Present and Future.” In: *Oceanography* 30 (2), pp. 18–28.

Kafatos, M., D. Sun, R. Gautam, Z. Boybeyi, R. Yang, and G. Cervone (Sept. 2006). “Role of anomalous warm gulf waters in the intensification of Hurricane Katrina.” In: *Geophysical Research Letters* 33 (17), p. L17802. ISSN: 0094-8276. DOI: 10.1029/2006GL026623. URL: http://doi.wiley.com/10.1029/2006GL026623.

Kaplan, J. and M. DeMaria (2003). “Large-Scale Characteristics of Rapidly Intensifying Tropical Cyclones in the North Atlantic Basin.” In: *Weather and Forecasting* 18.6, pp. 1093–1108. ISSN: 0882-8156. DOI: 10.1175/1520-0434(2003)018<1093:lcorit>2.0.co;2.

Karim, M. F. and N. Mimura (Aug. 2008). “Impacts of climate change and sea-level rise on cyclonic storm surge floods in Bangladesh.” In: *Global Environmental Change* 18 (3), pp. 490–500. ISSN: 09593780. DOI: 10.1016/j.gloenvcha.2008.05.002.

Kepert, J. D. (May 2012). “Choosing a boundary layer parameterization for tropical cyclone modeling.” In: *Monthly Weather Review* 140 (5), pp. 1427–1445. ISSN: 00270644. DOI: 10.1175/MWR-D-11-00217.1. URL: https://journals.ametsoc.org/view/journals/mwre/140/5/mwr-d-11-00217.1.xml.

Kepert, J. D. (2010). “Slab- and height-resolving models of the tropical cyclone boundary layer. Part I: Comparing the simulations.” In: *Quarterly Journal of the Royal Meteorological Society* 136.652, pp. 1686–1699. DOI: https://doi.org/10.1002/qj.667. eprint: https://rmets.onlinelibrary.wiley.com/doi/pdf/10.1002/qj.667. URL: https://rmets.onlinelibrary.wiley.com/doi/abs/10.1002/qj.667.

Khain, A. and I. Ginis (1991). "The mutual response of a moving tropical cyclone and the ocean." In: *Contributions to atmospheric physics* 64, pp. 125–141. ISSN: 0303-4186.

Kilroy, G., R. K. Smith, and M. T. Montgomery (2016). "Why Do Model Tropical Cyclones Grow Progressively in Size and Decay in Intensity after Reaching Maturity?" In: *Journal of the Atmospheric Sciences* 73.2, pp. 487–503. ISSN: 0022-4928. DOI: 10.1175/JAS-D-15-0157.1.

Kim, H. S., G. A. Vecchi, T. R. Knutson, W. G. Anderson, T. L. Delworth, A. Rosati, F. Zeng, and M. Zhao (Nov. 2014). "Tropical cyclone simulation and response to CO2 doubling in the GFDL CM2.5 high-resolution coupled climate model." In: *Journal of Climate* 27 (21), pp. 8034–8054. ISSN: 08948755. DOI: 10.1175/JCLI-D-13-00475.1. URL: https://journals.ametsoc.org/view/journals/clim/27/21/jcli-d-13-00475.1.xml.

Kirtman, B. P. et al. (Sept. 2012). "Impact of ocean model resolution on CCSM climate simulations." In: *Climate Dynamics* 39 (6), pp. 1303–1328. ISSN: 09307575. DOI: 10.1007/s00382-012-1500-3. URL: https://link.springer.com/article/10.1007/s00382-012-1500-3.

Klemp, J. B. (Jan. 2006). "Advances in the WRF model for convection-resolving forecasting." In: *Advances in Geosciences* 7, pp. 25–29. ISSN: 16807359. DOI: 10.5194/adgeo-7-25-2006.

Klotzbach, P. J. (Mar. 2014). "The madden-julian oscillation's impacts on worldwide tropical cyclone activity." In: *Journal of Climate* 27 (6), pp. 2317–2330. ISSN: 08948755. DOI: 10.1175/JCLI-D-13-00483.1. URL: http://apps.ecmwf.int/.

Klotzbach, P. J. and E. C. Oliver (May 2015). "Variations in global tropical cyclone activity and the Madden-Julian Oscillation since the midtwentieth century." In: *Geophysical Research Letters* 42 (10), pp. 4199–4207. ISSN: 19448007. DOI: 10.1002/2015GL063966. URL: https://onlinelibrary.wiley.com/doi/full/10.1002/2015GL063966https://onlinelibrary.wiley.com/doi/abs/10.1002/2015GL063966https://agupubs.onlinelibrary.wiley.com/doi/10.1002/2015GL063966.

Knutson, T. R., J. J. Sirutis, G. A. Vecchi, S. Garner, M. Zhao, H. S. Kim, M. Bender, R. E. Tuleya, I. M. Held, and G. Villarini (Sept. 2013). "Dynamical downscaling projections of twenty-first-century atlantic hurricane activity: CMIP3 and CMIP5 model-based scenarios." In: *Journal of Climate* 26 (17), pp. 6591–6617. ISSN: 08948755. DOI: 10.1175/JCLI-D-12-00539.1. URL: https://journals.ametsoc.org/view/journals/clim/26/17/jcli-d-12-00539.1.xml.

Knutson, T. R., J. J. Sirutis, M. Zhao, R. E. Tuleya, M. Bender, G. A. Vecchi, G. Villarini, and D. Chavas (Sept. 2015). "Global projections of intense tropical cyclone activity for the late twenty-first century from dynamical downscaling of CMIP5/RCP4.5 scenarios." In: *Journal of Climate* 28 (18), pp. 7203–7224. ISSN: 08948755. DOI: 10.1175/JCLI-D-15-0129.1. URL: https://journals.ametsoc.org/view/journals/clim/28/18/jcli-d-15-0129.1.xml.

Knutson, T. et al. (Oct. 2019). "Tropical cyclones and climate change assessment: Part I: Detection and attribution." In: *Bulletin of the American Meteorological Society* 100 (10), pp. 1987–2007. ISSN: 00030007. DOI: 10.1175/BAMS-D-18-0189.1. URL: https://en.wikipedia.org/wiki/Saffir-Simpson.

Knutson, T. et al. (Mar. 2020). "Tropical cyclones and climate change assessment part II: Projected response to anthropogenic warming." In: *Bulletin of the American Meteorolog-*

ical Society 101 (3), E303–E322. ISSN: 00030007. DOI: 10.1175/BAMS-D-18-0194.1. URL: https://doi.org/10.1175/BAMS-D-18-0194.1.

Korn, P. (2017). "Formulation of an unstructured grid model for global ocean dynamics." In: *Journal of Computational Physics* 339, pp. 525–552. ISSN: 00219991. DOI: 10.1016/j.jcp.2017.03.009.

Kumar, A. U., N. Brüggemann, and J. Marotzke (2022). *The impact of ocean eddies on tropical cyclone intensity in a one-year, global coupled atmosphere-ocean simulation (in preparation).*

Kumar, A. U., N. Brüggemann, R. K. Smith, and J. Marotzke (2021). "Response of a tropical cyclone to a subsurface ocean eddy and the role of boundary layer dynamics." In: *Quarterly Journal of the Royal Meteorological Society* n/a.n/a. DOI: https://doi.org/10.1002/qj.4210. eprint: https://rmets.onlinelibrary.wiley.com/doi/pdf/10.1002/qj.4210. URL: https://rmets.onlinelibrary.wiley.com/doi/abs/10.1002/qj.4210.

Lee, C.-Y. and S. S. Chen (2014). "Stable Boundary Layer and Its Impact on Tropical Cyclone Structure in a Coupled Atmosphere–Ocean Model." In: *Monthly Weather Review* 142.5, pp. 1927–1944. ISSN: 0027-0644. DOI: 10.1175/MWR-D-13-00122.1.

Leipper, D. F. and D. Volgenau (1972). "Hurricane Heat Potential of the Gulf of Mexico." In: *Journal of Physical Oceanography* 2.3, pp. 218 –224. DOI: 10.1175/1520-0485(1972)002<0218:HHPOTG>2.0.CO;2. URL: https://journals.ametsoc.org/view/journals/phoc/2/3/1520-0485_1972_002_0218_hhpotg_2_0_co_2.xml.

Li, D.-Y. and C.-Y. Huang (2018). "The influences of ocean on intensity of Typhoon Soudelor (2015) as revealed by coupled modeling." In: *Atmospheric Science Letters* 20.1, e871. DOI: 10.1002/asl.871. URL: https://doi.org/10.1002%2Fasl.871.

Li, D.-Y. and C.-Y. Huang (2019). "The influences of ocean on intensity of Typhoon Soudelor (2015) as revealed by coupled modeling." In: *Atmospheric Science Letters* 20.1, e871. ISSN: 1530261X. DOI: 10.1002/asl.871.

Li, J., H. Zhang, S. Liu, X. Wang, and L. Sun (Sept. 2021). "The Response and Feedback of Ocean Mesoscale Eddies to Four Sequential Typhoons in 2014 Based on Multiple Satellite Observations and Argo Floats." In: *Remote Sensing* 13 (19), p. 3805. ISSN: 2072-4292. DOI: 10.3390/rs13193805. URL: https://www.mdpi.com/2072-4292/13/19/3805.

Lin, I.-I., C.-H. Chen, I.-F. Pun, W. T. Liu, and C.-C. Wu (Feb. 2009). "Warm ocean anomaly, air sea fluxes, and the rapid intensification of tropical cyclone Nargis (2008)." In: *Geophysical Research Letters* 36 (3), n/a–n/a. ISSN: 00948276. DOI: 10.1029/2008GL035815. URL: http://doi.wiley.com/10.1029/2008GL035815.

Lin, I. I., G. J. Goni, J. A. Knaff, C. Forbes, and M. M. Ali (Apr. 2013). "Ocean heat content for tropical cyclone intensity forecasting and its impact on storm surge." In: *Natural Hazards* 66 (3), pp. 1481–1500. ISSN: 0921030X. DOI: 10.1007/s11069-012-0214-5. URL: https://link.springer.com/article/10.1007/s11069-012-0214-5.

Lin, I.-I., C.-C. Wu, K. A. Emanuel, I.-H. Lee, C.-R. Wu, and I.-F. Pun (2005). "The Interaction of Supertyphoon Maemi (2003) with a Warm Ocean Eddy." In: *Monthly Weather Review* 133.9, pp. 2635–2649. ISSN: 1520-0493. DOI: 10.1175/MWR3005.1.

Lin, I.-I., C.-C. Wu, I.-F. Pun, and D.-S. Ko (2008). "Upper-Ocean Thermal Structure and the Western North Pacific Category 5 Typhoons. Part I: Ocean Features and the Category 5 Typhoons' Intensification." In: *Monthly Weather Review* 136.9, pp. 3288–3306. ISSN: 1520-0493. DOI: 10.1175/2008MWR2277.1.

Linden, P. F. (1975). “The deepening of a mixed layer in a stratified fluid.” In: *Journal of Fluid Mechanics* 71.2, 385–405. DOI: 10.1017/S0022112075002637.

Lloyd, I. D. and G. A. Vecchi (Feb. 2011). “Observational evidence for oceanic controls on hurricane intensity.” In: *Journal of Climate* 24 (4), pp. 1138–1153. ISSN: 08948755. DOI: 10.1175/2010JCLI3763.1. URL: https://journals.ametsoc.org/view/journals/clim/24/4/2010jcli3763.1.xml.

Ma, Z. (2020). “A Study of the Interaction between Typhoon Francisco (2013) and a Cold-Core Eddy. Part I: Rapid Weakening.” In: *Journal of the Atmospheric Sciences* 77.1, pp. 355–377. DOI: 10.1175/JAS-D-18-0378.1. URL: https://journals.ametsoc.org/view/journals/atsc/77/1/jas-d-18-0378.1.xml.

Ma, Z., J. Fei, L. Liu, X. Huang, and X. Cheng (2013). “Effects of the Cold Core Eddy on Tropical Cyclone Intensity and Structure under Idealized Air–Sea Interaction Conditions.” In: *Monthly Weather Review* 141.4, pp. 1285–1303. ISSN: 0027-0644. DOI: 10.1175/MWR-D-12-00123.1.

Ma, Z., J. Fei, L. Liu, X. Huang, and Y. Li (2017). “An Investigation of the Influences of Mesoscale Ocean Eddies on Tropical Cyclone Intensities.” In: *Monthly Weather Review* 145.4, pp. 1181 –1201. DOI: 10.1175/MWR-D-16-0253.1. URL: https://journals.ametsoc.org/view/journals/mwre/145/4/mwr-d-16-0253.1.xml.

Masson-Delmotte, V. et al. (2021). *IPCC, 2021: Summary for Policymakers*.

Matsuoka, D., F. Araki, Y. Inoue, and H. Sasaki (2016). “A New Approach to Ocean Eddy Detection, Tracking, and Event Visualization –Application to the Northwest Pacific Ocean.” In: *Procedia Computer Science* 80. International Conference on Computational Science 2016, ICCS 2016, 6-8 June 2016, San Diego, California, USA, pp. 1601–1611. ISSN: 1877-0509. DOI: https://doi.org/10.1016/j.procs.2016.05.491. URL: https://www.sciencedirect.com/science/article/pii/S1877050916309784.

Mauritsen, T., G. Svensson, S. S. Zilitinkevich, I. Esau, L. Enger, and B. Grisogono (2007). “A Total Turbulent Energy Closure Model for Neutrally and Stably Stratified Atmospheric Boundary Layers.” In: *Journal of the Atmospheric Sciences* 64.11, pp. 4113–4126. ISSN: 1520-0469. DOI: 10.1175/2007JAS2294.1.

Menkes, C. E., M. Lengaigne, P. Marchesiello, N. C. Jourdain, E. M. Vincent, J. Lefèvre, F. Chauvin, and J. F. Royer (Jan. 2012). “Comparison of tropical cyclogenesis indices on seasonal to interannual timescales.” In: *Climate Dynamics* 38 (1-2), pp. 301–321. ISSN: 09307575. DOI: 10.1007/s00382-011-1126-x. URL: http://nomad1.ncep.noaa.gov/dods/reanalyses/.

Mogensen, K. S., L. Magnusson, and J.-R. Bidlot (2017). “Tropical cyclone sensitivity to ocean coupling in the ECMWF coupled model.” In: *Journal of Geophysical Research: Oceans* 122.5, pp. 4392–4412. ISSN: 21699275. DOI: 10.1002/2017JC012753.

Molinari, J., J. Frank, and D. Vollaro (2013). “Convective Bursts, Downdraft Cooling, and Boundary Layer Recovery in a Sheared Tropical Storm.” In: *Monthly Weather Review* 141.3, pp. 1048 –1060. DOI: 10.1175/MWR-D-12-00135.1. URL: https://journals.ametsoc.org/view/journals/mwre/141/3/mwr-d-12-00135.1.xml.

Montgomery, M. T. and R. K. Smith (2014). “Paradigms for tropical cyclone intensification.” In: *Australian Meteorological and Oceanographic Journal* 64.1, pp. 37–66. ISSN: 1836716X. DOI: 10.22499/2.6401.005.

Montgomery, M. T. and R. K. Smith (2017). "Recent Developments in the Fluid Dynamics of Tropical Cyclones." In: *Annual Review of Fluid Mechanics* 49.1, pp. 541–574. ISSN: 0066-4189. DOI: 10.1146/annurev-fluid-010816-060022.

Murakami, H. et al. (May 2012). "Future changes in tropical cyclone activity projected by the new high-resolution MRI-AGCM." In: *Journal of Climate* 25 (9), pp. 3237–3260. ISSN: 08948755. DOI: 10.1175/JCLI-D-11-00415.1. URL: https://journals.ametsoc.org/view/journals/clim/25/9/jcli-d-11-00415.1.xml.

Na, W., J. L. Mcbride, X. H. Zhang, and Y. H. Duan (Feb. 2018). "Understanding biases in tropical cyclone intensity forecast error." In: *Weather and Forecasting* 33 (1), pp. 129–138. ISSN: 15200434. DOI: 10.1175/WAF-D-17-0106.1. URL: www.ametsoc.org/PUBSReuseLicenses.

Nguyen, C. M., R. K. Smith, H. Zhu, and W. Ulrich (2002). "A minimal axisymmetric hurricane model." In: *Quarterly Journal of the Royal Meteorological Society* 128.586, pp. 2641–2661. ISSN: 1477870X. DOI: 10.1256/qj.01.156.

O'Brien, J. J. and R. O. Reid (Mar. 1967). "The Non-Linear Response of a Two-Layer, Baroclinic Ocean to a Stationary, Axially-Symmetric Hurricane: Part I. Upwelling Induced by Momentum Transfer." In: *Journal of the Atmospheric Sciences* 24 (2), pp. 197–207. ISSN: 0022-4928. DOI: 10.1175/1520-0469(1967)024<0197:tnlroa>2.0.co;2. URL: https://journals.ametsoc.org/view/journals/atsc/24/2/1520-0469_1967_024_0197_tnlroa_2_0_co_2.xml.

Ogata, T., R. Mizuta, Y. Adachi, H. Murakami, and T. Ose (July 2016). "Atmosphere-Ocean Coupling Effect on Intense Tropical Cyclone Distribution and its Future Change with 60 km-AOGCM." In: *Scientific Reports* 6 (1), pp. 1–8. ISSN: 20452322. DOI: 10.1038/srep29800. URL: http://cola.gmu.edu/grads/.

Olson, D. B. (May 1991). "Rings in the Ocean." In: *Annual Review of Earth and Planetary Sciences* 19 (1), pp. 283–311. ISSN: 0084-6597. DOI: 10.1146/annurev.ea.19.050191.001435. URL: https://www.annualreviews.org/doi/abs/10.1146/annurev.ea.19.050191.001435.

Ooyama, K. V. (1982). "Conceptual Evolution of the Theory and Modeling of the Tropical Cyclone." In: *Journal of the Meteorological Society of Japan. Ser. II* 60.1, pp. 369–380. DOI: 10.2151/jmsj1965.60.1_369.

Ooyama, K. (1969). "Numerical Simulation of the Life Cycle of Tropical Cyclones." In: *Journal of the Atmospheric Sciences* 26.1, pp. 3–40. ISSN: 0022-4928. DOI: 10.1175/1520-0469(1969)026<0003:NSOTLC>2.0.CO;2.

Patnaik, K. V., K. Maneesha, Y. Sadhuram, K. V. Prasad, T. V. R. Murty, and V. B. Rao (2014). "East India Coastal Current induced eddies and their interaction with tropical storms over Bay of Bengal." In: *Journal of Operational Oceanography* 7 (1), pp. 58–68. ISSN: 17558778. DOI: 10.1080/1755876X.2014.11020153. URL: https://www.tandfonline.com/action/journalInformation?journalCode=tjoo20.

Paul, B. K., H. Rashid, M. S. Islam, and L. M. Hunt (2010). "Cyclone evacuation in bangladesh: Tropical cyclones gorky (1991) vs. sidr (2007)." In: *Environmental Hazards* 9 (1), pp. 89–101. ISSN: 18780059. DOI: 10.3763/ehaz.2010.SI04.

Persing, J., M. T. Montgomery, J. C. McWilliams, and R. K. Smith (2013). "Asymmetric and axisymmetric dynamics of tropical cyclones." In: *Atmospheric Chemistry and Physics* 13.24, pp. 12299–12341. ISSN: 1680-7324. DOI: 10.5194/acp-13-12299-2013.

Pistrika, A. K. and S. N. Jonkman (Nov. 2010). "Damage to residential buildings due to flooding of New Orleans after hurricane Katrina." In: *Natural Hazards* 54 (2), pp. 413–434. ISSN: 0921030X. DOI: `10.1007/s11069-009-9476-y`. URL: `https://link.springer.com/article/10.1007/s11069-009-9476-y`.

Pithan, F., W. Angevine, and T. Mauritsen (2015). "Improving a global model from the boundary layer: Total turbulent energy and the neutral limit Prandtl number." In: *Journal of Advances in Modeling Earth Systems* 7.2, pp. 791–805. ISSN: 19422466. DOI: `10.1002/2014MS000382`.

Price, J. F. (1981). "Upper Ocean Response to a Hurricane." In: *Journal of Physical Oceanography* 11.2, pp. 153–175. ISSN: 0022-3670. DOI: `10.1175/1520-0485(1981)011<0153:UORTAH>2.0.CO;2`.

Pun, I.-F., I.-I. Lin, C.-C. Lien, and C.-C. Wu (2018). "Influence of the Size of Supertyphoon Megi (2010) on SST Cooling." In: *Monthly Weather Review* 146.3, pp. 661 –677. DOI: `10.1175/MWR-D-17-0044.1`. URL: `https://journals.ametsoc.org/view/journals/mwre/146/3/mwr-d-17-0044.1.xml`.

Rai, D. and S. Pattnaik (Aug. 2018). "Sensitivity of Tropical Cyclone Intensity and Structure to Planetary Boundary Layer Parameterization." In: *Asia-Pacific Journal of Atmospheric Sciences* 54 (3), pp. 473–488. ISSN: 19767951. DOI: `10.1007/s13143-018-0053-8`. URL: `https://doi.org/10.1007/s13143-018-0053-8`.

Raju, P. V., J. Potty, and U. C. Mohanty (Sept. 2011). "Sensitivity of physical parameterizations on prediction of tropical cyclone Nargis over the Bay of Bengal using WRF model." In: *Meteorology and Atmospheric Physics* 113 (3), pp. 125–137. ISSN: 01777971. DOI: `10.1007/s00703-011-0151-y`. URL: `https://link.springer.com/article/10.1007/s00703-011-0151-y`.

Riemer, M., M. T. Montgomery, and M. E. Nicholls (2010). "A new paradigm for intensity modification of tropical cyclones: thermodynamic impact of vertical wind shear on the inflow layer." In: *Atmospheric Chemistry and Physics* 10.7, pp. 3163–3188. DOI: `10.5194/acp-10-3163-2010`. URL: `https://acp.copernicus.org/articles/10/3163/2010/`.

Rogers, D. and V. Tsirkunov (2010). *Global Assessment Report on Disaster Risk Reduction*. World Bank.

Rotunno, R., Y. Chen, W. Wang, C. Davis, J. Dudhia, and G. J. Holland (2009). "Large-Eddy Simulation of an Idealized Tropical Cyclone." In: *Bulletin of the American Meteorological Society* 90.12, pp. 1783–1788. ISSN: 00030007, 15200477. URL: `http://www.jstor.org/stable/26225163`.

Sadhuram, Y., K. Maneesha, and T. V. Murty (Sept. 2012). "Intensification of Aila (May 2009) due to a warm core eddy in the north Bay of Bengal." In: *Natural Hazards* 63 (3), pp. 1515–1525. ISSN: 0921030X. DOI: `10.1007/s11069-011-9837-1`. URL: `www.imd.gov.in`.

Satoh, M. et al. (Nov. 2012). "The Intra-Seasonal Oscillation and its control of tropical cyclones simulated by high-resolution global atmospheric models." In: *Climate Dynamics* 39 (9-10), pp. 2185–2206. ISSN: 09307575. DOI: `10.1007/s00382-011-1235-6`. URL: `https://link.springer.com/article/10.1007/s00382-011-1235-6`.

Schade, L. R. and K. A. Emanuel (1999). "The Ocean's Effect on the Intensity of Tropical Cyclones: Results from a Simple Coupled Atmosphere–Ocean Model." In: *Journal of* *the Atmospheric Sciences* 56.4, pp. 642–651. ISSN: 0022-4928. DOI: 10.1175/1520-0469(1999)056<0642:TOSEOT>2.0.CO;2.

Scharroo, R., W. H. F. Smith, and J. L. Lillibridge (Oct. 2005). “Satellite altimetry and the intensification of Hurricane Katrina.” In: *Eos, Transactions American Geophysical Union* 86 (40), p. 366. ISSN: 0096-3941. DOI: 10.1029/2005eo400004. URL: https://onlinelibrary.wiley.com/doi/full/10.1029/2005EO400004https://onlinelibrary.wiley.com/doi/abs/10.1029/2005EO400004https://agupubs.onlinelibrary.wiley.com/doi/10.1029/2005EO400004.

Schmidt, C. W. and R. K. Smith (2016). “Tropical cyclone evolution in a minimal axisymmetric model revisited.” In: *Quarterly Journal of the Royal Meteorological Society* 142.696, pp. 1505–1516. ISSN: 00359009. DOI: 10.1002/qj.2753.

Seekins, D. M. (Sept. 2009). “State, society and natural disaster: Cyclone Nargis in Myanmar (Burma).” In: *Asian Journal of Social Science* 37 (5), pp. 717–737. ISSN: 15684849. DOI: 10.1163/156848409X12474536440500. URL: https://brill.com/view/journals/ajss/37/5/article-p717_3.xml.

Shay, L. K. (Jan. 2019). *Upper ocean structure: Responses to strong atmospheric forcing events*. DOI: 10.1016/B978-0-12-409548-9.11567-2.

Shay, L. K., G. J. Goni, and P. G. Black (2000). “Effects of a Warm Oceanic Feature on Hurricane Opal.” In: *Monthly Weather Review* 128.5, pp. 1366–1383. DOI: 10.1175/1520-0493(2000)128<1366:eoawof>2.0.co;2. URL: https://doi.org/10.1175%2F1520-0493%282000%29128%3C1366%3Aeoawof%3E2.0.co%3B2.

Smith, R. K. (1968). “The surface boundary layer of a hurricane.” In: *Tellus* 20.3, pp. 473–484. DOI: https://doi.org/10.1111/j.2153-3490.1968.tb00388.x. eprint: https://onlinelibrary.wiley.com/doi/pdf/10.1111/j.2153-3490.1968.tb00388.x. URL: https://onlinelibrary.wiley.com/doi/abs/10.1111/j.2153-3490.1968.tb00388.x.

Smith, R. K. (2003). “A simple model of the hurricane boundary layer.” In: *Quarterly Journal of the Royal Meteorological Society* 129.589, pp. 1007–1027. ISSN: 00359009. DOI: 10.1256/qj.01.197.

Smith, R. K. and M. T. Montgomery (2016). “The efficiency of diabatic heating and tropical cyclone intensification.” In: *Quarterly Journal of the Royal Meteorological Society* 142.698, pp. 2081–2086. ISSN: 00359009. DOI: 10.1002/qj.2804.

Smith, R. K. and M. T. Montgomery (2015). “Toward clarity on understanding tropical cyclone intensification.” In: *Journal of the Atmospheric Sciences* 72.8, pp. 3020–3031. ISSN: 15200469. DOI: 10.1175/JAS-D-15-0017.1. URL: https://journals.ametsoc.org/view/journals/atsc/72/8/jas-d-15-0017.1.xml.

Smith, R. K., M. T. Montgomery, and V.-S. Nguyen (2009). “Tropical cyclone spin-up revisited.” In: *Quarterly Journal of the Royal Meteorological Society* 135.642, pp. 1321–1335. ISSN: 00359009. DOI: 10.1002/qj.428.

Smith, R. K., M. T. Montgomery, and G. L. Thomsen (Apr. 2014). “Sensitivity of tropical-cyclone models to the surface drag coefficient in different boundary-layer schemes.” In: *Quarterly Journal of the Royal Meteorological Society* 140 (680), pp. 792–804. ISSN: 00359009. DOI: 10.1002/qj.2057. URL: https://onlinelibrary.wiley.com/doi/10.1002/qj.2057.

Smith, R. K. and G. L. Thomsen (2010a). “Dependence of tropical-cyclone intensification on the boundary-layer representation in a numerical model.” In: *Quarterly Journal of* *the Royal Meteorological Society* 136.652, pp. 1671–1685. DOI: 10.1002/qj.687. URL: https://doi.org/10.1002%2Fqj.687.

Smith, R. K. and G. L. Thomsen (Oct. 2010b). "Dependence of tropical-cyclone intensification on the boundary-layer representation in a numerical model." In: *Quarterly Journal of the Royal Meteorological Society* 136 (652), pp. 1671–1685. ISSN: 00359009. DOI: 10.1002/qj.687. URL: https://onlinelibrary.wiley.com/doi/10.1002/qj.687.

Smith, R. K. and S. Wang (2018). "Axisymmetric balance dynamics of tropical cyclone intensification: Diabatic heating versus surface friction." In: *Quarterly Journal of the Royal Meteorological Society* 144.716, pp. 2350–2357. ISSN: 00359009. DOI: 10.1002/qj.3389.

Smith, S. D. (Dec. 1988). "Coefficients for sea surface wind stress, heat flux, and wind profiles as a function of wind speed and temperature." In: *Journal of Geophysical Research* 93 (C12), p. 15467. ISSN: 0148-0227. DOI: 10.1029/JC093iC12p15467. URL: http://doi.wiley.com/10.1029/JC093iC12p15467.

Srinivas, C. V., R. Venkatesan, D. V. B. Rao, and D. H. Prasad (June 2008). *Numerical Simulation of Andhra Severe Cyclone (2003): Model Sensitivity to the Boundary Layer and Convection Parameterization*. DOI: 10.1007/978-3-7643-8493-7_3. URL: https://link.springer.com/chapter/10.1007/978-3-7643-8493-7_3.

Stensrud, D. (2007). *Parameterization Schemes: Keys to Understanding Numerical Weather Prediction Models*. Cambridge University Press. ISBN: 9780521865401. URL: https://books.google.de/books?id=lMXSpRwKNO8C.

Sugi, M., H. Murakami, and K. Yoshida (Sept. 2016). "Projection of future changes in the frequency of intense tropical cyclones." In: *Climate Dynamics 2016 49:1* 49 (1), pp. 619–632. ISSN: 1432-0894. DOI: 10.1007/S00382-016-3361-7. URL: https://link.springer.com/article/10.1007/s00382-016-3361-7.

Sun, L., Y.-J. Yang, T. Xian, Y. Wang, and Y.-F. Fu (Dec. 2012). "Ocean Responses to Typhoon Namtheun Explored with Argo Floats and Multiplatform Satellites." In: *Atmosphere-Ocean* 50 (sup1), pp. 15–26. ISSN: 0705-5900. DOI: 10.1080/07055900.2012.742420. URL: https://www.tandfonline.com/doi/full/10.1080/07055900.2012.742420.

Tao, W., J. Shi, S. Chen, S. Lang, P. Lin, S.-Y. Hong, C. Peters-Lidard, and A. Hou (2011). "The impact of microphysical schemes on hurricane intensity and track." In: *Asia-Pacific Journal of Atmospheric Sciences* 47, pp. 1–16.

Titley, H., M. Yamaguchi, and L. Magnusson (Sept. 2019). "Current and potential use of ensemble forecasts in operational TC forecasting: results from a global forecaster survey." In: *Tropical Cyclone Research and Review* 8 (3), pp. 166–180. ISSN: 22256032. DOI: 10.1016/j.tcrr.2019.10.005.

Trabing, B. C. and M. M. Bell (Dec. 2020). "Understanding error distributions of hurricane intensity forecasts during rapid intensity changes." In: *Weather and Forecasting* 35 (6), pp. 2219–2234. ISSN: 15200434. DOI: 10.1175/WAF-D-19-0253.1. URL: http://www.nhc.noaa.gov/verification/verify7.shtml.

Vogl, S. and R. K. Smith (2009). "Limitations of a linear model for the hurricane boundary layer." In: *Quarterly Journal of the Royal Meteorological Society* 135.641, pp. 839–850. ISSN: 00359009. DOI: 10.1002/qj.390.

Wadler, J. B., J. A. Zhang, B. Jaimes, and L. K. Shay (2018). "Downdrafts and the Evolution of Boundary Layer Thermodynamics in Hurricane Earl (2010) before and during Rapid

Intensification." In: *Monthly Weather Review* 146.11, pp. 3545 –3565. DOI: 10.1175/MWR-D-18-0090.1. URL: https://journals.ametsoc.org/view/journals/mwre/146/11/mwr-d-18-0090.1.xml.

Walsh, K. J., M. Fiorino, C. W. Landsea, and K. L. McInnes (May 2007). "Objectively determined resolution-dependent threshold criteria for the detection of tropical cyclones in climate models and reanalyses." In: *Journal of Climate* 20 (10), pp. 2307–2314. ISSN: 08948755. DOI: 10.1175/JCLI4074.1. URL: https://journals.ametsoc.org/view/journals/clim/20/10/jcli4074.1.xml.

Wang, Y. (2002). "An Explicit Simulation of Tropical Cyclones with a Triply Nested Movable Mesh Primitive Equation Model: TCM3. Part II: Model Refinements and Sensitivity to Cloud Microphysics Parameterization*." In: *Monthly Weather Review* 130.12, pp. 3022–3036. ISSN: 0027-0644. DOI: 10.1175/1520-0493(2002)130<3022:AESOTC>2.0.CO;2.

Wehner, M. F., K. A. Reed, B. Loring, D. Stone, and H. Krishnan (Feb. 2018). "Changes in tropical cyclones under stabilized 1.5 and 2.0°C global warming scenarios as simulated by the Community Atmospheric Model under the HAPPI protocols." In: *Earth System Dynamics* 9 (1), pp. 187–195. ISSN: 21904987. DOI: 10.5194/esd-9-187-2018.

Williams, S., M. Petersen, P. T. Bremer, M. Hecht, V. Pascucci, J. Ahrens, M. Hlawitschka, and B. Hamann (2011). "Adaptive extraction and quantification of geophysical vortices." In: *IEEE Transactions on Visualization and Computer Graphics* 17 (12), pp. 2088–2095. ISSN: 10772626. DOI: 10.1109/TVCG.2011.162.

Wong, M. L. and J. C. Chan (2004). "Tropical cyclone intensity in vertical wind shear." In: *Journal of the atmospheric sciences* 61.15, pp. 1859–1876.

Wu, C.-C., C.-Y. Lee, and I.-I. Lin (2007a). "The Effect of the Ocean Eddy on Tropical Cyclone Intensity." In: *Journal of the Atmospheric Sciences* 64.10, pp. 3562–3578. DOI: 10.1175/JAS4051.1. eprint: https://doi.org/10.1175/JAS4051.1. URL: https://doi.org/10.1175/JAS4051.1.

Wu, C.-C., C.-Y. Lee, and I.-I. Lin (2007b). "The Effect of the Ocean Eddy on Tropical Cyclone Intensity." In: *Journal of the Atmospheric Sciences* 64.10, pp. 3562–3578. ISSN: 1520-0469. DOI: 10.1175/JAS4051.1.

Yablonsky, R. M. and I. Ginis (Mar. 2012). "Impact of a Warm Ocean Eddy's Circulation on Hurricane-Induced Sea Surface Cooling with Implications for Hurricane Intensity." In: *Monthly Weather Review* 141 (3). Effect of WCE circulation on TC intensity (makes intensification less favourable), pp. 997–1021. ISSN: 0027-0644. DOI: 10.1175/MWR-D-12-00248.1.

Yamada, Y., M. Satoh, M. Sugi, C. Kodama, A. T. Noda, M. Nakano, and T. Nasuno (Dec. 2017). "Response of tropical cyclone activity and structure to global warming in a high-resolution global nonhydrostatic model." In: *Journal of Climate* 30 (23), pp. 9703–9724. ISSN: 08948755. DOI: 10.1175/JCLI-D-17-0068.1. URL: http://creativecommons..

Yan, Y., L. Li, and C. Wang (2017). "The effects of oceanic barrier layer on the upper ocean response to tropical cyclones." In: *Journal of Geophysical Research: Oceans* 122.6, pp. 4829–4844. ISSN: 21699275. DOI: 10.1002/2017JC012694. URL: http://doi.wiley.com/10.1002/2017JC012694.

Yang, L., M. Liu, J. A. Smith, and F. Tian (Feb. 2017). “Typhoon nina and the august 1975 flood over central china.” In: *Journal of Hydrometeorology* 18 (2), pp. 451–472. ISSN: 15257541. DOI: 10.1175/JHM-D-16-0152.1. URL: http://weather.uwyo..

Yi, J., Y. Du, Z. He, and C. Zhou (Feb. 2014). “Enhancing the accuracy of automatic eddy detection and the capability of recognizing the multi-core structures from maps of sea level anomaly.” In: *Ocean Science* 10 (1), pp. 39–48. ISSN: 1812-0792. DOI: 10.5194/os-10-39-2014.

Zängl, G., D. Reinert, P. Rípodas, and M. Baldauf (2015). “The ICON (ICOsahedral Non-hydrostatic) modelling framework of DWD and MPI-M: Description of the non-hydrostatic dynamical core.” In: *Quarterly Journal of the Royal Meteorological Society* 141.687, pp. 563–579. ISSN: 00359009. DOI: 10.1002/qj.2378.

Zhang, D.-L., Y. Liu, and M. K. Yau (2001). “A Multiscale Numerical Study of Hurricane Andrew (1992). Part IV: Unbalanced Flows.” In: *Monthly Weather Review* 129.1, pp. 92–107. ISSN: 0027-0644. DOI: 10.1175/1520-0493(2001)129<0092:AMNSOH>2.0.CO;2.

Zhang, J. A., J. J. Cione, E. A. Kalina, E. W. Uhlhorn, T. Hock, and J. A. Smith (2017a). “Observations of Infrared Sea Surface Temperature and Air–Sea Interaction in Hurricane Edouard (2014) Using GPS Dropsondes.” In: *Journal of Atmospheric and Oceanic Technology* 34.6, pp. 1333 –1349. DOI: 10.1175/JTECH-D-16-0211.1. URL: https://journals.ametsoc.org/view/journals/atot/34/6/jtech-d-16-0211.1.xml.

Zhang, J. A. and F. D. Marks (2015a). “Effects of Horizontal Diffusion on Tropical Cyclone Intensity Change and Structure in Idealized Three-Dimensional Numerical Simulations.” In: *Monthly Weather Review* 143.10, pp. 3981–3995. ISSN: 0027-0644. DOI: 10.1175/MWR-D-14-00341.1.

Zhang, J. A., F. D. Marks, M. T. Montgomery, and S. Lorsolo (2010). “An Estimation of Turbulent Characteristics in the Low-Level Region of Intense Hurricanes Allen (1980) and Hugo (1989).” In: *Monthly Weather Review* 139.5, pp. 1447 –1462. DOI: 10.1175/2010MWR3435.1. URL: https://journals.ametsoc.org/view/journals/mwre/139/5/2010mwr3435.1.xml.

Zhang, J. A., D. S. Nolan, R. F. Rogers, and V. Tallapragada (Aug. 2015b). “Evaluating the impact of improvements in the boundary layer parameterization on hurricane intensity and structure forecasts in HWRF.” In: *Monthly Weather Review* 143 (8), pp. 3136–3155. ISSN: 15200493. DOI: 10.1175/MWR-D-14-00339.1. URL: https://journals.ametsoc.org/view/journals/mwre/143/8/mwr-d-14-00339.1.xml.

Zhang, J. A., R. F. Rogers, D. S. Nolan, and F. D. Marks (2011). “On the Characteristic Height Scales of the Hurricane Boundary Layer.” In: *Monthly Weather Review* 139.8, pp. 2523–2535. ISSN: 0027-0644. DOI: 10.1175/MWR-D-10-05017.1.

Zhang, J. A., R. F. Rogers, and V. Tallapragada (Apr. 2017b). “Impact of parameterized boundary layer structure on tropical cyclone rapid intensification forecasts in HWRF.” In: *Monthly Weather Review* 145 (4), pp. 1413–1426. ISSN: 15200493. DOI: 10.1175/MWR-D-16-0129.1. URL: www.ametsoc.org/PUBSReuseLicenses.

Zhang, Q., L. Wu, and Q. Liu (Apr. 2009). “Tropical cyclone damages in China 1983-2006.” In: *Bulletin of the American Meteorological Society* 90 (4), pp. 489–495. ISSN: 00030007. DOI: 10.1175/2008BAMS2631.1. URL: www.econstats.com.

Zhu, T. and D.-L. Zhang (2006). "Numerical Simulation of Hurricane Bonnie (1998). Part II: Sensitivity to Varying Cloud Microphysical Processes." In: *Journal of the Atmospheric Sciences* 63.1, pp. 109–126. ISSN: 1520-0469. DOI: `10.1175/JAS3599.1`.

Zschau, J. and A. Küppers (2003). *Early Warning Systems for Tropical Storms*. DOI: `10.1007/978-3-642-55903-7`.

Zängl, G., D. Reinert, P. Rípodas, and M. Baldauf (Apr. 2014). "The ICON (ICOsahedral Non-hydrostatic) modelling framework of DWD and MPI-M: Description of the non-hydrostatic dynamical core." In: *Q.J.R. Meteorol. Soc.* 141.687, pp. 563–579. ISSN: 0035-9009. DOI: `10.1002/qj.2378`. URL: `https://doi.org/10.1002/qj.2378`.

DECLARATION

Versicherung an Eides statt

Declaration of oath

Hiermit erkläre ich an Eides statt, dass ich die vorliegende Dissertationsschrift selbst verfasst und keine anderen als die angegebenen Quellen und Hilfsmittel benutzt habe.

I hereby declare upon oath that I have written the present dissertation independently and have not used further resources and aids than those stated.

Hamburg, 12th April 2022

Arjun Kumar

Arjun Unnithan Kumar

Hinweis / Reference

Die gesamten Veröffentlichungen in der Publikationsreihe des MPI-M
„Berichte zur Erdsystemforschung / Reports on Earth System Science“,
ISSN 1614-1199

sind über die Internetseiten des Max-Planck-Instituts für Meteorologie erhältlich:
http://www.mpimet.mpg.de/wissenschaft/publikationen.html

All the publications in the series of the MPI -M
„Berichte zur Erdsystemforschung / Reports on Earth System Science“,
ISSN 1614-1199

are available on the website of the Max Planck Institute for Meteorology:
http://www.mpimet.mpg.de/wissenschaft/publikationen.html